Gyrokinetic Electron and Fully Kinetic Ion Particle Simulation on Current Sheet Instabilities

by

Zhenyu Wang

A dissertation submitted to the Graduate Faculty of
Auburn University
in partial fulfillment of the
requirements for the Degree of
Doctor of Philosophy

Auburn, Alabama
August 6, 2016

Keywords: particle simulation, current sheet, instability

Approved by

Yu Lin, Chair, Alumni Professor of Physics
Joseph Perez, Professor of Physics
Guofu Niu, Professor of Electrical and Computer Engineering
David Maurer, Associate Professor of Physics
Kaijun Liu, Assistant Professor of Physics

Abstract

Linear eigenmode stability properties of three-dimensional instabilities in a Harris current sheet with a finite guide magnetic field are systematically studied employing the gyrokinetic electron and fully kinetic ion (GeFi) particle-in-cell (PIC) particle simulation model with a realistic ion-to-electron mass ratio m_i/m_e, where m_i and m_e are the ion and electron masses, respectively. In contrast to the fully kinetic PIC simulation scheme, the fast electron cyclotron motion and plasma oscillations are systematically removed in the GeFi model, and hence one can employ the realistic mass ratio m_i/m_e.

In order to valid the GeFi code for the small guide field limit, the GeFi simulations are benchmarked against both the fully kinetic PIC simulation and the analytical eigenmode theory, and an excellent agreement is obtained. In order to thoroughly understand the properties of both electrostatic (ES) and electromagnetic (EM) instabilities in the Harris sheet, the GeFi simulation is carried out both using a simplified code in the ES limit and using the fully EM code. Lower-hybrid drift instability (LHDI), drift-kink instability (DKI), drift-sausage instability (DSI), and Buneman instability (BI) are found to be present in the current sheet, among which the LHDI is predominantly an ES instability.

Under a small guide field B_G, the LHDI is found to be excited, with $k\sqrt{\rho_i\rho_e} \sim 1$, where $\mathbf{k}$ is the wave vector perpendicular to the nonuniformity direction. For small wave numbers k_y along the current direction, the most unstable eigenmodes of LHDI are peaked at the location where $\mathbf{k} \cdot \mathbf{B} = 0$, consistent with previous analytical and simulation studies. Here, $\mathbf{B}$ is the equilibrium magnetic field. As k_y increases, however, the most unstable eigenmodes of LHDI are found to be peaked at $\mathbf{k} \cdot \mathbf{B} \neq 0$. In addition, the simulation results indicate that varying m_i/m_e, the current sheet width, and the guide magnetic field can affect the stability

of LHDI. Simulations with the varying mass ratio confirm the lower hybrid frequency and wave number scalings.

Under a moderate B_G, the DKI and DSI are excited, in the long wavelength regime ($k\rho_i \sim 1$). The magnetic fluctuations of DKI are localized at the edge of current sheet, whereas the DSI has compressional perturbations localized around the center. In the k_x-k_y space, the DKI and DSI occupy the smaller and larger k regime, respectively. The most unstable DKI are away from $\mathbf{k} \cdot \mathbf{B} = 0$, while the DSI is peaked at $\mathbf{k} \cdot \mathbf{B} = 0$.

At a larger guide field $B_G \sim B_{x0}$, an electromagnetic instability with a compressional magnetic perturbation is found to be present exactly at the center of current sheet. The growth rate of this mode is found to peak at $\mathbf{k} \times \mathbf{B} = 0$. The growth rate of this mode is consistent with that of the Buneman instability. Since the magnetic perturbations in this unstable mode are at the current sheet center and dominated by a compressional fluctuation δB_y in the direction of the electron drift velocity, the mode may contribute directly to the electron anomalous resistivity in magnetic reconnection.

Acknowledgments

I am most obliged to my advisor Dr. Yu Lin. She led me into the field of plasma simulation. Over the past six years, she taught me much knowledge of plasma physics. She also put a lot of efforts on training my oral and writing communication skills. Without her guidance and encouragement, my thesis research can never be finished.

I would like to thank Dr. Liu Chen for sharing his physics insights and encouraging me to carry out this study. I am indebted to Dr. Xueyi Wang for teaching me a lot in numerical algorithms. Also I appreciate the collaboration from Dr. Kurt Tummel. I would like to thank Dr. Kaijun Liu for his helpful suggestions in the past year. I appreciate Dr. Joseph Perez, Dr. Guofu Niu, and Dr. David Maurer for reviewing my thesis. In my graduate studies, I received supports and encouragements from faculty, staff and my classmates of the Physics Department at Auburn University. I want to give them my thanks.

Finally, I want to thank my parents for their endless loves and supports.

Table of Contents

List of Figures

List of Tables

Chapter 1

Introduction

Magnetic reconnection[1] is a fundamental and important phenomenon in both natural and laboratory plasmas[2, 3]. The reconnection process, which involves the breaking and reconnecting of different magnetic field lines. In the reconnection process, magnetic energy stored in the current sheet is rapidly released and transferred into kinetic energy of plasmas. The reconnection process can occur in the solar atmosphere, and has been observed in solar flares[4, 5] and/or coronal mass ejections[6, 7]. It has also been frequently observed in the Earths magnetosphere, such as the flux transfer events[8, 9, 10] in the magnetopause and in the magnetospheric substorm[11, 12], in which magnetic energy is released and transferred rapidly. Magnetic reconnection has also been observed in laboratory experiment, for example, the magnetic reconnection experiment (MRX) [13, 14].

Analytical and numerical studies have been performed for decades to understand the physics of magnetic reconnection in a current sheet[3]. A current sheet contains inhomogeneous plasmas with antiparallel magnetic field components and a cross-field drift current. In general, also contains a guide magnetic field component along the direction of the cross-field current. It is believed that the reconnection process can occur when the 'frozen-in' field condition is broken due to finite resistivity in plasmas. In collisional plasmas, the resistivity is originated from the particle-particle collision on the micro-scales. The resistive magneto-hydro dynamic (MHD) theory has successfully explained the excitation of reconnection in collisional plasmas[3].

In collisionless plasmas, the observed reconnection rate is usually fast. The mechanisms of the onset of collisonless reconnection, however, are still a mystery. There has been no consistent explanation for the fast rate of collisionless reconnection. It is believed that

certain physical mechanisms of interaction between plasma waves and particles can exist to slow down electrons and thus play the role of the 'resistivity' to trigger magnetic reconnection. This 'resistivity', usually called the 'anomalous resistivity', can also provide a mechanism for fast collisionless reconnection [16, 17, 18, 19, 20, 21, 22, 23]. However, until now, the source of anomalous resistivity is still poorly understood. It is believed that the electric and magnetic fluctuations of instabilities of current sheet can slow down the speed of the electrons and/or ions in the cross-field current direction. The decelerating effect causes anomalous resistivity in the current sheet[24, 25]. Therefore, it is important to study the instabilities existing in a current sheet.

In this chapter, the resistive MHD reconnection models are introduced first. The collisionless reconnection models are discussed next. Previous studies of current sheet instabilities are also reviewed.

1.1 Resistive MHD Reconnection Model

Early reconnection models were developed on the base of magnetohydrodynamic (MHD) framework. The first analytic model of reconnection was given by Sweet[26] and Parker[27]. In the Sweet-Parker model, reconnection was approximated with a two dimensional (2-D) incompressible problem of boundary layer. The rate of reconnection was derived. However, the reconnection rate given by this model was several orders of magnitude smaller than the observation results. Petschek[28] modified this model by including a larger outflow region outside the small diffusion layer. The Petschek model led to an enhanced rate of reconnection. In this section, the above two reconnection models are introduced briefly.

1.1.1 Sweet-Parker Reconnection Model

Fig 1.1 shows the Sweet-Parker model[26, 27], which is a 2-D steady-state incompressible MHD model. The blue curves with arrows are magnetic field lines. The red dashed lines mark the diffusion layer, whose width and length are δ and Δ, respectively. The magnetic

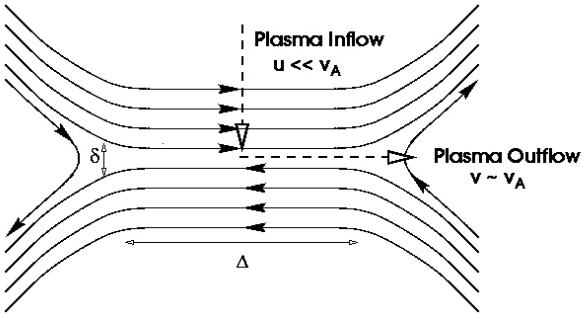

Figure 1.1: Sweet-Parker reconnection model (PPPL)

field lines are frozen together with the plasma flow toward the diffusion layer from top and bottom. In the layer, the energy of magnetic field is transferred to the kinetic and thermal energy of plasmas by the Joule dissipation. Meanwhile, plasmas flow out along the horizontal direction. Based on the Bernoulli equation, the outflow speed of plasma is approximately equal to the Alfven speed v_A. Because of the mass continuity, the inflow mass $v_R\Delta$ should be equal to the outflow mass $v_A\delta$, where v_R is the inflow speed of plasma. The inflow speed can thus be written as

$$v_R = (\delta/\Delta)v_A. \tag{1.1}$$

According to Ohm's law,

$$E_R = \eta J, \tag{1.2}$$

where E_R is the inductive electric field of reconnection diffusion layer, η is the resistivity of the diffusion layer, and J is the current density in the diffusion layer. The current J can be calculated from Ampere's law as,

$$J = B/\mu_0\delta. \tag{1.3}$$

Based on eqs. (1), (2), and (3), the outflow speed can be given as

$$v_R = v_A/\sqrt{S}, \tag{1.4}$$

where $S = \mu_0 v_A \Delta/\eta$ is the dimensionless Lundquist number. The time scale of reconnection is $t_R = L/v_R = \sqrt{S}(\Delta/v_A)$. The Lundquist number is usually sufficiently large for collisionless space plasmas. For example, the Lundquist number is larger than 10^{12} in the solar corona, and the diffusion time scale $\Delta/v_A \approx 10$s in the solar flare. The Sweet-Parker model predicted that the period of the flare is around 0.1 year. However, the observations showed that the time scale of flares is around several tens of minutes. Therefore, the reconnection rate given by the Sweet-Parker model is way too small to explain the observations. Overall, it cannot explain the fast energy transfer in solar flare and pulsations in space plasmas.

1.1.2 Petschek Reconnection Model

In order to explain the fast reconnection rate, Petschek[28] modified the theoretical reconnection model by introducing the effects of slow shock waves in the outflow region. In this model, due to the existence of slow shocks, the diffusion layer occupies only a very small region of reconnection. The reconnection rate given by the Petschek model was significantly enhanced. The slow shock introduces plasma flows into the small diffusion layer. Thus, the majority of magnetic energy is dissipated by the slow shock, unlike theSweet-Parker model, in which the Joule dissipation is dominant. A sketch of the Petschek model is shown in Fig. 1.2. In the figure, the slow shocks exist in the region enveloped by the dashed lines, and the diffusion layer with effective length L^* is marked by the rectangular solid lines. The effective length of the diffusion layer L^* is much shorter than the length in the Sweet-Parker model. Therefore, the reconnection rate given by the Petschek model is much larger than that of the Sweet-Parker model. The reconnection rate of the Petschek model is given by[29]

$$v_R/v_A = \pi/8\ln S. \tag{1.5}$$

In the near-Earth space, the value of $\ln S$ is usually around 10 20. A reconnection rate consistent with the observation can thus be obtained by the Petschek model. However, numerical

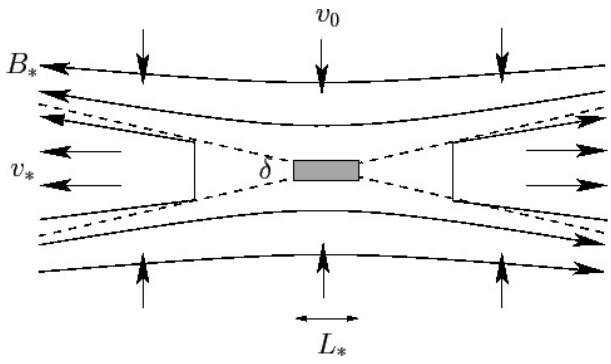

Figure 1.2: Petschek reconnection model (Fitzpatrick)

simulations show that the slow shocks can only be excited if L^* and L are comparable[30, 31]. The two basic assumptions of the Petschek model, the short diffusion layer and the slow shock cannot coexist.

1.2 Collisionless Reconnection Models

In collisionless plasmas, there exist little classical resistivity. To understand the fast reconnection in space plasmas, collisionless reconnection models are developed in the recent decades. In this section, two collisionless models, the Hall MHD model and the multiple island collisionless reconnection model, are discussed.

1.2.1 Hall MHD Model

In the two-fluid treatment, the collisional MHD reconnection model obeys the classical Ohm's law,

$$\mathbf{E} + \mathbf{V} \times \mathbf{B} = \eta \mathbf{J} \tag{1.6}$$

Since, the classical resistivity does not exist in collisionless plasmas, the generalized Ohm's law was introduced to treat the collisionless reconnection. From the two-fluid theory, the generalized Ohm's law can be written as

$$\mathbf{E} + \mathbf{V} \times \mathbf{B} = \frac{\mathbf{1}}{\mathbf{en}} \mathbf{J} \times \mathbf{B} - \frac{\mathbf{1}}{\mathbf{en}} \nabla \cdot \mathbf{P_e} - \frac{\mathbf{m_e}}{\mathbf{e}} \frac{\mathbf{dV_e}}{\mathbf{dt}}. \tag{1.7}$$

Here, the classical resistivity term is removed, and the first, second and third terms on the righthand side describe the Hall effect, the gradient of electron pressure, and the electron inertia, respectively. The Hall electric field is due to the electron and ion charge separation associated with the particle inertias. In this collisionless reconnection model, the Hall effect plays a key role. Due to the mass separation between electrons and ions, the diffusion layer in the collisionless plasma has dual structures. One is the electron diffusion region, and the other is the ion diffusion region. The grey area in Fig. 1.3 shows the ion diffusion region, in which the ions are decoupled with the magnetic field, while the electrons are still frozen in the field lines. The separation of the ion and electron motions also produces the Hall current, which corresponds to a quadrupolar magnetic field component perpendicular to the reconnection plane. The spatial scale of the ion diffusion region is comparable to the ion inertial length $d_i = c/\omega_{pi}$. In the center of the ion diffusion region (white area), the strength of magnetic field is weak in the cases with a zero guide field, and the electrons are also unmagnetized. The region is the so-called electron diffusion region with a typical spatial scale length of $d_e = c/\omega_{pe}$, and the electron pressure gradient term is dominant in the region.

It is believed that the whistler physics associated with the Hall effect leads to a fast reconnection rate in the collisionless plasma[100]. The simulation results from resistive MHD, Hall MHD, Hybrid and fully kinetic particle simulations showed that the fast reconnection is observed when the Hall effect is included in the simulation model[2].

The Hall effect was observed by satellite observations and laboratory experiments. For example, Polar satellites found the existence of the Hall quadrupole field in the magnetopause[32]. The Geotail satellite found the Hall currents around the X-line of reconnection in the magnetotail[33]. The Cluster satellites further confirmed the existence of Hall quadrupole field in the reconnection diffusion region[34]. In Fig. 1.5, the B_y component is perpendicular to the reconnection plane. The red circles indicate $B_y > 0$, and the black circles indicate $B_y < 0$, where the size of circles correspond to the strength of the field. The figure shows a

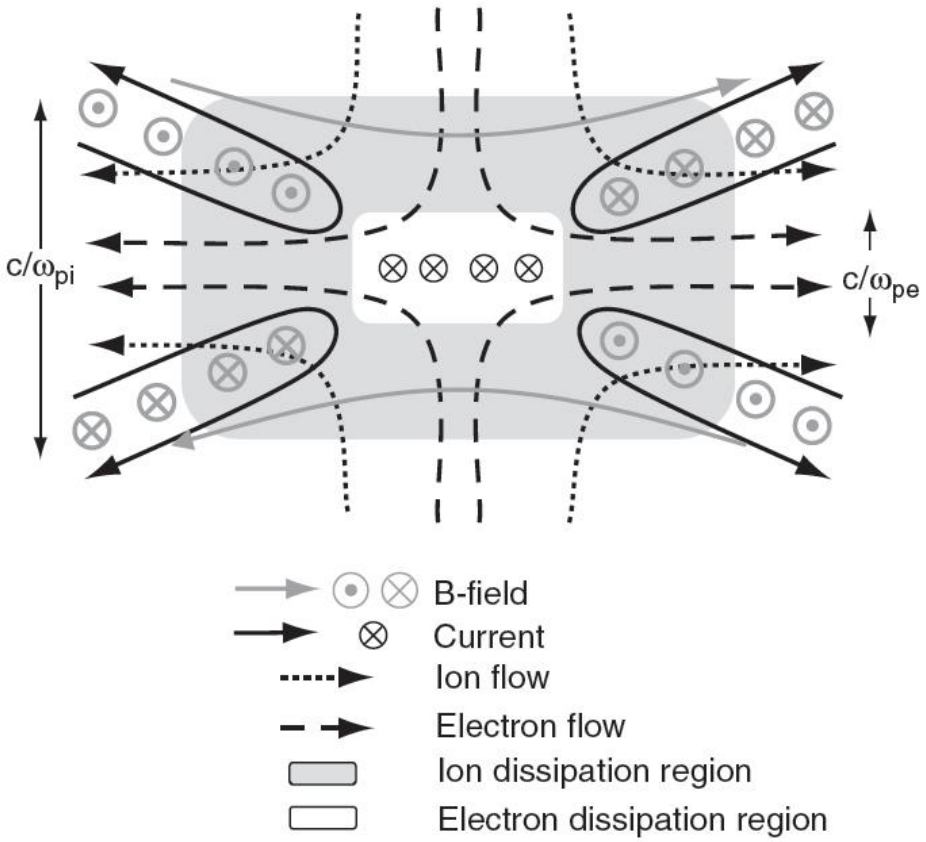

Figure 1.3: The structure of electron diffusion region in collisionless reconnection[15]

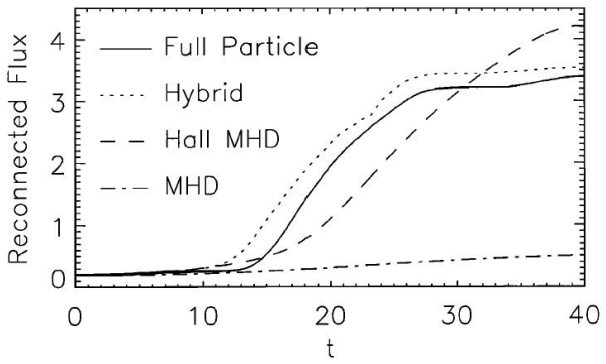

Figure 1.4: Reconnection rate versus time in different simulation models[2].

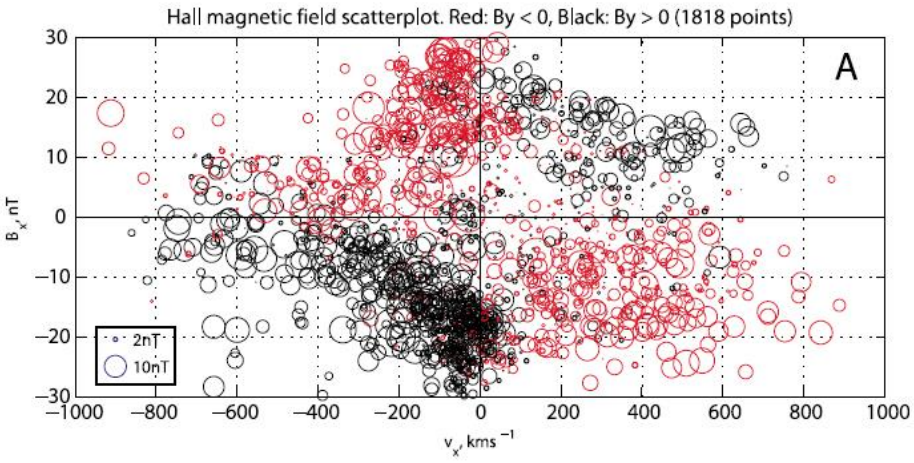

Figure 1.5: The magnetic field B_y perpendicular to the reconnection plane on the B_x-V_x coordinates, where B_x and V_x are the magnetic field and the flow velocity respectively in the direction of the anti-parallel magnetic field[34].

typical quadrupolar B_y structure as a function of the anti-parallel magnetic field and reconnection flow. The MRX experiment also observed the Hall effect in reconnection[35, 36]. As Fig. 1.6 showing, the experiment found the decoupling of electrons and ions and the existence of the Hall quadrupole field. It also showed that the drift speed of ions is much smaller than that of electrons, and thus the major carrier of the Hall currents are the electrons.

1.2.2 Multiple Island Collisionless Reconnection

In recent decades, fully kinetic particle-in-cell (PIC) simulation method was utilized to study collisionless reconnection, and numerous new results were obtained. Simulations based on periodical boundary conditions under a zero guide field showed that the scale of the electron diffusion layer is comparable to the electron inertial scale[37, 38, 39, 40]. However, periodic boundary conditions are invalid to plasmas in reality. Open boundaries were then used in the particle simulation of reconnection[41]. The simulation results showed that in early stage the reconnection with the open boundaries are nearly consistent with that of periodic boundaries. However, in later stage, the electron diffusion region was elongated (Fig. 1.6), and thus the reconnection rate was reduced. The elongated current sheet then

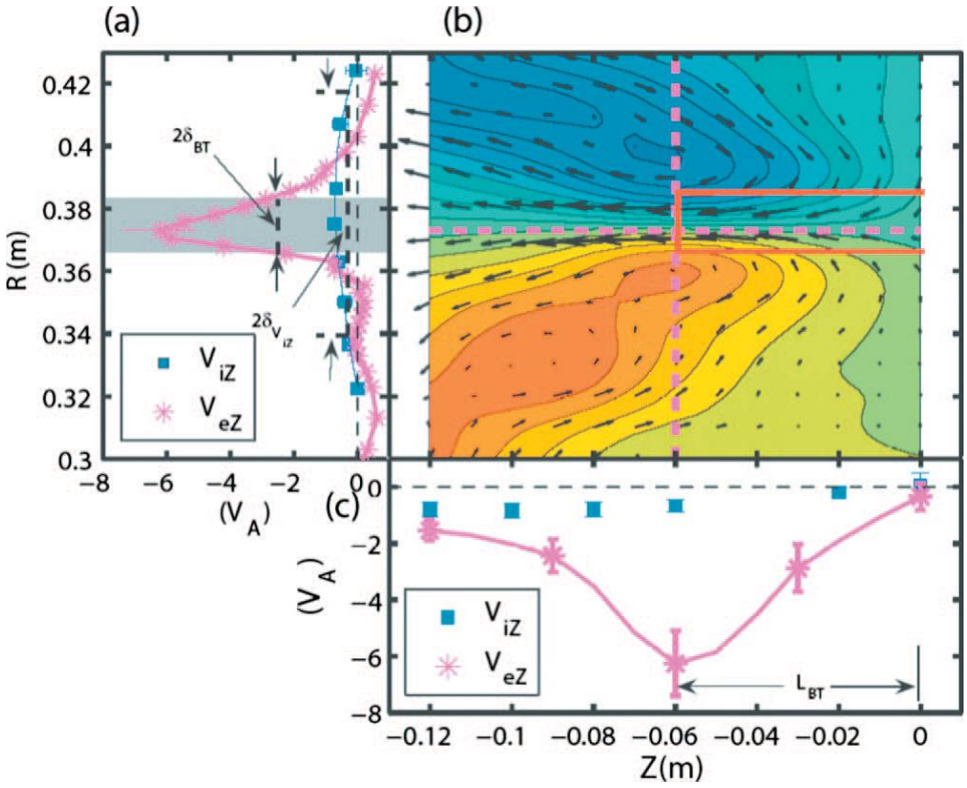

Figure 1.6: The results of MRX: (a) the profile of out-flow velocity of electrons and ions in the radial direction, (b) the contours of the magnetic field perpendicular to the reconnection plane and the vectors of velocity of electron flow, (c) the out-flow velocities of electrons and ions in the horizontal direction[35].

broke up due to the instabilities that produce secondary islands. The reconnection rate was enhanced by the split and shorter current sheets. The secondary islands continuously expanded and emerged with the primary island[41]. The secondary islands were also found by Cluster spacecraft in the reconnection diffusion region[42, 43, 44].

1.3 Current Sheet Instabilities

The Hall physics, however, does not provide dissipation in the electron diffusion region because $\mathbf{E}_{Hall} \cdot \mathbf{J}$=0, where $\mathbf{E}_{Hall} = \mathbf{J} \times \mathbf{B}$ is the Hall electric field. On the other hand, various instabilities can be excited in current sheet by inhomogeneous density and magnetic field and/or the drift current. Since wave-particle interaction in the current sheet may provide anomalous resistivity and trigger collisionless reconnection[24, 25], it is important to study the instabilities in a current sheet. Analytical theory and numerical simulations were used for decades to study the current sheet instabilities. Particle simulations found that the electrons are slowed down in the diffusion region at the onset stage of reconnection[25], suggesting some mechanism may play the role of resistivity in the collisionless plasma. One possible mechanism is that the instabilities of the current sheet scatter the electrons by the wave-particle resonance. Anomalous resistivity in current sheet was also suggested to be a candidate to achieve fast reconnection on a rapid time scale. In the following, we review investigations of the current sheet instabilities.

1.3.1 Tearing Mode

In early years, collisionless tearing mode instability was studied as the onset mechanism of reconnection[48, 49, 50, 51]. The growth rate of the instability was compared to the time scale of the magnetosheath flow from the nose of the magnetopause to the polar cusp [52]. It was shown that only very thin current sheet can satisfy the requirement that the growth time of tearing mode should be much less than the critical flow time at the magnetopause. In a thin current sheet, the kinetic effects are important because the wavelength of the tearing mode

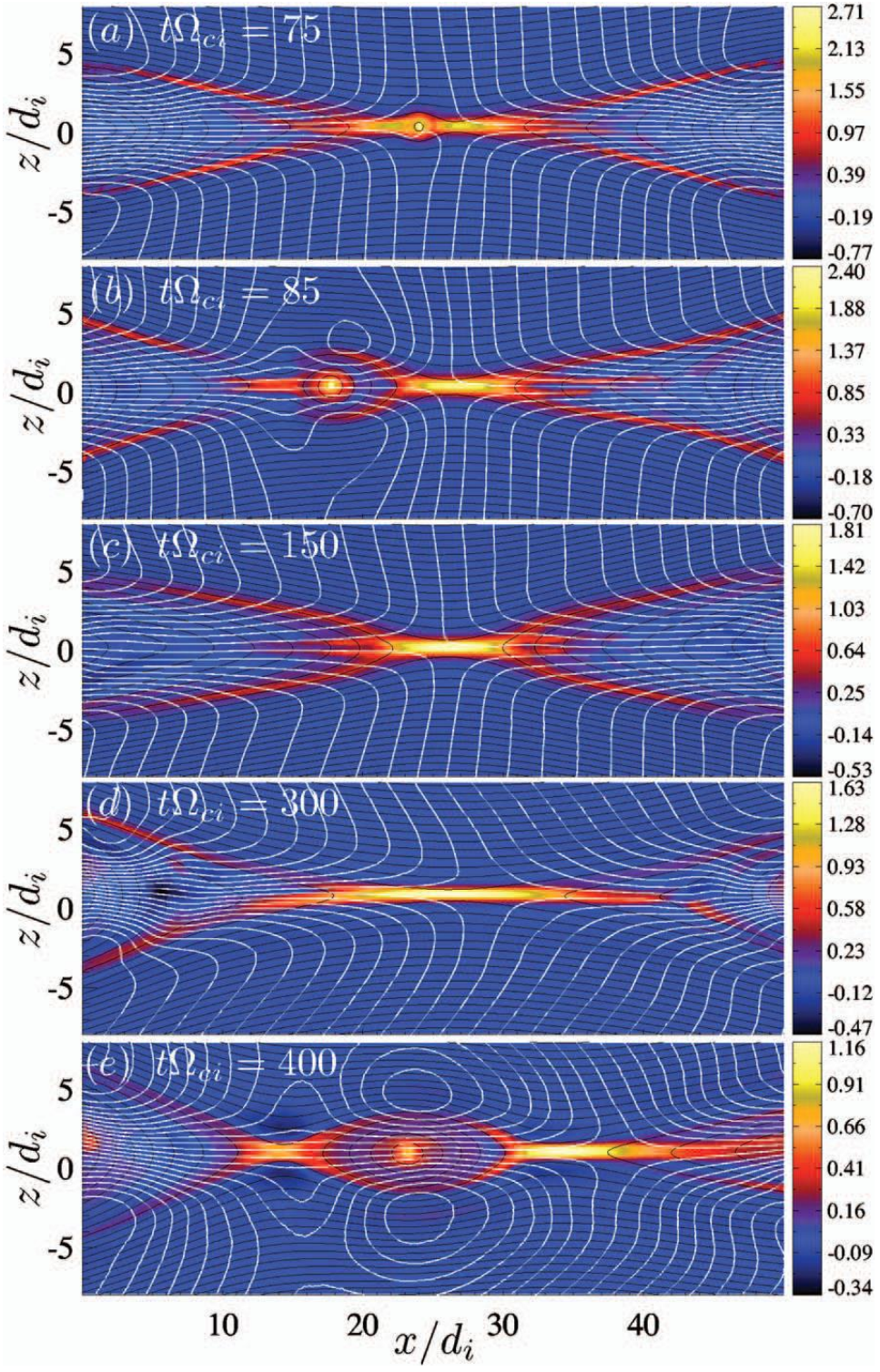

Figure 1.7: The evolution in the electron diffusion region of the simulation with open boundaries. White lines are the streamlines of ions, Black lines show magnetic field lines and the color contours show the electron velocity perpendicular to the reconnection plane.[41]

are comparable to the ion gyroradii. Fully kinetic and gyrokinetic analytical theories were developed, and it was found that the real frequency of the tearing mode is nearly zero [53, 54], indicating that the instability is standing at the resonance point and does not interact with the electrons. Thus the tearing mode in the 2-D reconnection plane cannot directly resonate with electrons to provide the anomalous resistivity. In the gyrokinetic studies, the guide field was found to stabilize the 2-D tearing mode. Fully kinetic particle simulations also confirmed the results. The 3-D numerical solution of the linear Vlasov theory[55] was used to examine the collisionless tearing mode as a function of the guide field. In the weak and strong guide field regimes, the most unstable tearing mode was found to have a zero frequency and be perpendicular to the cross-field current. Similar to the 2-D situation, the 3-D tearing mode with a strong or weak guide field is not likely to be a source of the anomalous resistivity. In the intermediate guide field regime, the results showed that the tearing mode in the 3-D space has a finite real frequency in the drift frequency range and can obliquely propagate with respect to the anti-parallel field. Although the propagation is not completely in the reconnection plane, the tearing mode is still nearly perpendicular to the cross-field current. The 3-D tearing modes still cannot directly resonate with the electrons. Besides, theories and simulations showed that the growth rate of the tearing mode is less than Ω_i, which is the ion gyrofrequecy, too small to provide the enough resistivity for magnetic reconnection.

1.3.2 Lower Hybrid Drift Instability

Several instabilities can be excited in the plane which contains the current sheet normal and the cross-field current, in the so-called 'out-of-plane' direction. Although these instabilities cannot directly break and reconnect the field lines of the anti-parallel field, the instabilities in the out-of-plane direction usually propagate along the direction of the current and thus may resonate with the drifting electrons. Among these instabilities, the lower-hybrid drift instability (LHDI) has attracted long time attention as a possible source of anomalous

resistivity. The lower-hybrid drift instability is a short wavelength quasi-electrostatic mode driven by the finite β and ∇B.

An electromagnetic local linear theory [56, 57] found that the higher beta will stabilize the LHDI. Nonlocal electrostatic theory was developed and applied to study the drift wave instabilities in a density gradient plasma[58] and/or sheared magnetic field[59]. The nonlocal kinetic theory for a Harris current sheet without guide field found that the LHDI is well localized at the edge of the current sheet[60]. A guide field will significantly influence the instabilities in a current sheet. Yoon [61] derived a local kinetic theory that can treat an arbitrary diamagnetic drift speed and guide field. It is found that the most unstable LHDI is a oblique mode when guide field exists. A gyrokinetic nonlocal theory was derived[62] under gyrokinetic electrons and fully kinetic unmagnetized ions assumption. The analytical calculation showed the 3-D LHDI is not constricted by $\mathbf{k} \cdot \mathbf{b} = 0$, where $\mathbf{k}$ is the wave vector of the LHDI and $\mathbf{b}$ is unit vector of the local magnetic field.

Meanwhile, numerical simulations were carried out to study the LHDI for decades of years. Daughton[63, 64] used a linear Vlasov simulation to investigate the linear LHDI and drift kink instability in a Harris current sheet. The simulation predicted the fastest growing LHDI satisfies $\mathbf{k} \cdot \mathbf{b} = 0$ in presence of finite guide field. The subsequent fully kinetic PIC simulations[65, 66, 67] showed that the LHDI, which is initially excited at the edge of the current sheet, can penetrate into the central region of the current sheet, then heat electron anisotropically and produce current bifurcation. Recently, the 3-D PIC simulations of magnetic reconnection showed the reconnection onset and rate significantly depends on current sheet instabilities in the full 3-D space. Yin[68] carried out a PIC simulation for 3-D pair plasmas and found that the interaction of tearing and kink modes cause reconnection onset that is patchy and occurs at multiple sites. Daughton[69] found that flux ropes in reconnection are dramatically different between 2-D and 3-D cases due to tearing-type instabilities in the full 3-D spectrum. Based on these simulations, the current sheet instabilities in 3-D

space should be further investigated. Meanwhile, previous particle simulations on reconnection and/or current sheet instabilities were focus mainly on artificial ion-to-electron mass ratios. But theoretical studies suggested that the behaviors of the current sheet instabilities dramatically change as the mass ratio varies[70, 63]. The characteristics of the instabilities are still not fully understood.

Moreover, previous studies presumed that the most unstable mode satisfies $k_{\|} = 0$ where $k_{\|} = \mathbf{k} \cdot \mathbf{B}$. A PIC simulation was carried out in the rotated 2-D plane that satisfies $k_{\|} \neq 0$, which found that the frequency and growth rate agree well with the theoretical caculations[64]. However, as mentioned above, a recent gyrokinetic theory[62] found that the most unstable LHDI can occur at $k_{\|} \neq 0$ for certain ks. The unstable modes with $k_{\|} \neq 0$ can be the potential source of the anomalous resistivity because the electrons can resonate with the modes and be scattered. Therefore, further particle simulations are needed to confirm whether the $k_{\|} \neq 0$ mode exists. A comprehensive 3-D particle simulation is required to examine the LHDIs in the full 3-D space.

1.4 Drift Kink Instability

A long wavelength ($k\rho_i \sim 1$) electromagnetic mode driven by the drift current was found by simulations and theories[71, 72, 73, 75, 74]. This unstable mode has a wave vector along the direction of the current, and was called the drift kink instability (DKI)[76]. A two-fuild theory of the DKI was developed, and the results were compared with the particle simulations[73]. Based on the two-fluid theory, structures of both even and odd symmetry were found[77]. However, the wavelength of these unstable modes is comparable to the current sheet half-width L. The kinetic effects are thus not negligible, and the two-fluid theory is somehow invalid.

A kinetic theory was also developed and applied to the DKI, and it was found that the linear growth rate agrees well with that from the particle simulation[74]. However, the linear theory showed an even mode structure, while an odd mode structure was obtained in the

simulation. The real frequency and the wavelength of the unstable mode are also significantly different from those from the simulation. A numerical calculation of the linear Vlasov theory[70] was used to examined the DKI, in the smaller ion-to-electron mass ratio m_i/m_e regime, and the numerical results agreed well with the PIC simulation results. However, at larger m_i/m_e the linear growth rate obtained from the numerical calculation was an order of magnitude smaller than that from the particle simulation. Until now, the understanding of the DKI is still far from sufficient.

Besides the discrepancies between the theories and simulations mentioned above, previous PIC simulations were based on the nonlinear models, which made it hard to identify the polarities of the DKI in the linear stage and compare with the linear theories. In addition, previous analytical and numerical studies were performed with a zero guide field. The influence of guide field on the mode structure and frequency of the DKI is not understood.

1.5 Our Particle Simulation Approach for Current Sheet

As mentioned above, particle simulations were used to investigate the physics of fast reconnection. Particle simulation has proven to be a powerful tool in studying the evolution of various plasma kinetic processes, in which the plasma usually involves nonlinear dynamics under the realistic conditions.

However, there has always been a dilemma between the available computing resources and the requirement in the resolution of relevant kinetic processes.

Collisionless reconnection and related current sheet instabilities are a good example. Reconnection involves a wide range of spatial and temporal scales. Its spatial scales are from electron Larmor radius to global Alfven scales, and its temporal scales are from the MHD time-frames to the lower-hybrid frequencies. In the particle simulations of reconnection, one need to resolve these broad ranges of spatial and temporal scales. It is rather difficult to include all the disparate temporal and spatial scales of both electrons and ions in the calculation of a realistic system due to the constraints of available computing power. In the

following, we take the fully kinetic (FK) particle simulation model as an example to explain the necessity of developing a new particle simulation model.

Fully kinetic particle simulation has been used to investigate the onset of reconnection for several decades[80, 81, 78, 79]. In the FK particle codes, both the electrons and the ions are treated as the FK particles. Due to the disparate temporal and spatial scales between the electrons and the ions, the most of FK simulations have employed the unrealistically reduced ion-to-electron mass ratio m_i/m_e to accommodate the limited computing resources. However, theoretical studies show that the current sheet instabilities are dramatically affected by the mass ratio[70, 63]. Meanwhile, most of the previous FK simulations were carried out in a 2-D plane due to the available computing power. Nevertheless, recent 3-D PIC simulations of magnetic reconnection, which still used a reduced m_i/m_e, showed that the reconnection onset and rate are significantly different from those in a 2-D simulation[68, 69]. Thus in order to understand magnetic reconnection and the associated current sheet instabilities, 3-D particle simulations under a realistic mass ratio, in a large system size, are need. However, the fully kinetic particle models demand a tremendous computing resource for this kind of simulations.

To enhance the computation effectiveness, reduced kinetic models such as drift kinetic (DK) and gyrokinetic models were attempted for magnetic reconnection with a finite guide field[116, 122, 117, 120, 118, 119], in which the high frequency cyclotron motions are averaged out and the simulation time steps are greatly increased. The computation time could thus be significantly saved. Gyrokinetic (GK) models[86] are widely used in the tokamak physics for three decades[124]. In recent years, GK models were also applied to the magnetospheric research[125, 127, 118]. For the specific problem of magnetic reconnection, the GK approach is valid for the general cases with a finite guide field, which are important but not adequately understood so far.

Nevertheless, to properly address wave modes in the lower-hybrid and kinetic Alfvén regimes when frequencies are higher or comparable to ion cyclotron frequencies, ions must

be treated as fully kinetic particles. For this purpose, a novel gyro-kinetic electron and fully kinetic ion (GeFi) particle simulation model was developed in the past decade[83, 82]. In the GeFi model, the electrons obey the governance of the GK equation[86, 87, 88, 89] in five-dimension phase space and the ions follow the FK equation in six-dimension space. The rapid electron gyromotion has been averaged out, while finite Larmor radius effect and off-diagonal components of the electron pressure tensor are retained[86, 90]. Therefore, a larger time step is allowed in the simulation and thus the GeFi model can effectively handle the realistic m_i/m_e. In a broader sense, the application of the GeFi model is not limited to magnetic reconnection. The model is particularly suitable for the problems that satisfy the gyrokinetic ordering[86]. Different from the conventional GK models[126, 123, 125], wave modes relevant to magnetic reconnection, such as LHDIs, KAWs, and MHD modes (with characteristic frequency $\omega \ll \Omega_e$, where Ω_e is the electron gyrofrequency) are now all included on an equal footing. In addition to the numerical advantage that realistic m_i/m_e can be handled with the GeFi scheme, the GeFi simulation can also be used as a reduced theoretical framework, together with the corresponding analytical theory.

As a unique and novel simulation model, the GeFi model has been benchmarked against the analytical theory for uniform plasmas[83, 82], and has also been used to study the Landau damping of lower hybrid waves in the uniform plasma[129]. For inhomogeneous plasmas, the GeFi model has been used to investigate the 2-D tearing and current-driven instabilities in a Harris current sheet[130, 84, 54]. Nevertheless, it is also necessary and important to validate the GeFi results by direct comparison with FK particle simulations, which to date has only been done for tearing mode under a strong guide field[82, 54], but not yet for the high frequency LHDI in a current sheet and under a small guide field, B_G, that is much smaller than the anti-parallel component, B_{x0}. Since the GK approximation assumes a gyro phase uniformity, benchmarking the GeFi model against the FK simulations for a small $B_G \ll B_{x0}$ is particularly necessary.

In this dissertation work, the GeFi particle code is benchmarked against the FK particle code and used to investigate the electrostatic and electromagnetic instabilities of the current sheet in the lower hybrid frequency range.

1.6 Summary and Outline: Central Task of the Thesis

In this chapter, the basic physical picture of the magnetic reconnection is introduced. The resistive MHD reconnection models on the reconnection are discussed, and the Hall MHD model for fast collisionless reconnection is presented. Recent development of multiple X-line model associated with the island interaction is also described. On the other hand, anomalous resistivity due to wave-particle interaction is also important for triggering the fast collisionless reconnection. The mechanism of the current sheet instabilities as the potential source of the anomalous resistivity is discussed. Previous theoretical and simulation studies of the tearing mode, lower hybrid drift instability, and drift kink instability are reviewed. A novel gyrokinetic particle simulation model, the GeFi particle model is introduced, which can be used to simulate a large system under a realistic proton-to-electron mass ratio.

The central task of this thesis is to systematically investigate the 3-D current-driven instabilities (e.g., LHDI and DKI) in a Harris current sheet, which are fundamentally important to the anomalous resistivity of magnetic reconnection, using the 3-D GeFi particle code. The GeFi simulations are benchmarked against the FK particle simulations and the GK eigenmode theory. Since the LHDI has been found to be dominated by electrostatic properties, our simulation is conducted by first calculating the current sheet instabilities in the ES limit. This way, the LHDI is singled out. Then, the simulation is carried out with the full EM code, which covers the complete ES and EM properties, and the presence of various EM modes will be discussed as a function of the guide field strength.

The rest of the thesis is organized as follows. The GeFi particle model and its algebra are described in chapter II. The electrostatic simulation results are shown in chapter III.

The electromagnetic results are then shown in chapter IV. Finally, chapter V summarizes the thesis work.

Chapter 2

Simulation Model and Algebra

In this chapter, the simulation tools used in the thesis is introduced. Firstly, the formulism of the GeFi model are is presented. Then the algebra used in the GeFi code is introduced. The GK electron distribution function in the Harris equilibrium is also given. The results from the GeFi code are compared to the results from the explicit FK code. The explicit FK particle simulation scheme is also given in this chapter.

2.1 GeFi Model

2.1.1 Equations of Particle Motion

In the GeFi model, the ions are treated as FK particles and the elctrons are treated with the GK approximations. The FK ions are governed by the Vlasov equation in the six-dimensional phase space ($\mathbf{x}$,$\mathbf{v}$)

$$\frac{\partial f_i}{\partial t} + \mathbf{v} \cdot \frac{\partial f_i}{\partial \mathbf{x}} + \frac{q_i}{m_i}(\mathbf{E} + \frac{1}{c}\mathbf{v} \times \mathbf{B}) \cdot \frac{\partial f_i}{\partial \mathbf{x}} = 0. \tag{2.1}$$

Here, f_i is ion distribution function, m_i is the ion mass, q_i is the charge of ion, $\mathbf{E}$ and $\mathbf{B}$ are electric and magnetic field respectively. The GeFi particle model uses the particle-in-cell (PIC) scheme[91]. Thus, f_i can be evaluated by the statistic of a group of particles in the discrete space,

$$f_i(\mathbf{x}, \mathbf{v}, t) = \sum_j \delta(\mathbf{x} - \mathbf{x}_j)\delta(\mathbf{v} - \mathbf{v}_j), \tag{2.2}$$

where j is the index of the individual particles. The evolution of f_i is determined by the ion equation of motion,

$$\frac{d\mathbf{v}}{dt} = \frac{q_i}{m_i}(\mathbf{E} + \mathbf{v} \times \mathbf{B}), \tag{2.3}$$

$$\frac{d\mathbf{x}}{dt} = \mathbf{v}. \tag{2.4}$$

The number density and current density, n_i and $\mathbf{J}_i$, are obtained from the moments of f_i,

$$n_i = \int f_i d^3v = \sum_j \delta(\mathbf{x} - \mathbf{x}_j), \tag{2.5}$$

$$\mathbf{J}_i = q_i \int \mathbf{v} f_i d^3v = q_i \sum_j \mathbf{v}_j \delta(\mathbf{x} - \mathbf{x}_j) \tag{2.6}$$

in a discrete space.

For electrons, the difficulty in the conventional fully kinetic particle simulation is that, physically, the spatial size should be larger than Debye length, and the temporal scale needs to be small enough to cover electron plasma frequency and/or electron gyrofrequency, numerically, the grid size and time step need to satisfy the Courant condition[91]. However, the reconnection studies intend to have simulation size much larger than the ion skin depth and simulation time much longer than Alfvén time. Hence the large ion-to-electron mass ratio introduces extreme computing power consuming. Since the modes of interest are in lower-hybrid frequency range, and the finite Lamor radii effects of electrons are not negligible, the GK electron approach is used in the model. By assuming $k_\perp \gg k_\parallel$, which is generally true for most of processes in the reconnection, the high frequency electron plasma oscillation has been suppressed. This is valid for $\Omega_e^2 \sim \omega_{pe}^2$, where ω_{pe} is the electron plasma frequency.

The GK ordering is applied on the electrons,

$$\frac{\omega}{\Omega_e} \sim \frac{\rho_e}{L} \sim k_\parallel \rho_e \sim \frac{\delta B}{B} \sim \epsilon, k_\perp \rho_e \sim 1. \tag{2.7}$$

Here, $\rho_e = v_{te}/\Omega_e$ is the the electron Larmor radius, $v_{te} = \sqrt{T_e/m_e}$ is the electron thermal speed, L is the macroscopic background plasma scale length, δB is the perturbed magnetic field on the microscopic wave scale lengths, and ϵ is a smallness parameter. For electrons, the coordinate is transformed from particle coordinates $(\mathbf{x}, \mathbf{v})$ to gyrocenter coordinates ($\mathbf{R}$, $p_\parallel$, μ, ζ), where $\mathbf{R} = (\mathbf{x} - \rho)$ is the gyrocenter position with $\rho = (\mathbf{b} \times \mathbf{v}_{\perp e})/\Omega_e$ being the gyroradii vector, $\mathbf{b} = \mathbf{B}/B$, $p_\parallel = m_e v_{e\parallel} + q_e A_\parallel/c$ the parallel canonical momentum of electrons, μ is the magnetic moment and ζ is the gyrophase angle. The parallel direction is defined along the background magnetic field $\bar{\mathbf{B}}$. The Vlasov equation in guiding-center coordinates can be obtained by averaging over ζ,

$$\frac{\partial F_e}{\partial t} + \frac{d\mathbf{R}}{dt} \cdot \frac{\partial F_e}{\mathbf{R}} + \frac{dp_\parallel}{dt} \frac{\partial F_e}{\partial p_\parallel} = 0, \tag{2.8}$$

where the upper-case varibles are gyrocenter variables, and $F_e(\mathbf{R}, p_\parallel, \mu)$ is the distribution function of electrons in the five-dimensional gyrocenter phase space. The gyrocenter euations of motion are[86, 87, 88]

$$\frac{dp_\parallel}{dt} = -\mathbf{b}^* \cdot [q_e < \nabla \phi_0^* > + \mu \nabla \bar{B}_0], \tag{2.9}$$

$$\frac{d\mathbf{R}}{dt} = v_{e\parallel} \mathbf{b}^* + \frac{c}{q_e \bar{B}} \bar{\mathbf{b}} \times [q_e < \nabla \phi_0^* > + \mu \nabla \bar{B}_0], \tag{2.10}$$

where m_e and $v_{e\parallel}$ are the electron mass and electron parallel velocity, respectively, q_e is the electron charge, μ is the magnetic moment, $\bar{\mathbf{B}}_0$ is the background magnetic field, $\bar{\mathbf{b}} = \bar{\mathbf{B}}_0/\bar{B}_0$, and $\mathbf{b}^* = \bar{\mathbf{b}} + (v_{e\parallel}/\bar{\Omega}_e)\bar{\mathbf{b}} \times (\bar{\mathbf{b}} \cdot \nabla)\bar{\mathbf{b}}$. $\phi_0^* = \bar{\phi}_0 - \mathbf{v} \cdot \bar{\mathbf{A}}_0/c$ is the unperturbed scalar potential, $< \ldots >$ represents gyro-averaging, and $\perp$ and $\parallel$ denote components perpendicular and parallel to the background magnetic field, respectively. The electron gyro-averaged guiding center charge-density and $p_\parallel$-current are

$$< N_e > = \int F_e d^3 v, \tag{2.11}$$

$$< J_{e\|} >= \frac{q_e}{m_e} \int p_\| F_e d^3v. \tag{2.12}$$

In GK simulations, the gyro-averaging is carried out numerically in a discrete space, the technology will be introduced later.

2.1.2 Field Equations

The vector and scalar potentials are calculated by the Maxwell equations, which consists of the Poisson's and Ampere's law, with the Coulomb gauge $\nabla \cdot \mathbf{A} = 0$. The scalar potential are firstly calculated. The Poisson's equation in the lab frame is

$$\nabla_\perp^2 \phi = -4\pi(q_i n_i + q_e n_e). \tag{2.13}$$

Here, assuming $|\nabla_\perp^2| \gg |\nabla_\|^2|$, $\nabla^2\phi$ is replaced by $\nabla_\perp^2\phi$ in eq.(13) to suppress the undesirable high-frequency Langmuir oscillation along $\mathbf{B}$. Following the nonlinear GK formalism[86, 90], assuming $|\rho_e \nabla_\perp| < 1$, the electron density n_e can be written as

$$n_e = \frac{q_e}{m_e} \int d^3v (\frac{\partial f_e}{\partial w})[\phi - < \phi > + \frac{1}{c} < \mathbf{v}_\perp \cdot \mathbf{A} >] + < N_e >, \tag{2.14}$$

where $< N_e >$ is the guiding-center density of the electrons. Combining eq. (13) and (14), the generalized GK Poisson's equation

$$\nabla_\perp \cdot (1 + \frac{\bar{\omega}_{pe}^2}{\bar{\Omega}_e^2}) \cdot \nabla_\perp \phi + 4\pi \bar{n}_e q_e \frac{\delta B_\|}{\bar{B}} = -4\pi(q_i n_i + q_e < N_e >), \tag{2.15}$$

where $\bar{n}_e$ is the equilibrium electron density, $\delta \mathbf{B}_\| = \bar{\mathbf{b}} \cdot \delta \mathbf{B}$, the second and third terms on left-hand side (LHS) represents the polarization drift and $\mathbf{E} \times \mathbf{B}$ drift associated with inductive electric field $\partial A / \partial t$, respectively.

In the eq. (2.15), there are two unknown variables, since $\omega \ll \Omega_e$, the $\delta B_\parallel$ is calculated by using the electron force balance

$$\nabla \cdot (n_e q_e \mathbf{E}) = \nabla \cdot [\nabla \cdot \mathbf{P}_e - \frac{1}{c}\mathbf{J}_e \times \mathbf{B}], \tag{2.16}$$

where

$$\mathbf{P}_e = (\bar{n}_e q_e \rho_e^2 \nabla_\perp^2 \phi + 2\bar{n}_e T_e \frac{\delta \bar{B}_\parallel}{\bar{B}})(\mathbf{I} - \frac{1}{2}\bar{\mathbf{b}}\bar{\mathbf{b}}) + < \mathbf{P}_g >, \tag{2.17}$$

$$< \mathbf{P}_g >= \int m_e \mathbf{v}\mathbf{v} F_e d^3 v, \tag{2.18}$$

the first two terms of $\mathbf{P}_e$ are correspond to the electron perpendicular guiding-center drifts. Noting the electron current $\mathbf{J}_e = (c/4\pi)\nabla \times \mathbf{B} - \mathbf{J}_i$ with $\mathbf{J}_i$ being the ion current density, $|\nabla_\perp| \gg |\nabla_\parallel|$, the eq. (2.16) can be written as

$$\nabla^2 \Psi = -\nabla \cdot (\nabla \cdot \mathbf{P}_g + \frac{1}{c}\mathbf{J}_i \times \mathbf{B}), \tag{2.19}$$

where, noting $\bar{n}_e q_e = -\bar{n}_i q_i$,

$$\Psi = \frac{(1 + \bar{\beta}_e)\bar{B}\delta B_\parallel}{4\pi} - \bar{n}_i q_i (1 + \rho_e^2 \nabla_\perp^2)\phi. \tag{2.20}$$

Expressing $\delta B_\parallel$ in the terms of Ψ, the GK Poisson's equation, eq. (2.15) can finally be expressed as

$$[\nabla_\perp \cdot (1 + \bar{\beta}_e + \frac{\bar{\omega}_{pe}^2}{\bar{\Omega}_e^2}) \cdot \nabla_\perp - \frac{\bar{\omega}_{pi}^2}{\bar{V}_A^2}]\phi = -4\pi[(1 + \bar{\beta}_e)(q_i n_i + q_e < N_e >) - \frac{4\pi \bar{n}_i q_i}{\bar{B}^2}\Psi], \tag{2.21}$$

where $\bar{\omega}_{pi}$ and $\bar{V}_A$ are the background ion plasma frequency and the Alfvén speed, respectively. Eqs. (19) and (22) completely determine Ψ and ϕ. Given $\delta B_\parallel$, we can now calculate $\mathbf{A}$. Decompose $\mathbf{A}$ into three locally orthogonal components, i.e. $\mathbf{A} = \mathbf{A}_\perp + A_\parallel \bar{\mathbf{b}} + \nabla_\perp \xi$. $\mathbf{A}_\perp$

is determined by the perpendicular Ampere's law

$$\nabla^2 \mathbf{A}_\perp = -\frac{4\pi}{c}\mathbf{J}_\perp, \tag{2.22}$$

with $\mathbf{J}_\perp = (c/4\pi)\nabla \times \delta B_\parallel$. $A_\parallel$ can be given by parallel Ampere's law

$$(\nabla^2 - \frac{\omega_{pe}^2}{c^2})A_\parallel = -\frac{4\pi}{c}(\mathbf{J}_{i\parallel} + < \mathbf{J}_{\mathbf{e}\parallel} >). \tag{2.23}$$

$\nabla_\perp \xi$ can be determined by the Coulomb gauge $\nabla \cdot \mathbf{A} = 0$ or $\nabla_\perp^2 \xi = -\nabla \cdot (A_\parallel \bar{\mathbf{b}})$.

2.1.3 Linearized GeFi δf Scheme

Since the thesis focuses on the linear instabilities, we use the linearized GeFi δf scheme for our simulation study.

For the linearized scheme, the FK ion equations of motion in unperturbed orbits are

$$\begin{aligned} \frac{d\mathbf{p}_i}{dt} &= -q_i \nabla(\bar{\phi}_0 - \mathbf{v}_i \cdot \bar{\mathbf{A}}_0/c), \\ \frac{d\mathbf{x}_i}{dt} &= \mathbf{v}_i, \end{aligned} \tag{2.24}$$

where q_i is the ion charge, $\mathbf{p}_i$ is the ion canonical momentum, $\mathbf{x}_i$ is the ion position, $\mathbf{v}_i$ is the ion velocity, ϕ_0 and $\mathbf{A}_0$ are the equilibrium scalar and vector potentials, respectively, and the 'bar' indicates the background quantities. The perturbed ion particle weighting function $W_i = \delta f_i / \bar{f}_i$ is governed by the linearized Vlasov equation in the six-dimensional phase space $(\mathbf{x}, \mathbf{v}_i)$,

$$\frac{dW_i}{dt} = q_i \nabla \delta\phi \cdot \frac{\partial ln \bar{f}_i}{\partial \mathbf{v_i}}. \tag{2.25}$$

Here, $\bar{f}_i$ is the equilibrium ion distribution function, and $\delta\phi$ is the perturbed scalar potential.

The gyrocenter equations of motion in unperturbed orbits for the parallel electron canonical momentum, $p_\parallel = m_e v_{e\parallel} + q_e A_\parallel / c$, and for the electron gyrocenter position, $\mathbf{R}$, are given

by [86, 87, 88, 89]

$$\begin{aligned}\frac{dp_\parallel}{dt} &= -\mathbf{b}^*\cdot[q_e < \nabla\phi_0^* > +\mu\nabla\bar{B}_0], \\ \frac{d\mathbf{R}}{dt} &= v_{e\parallel}\mathbf{b}^* + \frac{c}{q_e\bar{B}}\bar{\mathbf{b}}\times[q_e < \nabla\phi_0^* > +\mu\nabla\bar{B}_0],\end{aligned} \tag{2.26}$$

where m_e and $v_{e\parallel}$ are the electron mass and electron parallel velocity, respectively, q_e is the electron charge, μ is the magnetic moment, $\bar{\mathbf{B}}_0$ is the background magnetic field, $\bar{\mathbf{b}} = \bar{\mathbf{B}}_0/\bar{B}_0$, and $\mathbf{b}^* = \bar{\mathbf{b}} + (v_{e\parallel}/\bar{\Omega}_e)\bar{\mathbf{b}}\times(\bar{\mathbf{b}}\cdot\nabla)\bar{\mathbf{b}}$. $\phi_0^* = \bar{\phi}_0 - \mathbf{v}\cdot\bar{\mathbf{A}}_0/c$ is the unperturbed scalar potential, $< \ldots >$ represents gyro-averaging, and $\perp$ and $\parallel$ denote components perpendicular and parallel to the background magnetic field, respectively. The weighting function of the GK electrons obeys

$$\begin{aligned}\frac{dW_e}{dt} = -\frac{c\bar{\mathbf{b}}}{q_e\bar{B}_0}\times(q_e < \nabla\delta\phi >)\cdot\frac{\partial ln\bar{F}_e}{\partial\mathbf{R}} \\ +\mathbf{b}^*\cdot(q_e < \nabla\delta\phi >)\cdot\frac{\partial ln\bar{F}_e}{\partial p_\parallel}.\end{aligned} \tag{2.27}$$

The linearized GK Poisson's equation in a nonuniform plasma can be expressed as

$$\begin{aligned}[\nabla_\perp(1+\bar{\beta}_e+\frac{\bar{\omega}_{pe}^2}{\bar{\Omega}_e^2})\cdot\nabla_\perp - \frac{\bar{\omega}_{pi}^2}{\bar{V}_A^2}]\delta\phi \\ = -4\pi[(1+\bar{\beta}_e)(q_i\delta n_i + q_e < \delta N_e >) - \frac{4\pi\bar{n}_i q_i}{\bar{B}^2}\delta\Psi],\end{aligned} \tag{2.28}$$

where $\bar{\omega}_{pe}$ and $\bar{\Omega}_e$ are the electron plasma frequency and electron gyrofrequency based on the equilibrium magnetic field and plasma density, δn_i is the perturbed ion number density, and $< \delta N_e >$ is the perturbed electron density in the guiding-center coordinates[83, 82]. Ψ can be obtained from

$$\nabla^2\delta\Psi = -\nabla\cdot[\nabla\cdot < \delta\mathbf{P}_g > +\frac{1}{c}\delta\mathbf{J}_i\times\mathbf{B} + \frac{1}{c}\mathbf{J}_i\times\delta\mathbf{B}], \tag{2.29}$$

where $\delta\mathbf{J}_i = q_i\int\mathbf{v}\delta f_i d^3\mathbf{v}$, $\mathbf{J}_i = q_i\int\mathbf{v}\bar{f}_i d^3\mathbf{v}$, and $< \delta\mathbf{P}_g >= \int m_e\mathbf{v}\mathbf{v}\delta F_e d^3\mathbf{v}$.

The perturbed potential $\delta A_\perp$ is determined by the linearized perpendicular Ampeŕe's law

$$\nabla^2 \delta \mathbf{A}_\perp = -\frac{4\pi}{c}\delta \mathbf{J}_\perp, \tag{2.30}$$

with $\delta \mathbf{J}_\perp = (c/4\pi)\nabla \times (\delta B_\parallel \bar{\mathbf{b}})$. $A_\parallel$ is given by the linearized parallel Ampeŕe's law

$$(\nabla^2 - \frac{\omega_{pe}^2}{c^2})\delta A_\parallel = -\frac{4\pi}{c}(\delta J_{i\parallel} + < \delta J_{e\parallel} >), \tag{2.31}$$

where $< \delta J_{e\parallel} >= (q_e/m_e)\int p_\parallel \delta F_e d^3\mathbf{v}$, and $\delta J_{i\parallel} = q_i \int v_\parallel \delta f_i d^3\mathbf{v}$. $\delta B_\parallel$ is obtained from

$$\delta B_\parallel = 4\pi \frac{\delta\Psi + \bar{n}_i q_i (1+\rho_e^2\nabla_\perp^2)\delta\phi}{(1+\bar{\beta}_e)\bar{B}}. \tag{2.32}$$

Decompose $\delta A = \delta A_\parallel \bar{\mathbf{b}} + \delta \mathbf{A}_\perp + \nabla_\perp \xi$. To ensure the Coulomb gauge condition $\nabla \cdot \delta \mathbf{A} = 0$, ξ is

$$\nabla_\perp^2 \xi = -\nabla \cdot (\delta A_\parallel \bar{\mathbf{b}}). \tag{2.33}$$

The perturbed electric field is determined by the electron force balance equation

$$\bar{n}_e q_e \delta \mathbf{E} = \nabla \cdot \delta \mathbf{P}_e - \frac{1}{c}(\bar{J}_e \times \delta \mathbf{B} + \delta \mathbf{J}_e \times \bar{\mathbf{B}}). \tag{2.34}$$

The obtained $\delta \mathbf{E}$ and $\delta \mathbf{B} = \nabla \times \delta \mathbf{A}$ are use to advance the ion weighting function W_i, mean while, $\delta A_\parallel$ and $\delta\phi$ are used to advance the electron weighting function W_e.

2.1.4 Harris Equilibrium in the Gyrokinetic Coordinate

In the Harris equilibrium[92], the equilibrium ion velocity distribution in the six dimensional phase space $(\mathbf{x}, \mathbf{v})$ is given by

$$\bar{f}_{Hi} = \frac{n_{h0}}{(2\pi T_i/m_i)^{3/2}} \exp(-m_i[v_x^2 + (v_y - V_{di})^2 + v_z^2]/2T_i) \exp[-V_{di} q_i A_y(z)/T_i], \tag{2.35}$$

where V_{di} is the ion drift speed and

$$n_{h0}\exp[-V_{di}q_iA_y(z)/T_i] = n_H\mathrm{sech}^2(z/\mathrm{L}). \tag{2.36}$$

In the GeFi model, the drift Maxwellian velocity distribution of electrons in the guiding-center coordinate can be derived as follows. In the lab frame, the velocity distribution function of FK electrons is

$$\bar{f}_e = \frac{n_{h0}}{(2\pi T_e/m_e)^{3/2}}\exp(-m_e[v_x^2 + (v_y - V_{di})^2 + v_z^2]/2T_e)\exp[-V_{de}q_iA_y(z)/T_e], \tag{2.37}$$

where, V_{de} is the electron drift speed, in the Harris equilibrium, $V_{di}/T_i = -V_{de}/T_e$. The guiding center coordinate in current sheet normal is $Z = z + (\mathbf{v}\times\mathbf{b}/\Omega_e)\cdot\hat{\mathbf{z}}$, the unit vector of local magnetic field is $\hat{\mathbf{b}} = (B_G\hat{\mathbf{y}} + B_x\hat{\mathbf{x}})/B$, the $\hat{\xi} = \mathbf{b}\times\hat{\mathbf{z}}$ represents the gyrophase angle. The electron velocity can be written as

$$\mathbf{v} = v_x\hat{\mathbf{x}} + v_y\hat{\mathbf{y}} + v_z\hat{\mathbf{z}} = v_\parallel\hat{\mathbf{b}} + \mathbf{v}_\perp, \tag{2.38}$$

where $v_\parallel$ is the velocity parallel to $\hat{\mathbf{b}}$, $v_\perp$ is the perpendicular velocity. Noting that, $v_\parallel = v_yB_G/B + v_xB_x/B$, $v_\xi = v_xB_G/B - v_yB_x/B$, the electron speed can be written as

$$v_x^2 + v_y^2 + (v_y - V_{de})^2 = (v_\parallel - V_{de}\frac{B_G}{B})^2 + v_\perp^2 + \frac{B_x^2}{B^2}V_{de}^2 + 2v_\xi\frac{B_x}{B}V_{de}. \tag{2.39}$$

Noting that $z = Z + v_\xi/\Omega_e$, A_y can be expressed to the second order,

$$A_y(z) = A_y(Z) + A_y'(Z)\frac{v_\xi}{\Omega_e} + \frac{1}{2}A_y''(Z)\frac{v_\xi^2}{\Omega_e^2}. \tag{2.40}$$

The f_e is thus rewritten as

$$\bar{f}_e = \frac{n_{h0}}{(2\pi T_e/m_e)^{3/2}}\exp[-\frac{m_e[(v_\parallel - V_{de}B_G/B)^2 + v_\perp^2]}{2T_e}]\exp(-\frac{m_e}{2T_e}\frac{B_x^2}{B^2}V_{de}^2) \tag{2.41}$$

$$\times \exp[-\frac{V_{de} q_e A_y(z)}{T_e}](1 + \frac{V_{de}}{4}\frac{m_e}{T_e \Omega_e}\frac{B'_x}{B} v_\perp^2).$$

where we use the expansion

$$\exp[-\frac{V_{de}}{2}\frac{q_e}{T_e} A''_y(Z)\frac{v_\xi^2}{\Omega_e^2}] = 1 + \frac{V_{de}}{2}\frac{m_e}{T_e}\frac{B'_x}{B}\frac{m_e}{q_e B} v_\xi^2. \tag{2.42}$$

Take gyro-averaging $(2\pi)^{-1}\int_0^{2\pi} d\alpha$ on eq. (2.31), the electron distribution in guiding center coordinate is obtained as

$$F_e = \frac{n_h(Z)}{(2\pi T_e/m_e)^(3/2)} \exp[-\frac{m_e[(v_\parallel - V_{de} B_G/B)^2 + v_\perp^2]}{2T_e}] \exp(-\frac{m_e}{2T_e}\frac{B_x^2}{B^2} V_{de}^2)(1 + \frac{V_{de}}{2}\frac{B'_x}{T_e \Omega_e}\mu), \tag{2.43}$$

where $\mu = m_e v_\perp^2/2B$ is the magnetic moment.

2.2 GeFi Simulation Algebra

In the GeFi code, we use the second Runge-Kutta method to push particles, the Fourier analysis and cyclic reduction (FACR) method to solve elliptical boundary value problem (solving Poisson's equation), iteration method to solve coupled **A** and Φ equations, and four-point averaging method to carry out gyrokinetic interpolation. In this section, the four-point approach and FCAR method are introduced.

2.2.1 Four-point Numerical Approach for Gyrokinetic

In the continuous space, the gyro-averaging is expressed as $< >_\alpha \equiv (2\pi)^{-1}\int_0^{2\pi} d\alpha$, however in the discrete space, we can only take finite points on the orbit of particle to average the gyro-phase angle. Thus it is necessary to evaluate the accuracy of the discrete gyro-averaging method, which average the values of a physical quantity on the equal interval points of orbit.

Consider the averaged scalar potential $\bar{\Phi}$ at the gyrocenter position $\mathbf{R}$,

$$\bar{\Phi}(\mathbf{R}) =< \int d^3x\, \Phi(\mathbf{x})\delta(\mathbf{x}-\mathbf{R}-\rho) >_\alpha, \tag{2.44}$$

where $\mathbf{x}$ is the simultaneous position of the particle, ρ is the gyroradii. Expand $\Phi(\mathbf{x})$ in the Fourier $\mathbf{k}$ space,

$$\Phi(\mathbf{x}) = \sum_{\mathbf{k}} \Phi(\mathbf{k})\exp(i\mathbf{k}\cdot\mathbf{x}). \tag{2.45}$$

$< \bar{\Phi}(\mathbf{R}) >$ is expressed in the $\mathbf{k}$ space,

$$< \Phi(\mathbf{R}) >= \sum_{\mathbf{k}} \Phi(i\mathbf{k}\cdot\mathbf{R}) < \exp(i\mathbf{k}\cdot\rho) >_\alpha \tag{2.46}$$

Using the formula

$$< \exp(i\mathbf{k}\cdot\rho) >_\alpha = \mathrm{J}_0(\frac{k_\perp v_\perp}{\Omega}), \tag{2.47}$$

where $k_\perp$ and $v_\perp$ is the wavenumber and speed perpendicular to the local magnetic field, Ω is the gyrofrequency, J_0 is the zero-order Bessel function. $\bar{\Phi}(\mathbf{R})$ is finally written as

$$\bar{\Phi}(\mathbf{R}) = \sum_{\mathbf{k}} \Phi(i\mathbf{k}\cdot\mathbf{R})\mathrm{J}_0(\frac{k_\perp v_\perp}{\Omega}) \tag{2.48}$$

in the continuous space.

In the discrete space, the gyroaveraged scalar potential $< \Phi(\mathbf{x}_j) >_\alpha$ is

$$< \Phi(\mathbf{x}_j) >_\alpha = \sum_{\mathbf{k}} \Phi(i\mathbf{k}\cdot\mathbf{R}_j) < \exp(i\mathbf{k}\cdot\rho_j) >_\alpha, \tag{2.49}$$

where $\mathbf{R}_j$ and $\rho_\mathbf{j}$ is the gyrocenter and gyroradii of the jth particle respectively. Noting that

$$< \exp(i\mathbf{k}\cdot\rho_j) >_\alpha = \sum_{n=-\infty}^{\infty} \mathrm{J}_n(k_\perp\rho_j)\sin(2\pi n)\cot(\frac{n\pi}{M})/M, \tag{2.50}$$

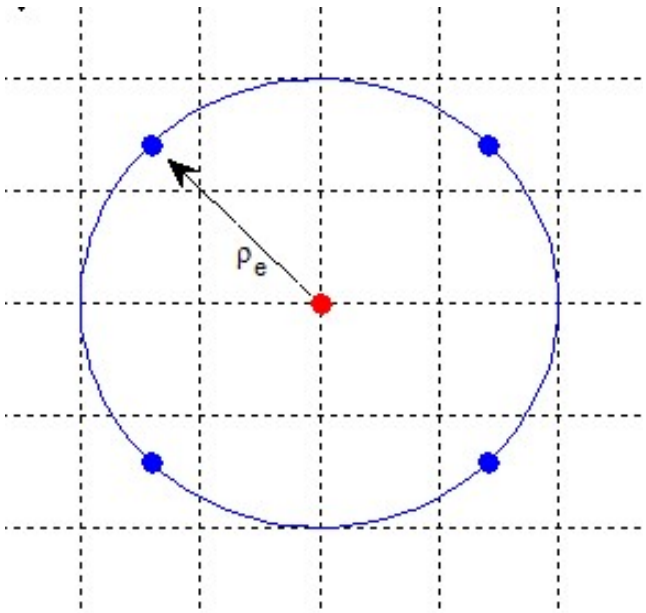

Figure 2.1: Four point averaging on the grids

M is the number of sampling points on the orbit, the four-point (M=4) gyroaveraged $<\Phi(\mathbf{x}_j)>_\alpha$ is

$$<\Phi(\mathbf{x}_j)>_{\alpha,M=4}=\sum_{\mathbf{k}}\Phi(\mathbf{k})\exp(i\mathbf{k}\cdot\mathbf{R}_j)[\mathrm{J}_0(k_\perp\rho_j)-\mathrm{J}_4(k_\perp\rho_j)-\mathrm{J}_{-4}(k_\perp\rho_j)+\cdots]. \quad (2.51)$$

When $k_\perp\rho_j \lesssim 2$, $\mathrm{J}_4 \ll \mathrm{J}_0$, thus the difference between $\bar{\Phi}(\mathbf{R})$ and $<\Phi(\mathbf{x}_j)>_{\alpha,M=4}$ is a smallness ($\sim \mathrm{J}_4$), mean while the gyrokinetic ordering requires $k_\perp\rho \leq 1$, so the four-point averaging shown in Fig.2.1 is practically suitable for the gyrokinetic simulation[90, 93].

2.2.2 Boundary Conditions and Field Equations Solving

As the section (2.1) showing, all field equations in the GeFi model are the elliptical partial differential equation (PDE), in this subsection, we show the numerical algebra of the elliptical PDE with the combined boundary conditions of the current sheet system. In the current sheet, the conducting boundary condition is applied on the direction of current sheet normal, the periodical boundary condition is applied on the directions along the anti-parallel magnetic field and/or the cross-field current. In order to show the algebra of solving field

equation in the GeFi code, we present the numerical solution of the Poisson's equation of scalar potential Ψ (eq. 2.19) in a 2-D plane (y-z) which contains the cross-field current (in y-axis) and the current sheet normal (in z-axis). Consider an elliptical boundary value problem

$$\begin{aligned} -\nabla^2\Psi = G, \;\; (y,z) \in (0,L_y)\times(0,L_z) \\ \Psi(y=0)=\Psi(y=L_y), \;\; \Psi(z=0)=\Psi(z=L_z)=0, \end{aligned} \tag{2.52}$$

where G represents the right side of eq. (2.19). The correspondent differential scheme is

$$\begin{aligned} -(\frac{1}{\Delta y^2}\delta_y^2+\frac{1}{\Delta z^2}\delta_z^2)\Psi_{j,k} = G_{j,k}, j=1,\cdots,M_y-1, \;\; k=1,\cdots,M_z-1, \\ \Psi_{0,k}=\Psi_{M_y,k}, k=0,\cdots,M_z, \\ \Psi_{j,0}=\Psi_{j,M_z}=0, j=0,\cdots,M_y, \end{aligned} \tag{2.53}$$

where M_y and M_z are grid numbers in y and z directions respectively, $\Delta y = 1/M_y$ and $\Delta z = 1/M_z$ are spatial steps, $\delta_y\Psi = \Psi_{j+1,k} - 2\Psi_{j,k} + \Psi_{j-1,k}$ is the center difference operator as well as $\delta_z\Psi = \Psi_{j,k+1} - 2\Psi_{j,k} + \Psi_{j,k-1}$.

Using discrete Fourier transform (DFT), Ψ and G can be expressed as

$$\begin{aligned} \Psi_{j,k} = \sum_{m=-(M_y-1)/2}^{(M_y-1)/2} \hat{\Psi}_{m,k} \mathrm{e}^{im\pi j\Delta y}, \\ \hat{\Psi}_{m,k} = \frac{1}{M_y}\sum_{j=0}^{M_y-1} \Psi_{j,k}\mathrm{e}^{-im\pi j\Delta y}, \end{aligned} \tag{2.54}$$

and

$$\begin{aligned} G_{j,k} = \sum_{m=-(M_y-1)/2}^{(M_y-1)/2} \hat{G}_{m,k} \mathrm{e}^{im\pi j\Delta y}, \\ \hat{G}_{m,k} = \frac{1}{M_y}\sum_{j=0}^{M_y-1} G_{j,k}\mathrm{e}^{-im\pi j\Delta y}, \end{aligned} \tag{2.55}$$

in the GeFi code, $M_y, M_z \equiv 2^n + 1$ (n is positive integer) to execute fast Fourier transform (FFT). It is proven that[94]

$$\delta_y^2 \Psi_{j,k} = \sum_{m=-(M_x-1)/2}^{(My+1)/2} -4\sin^2\frac{l\pi\delta x}{2}\hat{\Psi}_{m,k}\mathrm{e}^{im\pi j\Delta x}. \tag{2.56}$$

Based on eq. (2.43), (2.44) and (2.45), the Poisson's equation, eq. (2.42), can be rewritten in **k** space

$$\begin{aligned}(-\frac{4}{\Delta x^2}\sin^2\frac{j\pi\Delta x}{2} + \frac{1}{\Delta y^2}\delta_y^2)\hat{\Psi}_{j,k} &= \hat{G}_{j,k} \\ j = 1, \cdots, M_y - 1, \;\; k = 1, \cdots, M_z - 1,& \\ \hat{\Psi}_{j,0} = \hat{\Psi}_{j,M_z} &= 0.\end{aligned} \tag{2.57}$$

Solving eq. (2.46) as the tri-diagonal systems of equations[95], we can get the solution $\hat{\Psi}_{m,k}$ in the **k** space. The solution $\Psi j, k$ in real space is obtained by carrying out the inverse FFT on $\hat{\Psi}_{m,k}$.

2.3 Explicit Fully Kinetic Simulation Algebra

Since the GeFi is a novel model, it is necessary to benchmark against the widely used explicit fully kinetic (FK) particle-in-cell (PIC) model[91]. The simple description of the FK PIC model is as follows: (1) the current density on the grids is obtained by a spatial weighting method according to the records of the positions and velocities of particles, (2) the electric and magnetic field are determined by the integrals of Faraday's and Ampere's law

$$\frac{\partial \mathbf{B}}{\partial t} = -\nabla \times \mathbf{E}, \tag{2.58}$$

$$\frac{\partial \mathbf{E}}{\partial t} = c^2 \nabla \times \mathbf{B} - \frac{1}{\epsilon_0}\mathbf{J}, \tag{2.59}$$

(3) the ions and electrons are traced by the FK equations of motion

$$m\frac{d\mathbf{v}}{dt} = q(\mathbf{E} + \mathbf{v} \times \mathbf{B}), \tag{2.60}$$

$$\frac{d\mathbf{r}}{dt} = \mathbf{v}, \tag{2.61}$$

repeat (1)-(3) for the designed steps. Next, the numerical algorithms used in the FK PIC code are introduced. In the following discussion, we still focus on the geometry of the current sheet in which the cross-field current is in y and the current sheet normal is in z.

2.3.1 Fully Kinetic δf Scheme

In the fully kinetic δf model, for both electrons and ions, the perturbed particle weighting function $W_\alpha = \delta f / \bar{f}_\alpha$, is governed by the linearized Vlasov equation,

$$\frac{dW_\alpha}{dt} = q_\alpha \nabla \delta\phi \cdot \frac{\partial ln \bar{f}_\alpha}{\partial \mathbf{v}_\alpha}, \tag{2.62}$$

where subscript $\alpha = i, e$. The unperturbed orbits of particles follow,

$$\begin{aligned} \frac{d\mathbf{v}_\alpha}{dt} &= \frac{q_\alpha}{m_\alpha}\mathbf{v}_\alpha \times \mathbf{B}_0, \\ \frac{d\mathbf{x}_\alpha}{dt} &= \mathbf{v}_\alpha. \end{aligned} \tag{2.63}$$

The perturbed magnetic and electric field are given by Faraday's and Ampeŕe's law,

$$\frac{\partial \delta\mathbf{E}}{\partial t} = -\nabla \times \delta\mathbf{B}, \tag{2.64}$$

$$\frac{\partial \delta\mathbf{E}}{\partial t} = c^2 \nabla \times \delta\mathbf{B} - \frac{1}{\epsilon_0}\delta\mathbf{J}, \tag{2.65}$$

where $\delta\mathbf{J} = \int q_i \delta f d^3v$.

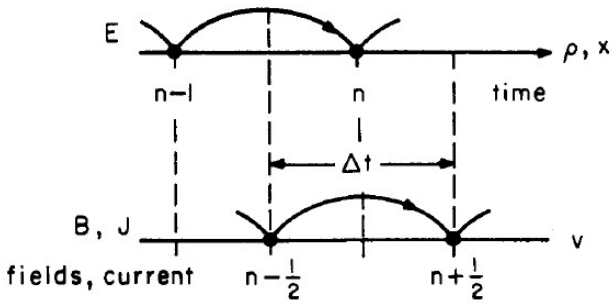

Figure 2.2: Temporal layout of fields and quantities used in the leap-frog scheme. $\mathbf{E}$,$\mathbf{x}$,ρ are advanced at step n, $\mathbf{B}$,$\mathbf{v}$,$\mathbf{J}$ are advanced at step $n - \frac{1}{2}$.[91]

2.3.2 Field Integration

The fields are integrated forward using their time derivatives as given in eq. (2.47) and (2.48). The leap-frog scheme[91] is applied on the coupled field equations in which the time derivatives of $\mathbf{B}(\mathbf{E})$ on the left hand side with $\mathbf{B}(\mathbf{E})$ appearing on the right hand side. Fig. 2.2 shows the leap-frog scheme that advances $\mathbf{E}$, the position of particle $\mathbf{x}$ and the charge density ρ at the integer steps, $\mathbf{B}$, the velocity of particle $\mathbf{v}$, the current density $\mathbf{J}$ at the half integer steps. The centered time differential, which is accurate to the second order, is applied.

We are now ready to difference Maxwell's equations explicitly in a very simple way whose accuracy is second in space and time[91]. Particularly the time derivative becomes

$$(\partial_t E_x)^{n+1/2}_{j+1/2,k} \equiv \frac{E^{n+1}_{x,j+1/2,k} - E^{n}_{x,j+1/2,k}}{\Delta t} \tag{2.66}$$

where $E^n_{x,j+1/2,k} \equiv E_x([j+1/2]\Delta x, k\Delta y, n\Delta t)$, etc. The spatial differences ∂_x and ∂_y are defined analogously. The gradient ∇ becomes ∂_x and ∂_y. Noting that, these operators, applied to fields defined on our space-time grids, commute. Therefore the algebra of the difference equations are same as the correspondent differential equations.

The difference Faraday's and Ampere's law are,

$$(\partial_t B_z)^n_{j+1/2,k+1/2} = -c(\partial_x E_y - \partial_y E_x)^n_{j+1/2,k+1/2} \tag{2.67}$$

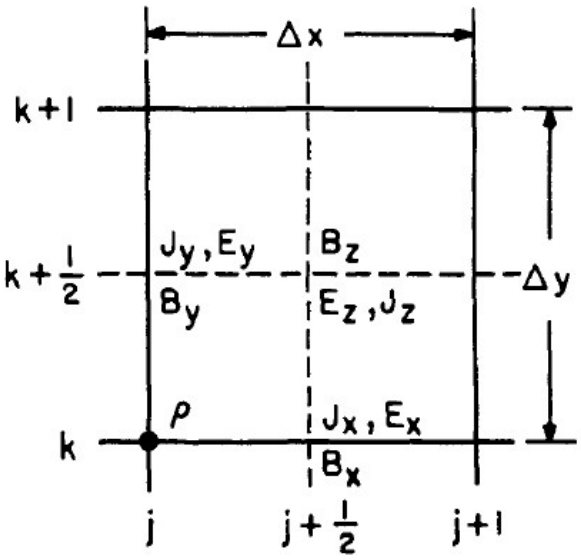

Figure 2.3: Spatial Layout on the grids of 2-D fields (E_x, E_y, E_z) and the the source terms (ρ,J_x, J_y, $\delta\phi$) during the integration of the difference field equations [91]. Here 'Δx' is corrected to be 'Δy'.

$$(\partial_t E_x)^{n+1/2}_{j+1/2,k} = (c\partial_y B_z - J_x)^{n+1/2}_{j+1/2,k} \tag{2.68}$$

$$(\partial_t E_y)^{n+1/2}_{j,k+1/2} = (-c\partial_x B_z - J_y)^{n+1/2}_{j,k+1/2}. \tag{2.69}$$

When $B_z^{n-1/2}$ and $\mathbf{E}^n$ are known, eq.(2.52) gives $B_z^{n+1/2}$. $\mathbf{E}$ is then advanced in the same way. For example, (2.53) and (2.54) are rewritten to

$$\frac{E^{n+1}_{x,j+1/2,k} - E^n_{x,j+1/2,k}}{\Delta t} = c\frac{B^{n+1/2}_{z,j+1/2,k+1/2} - B^{n+1/2}_{z,j+1/2,k-1/2}}{\Delta y} - J^{n+1/2}_{x,j+1/2,k} \tag{2.70}$$

$$\frac{E^{n+1}_{y,j,k+1/2} - E^n_{x,j,k+1/2}}{\Delta t} = -c\frac{B^{n+1/2}_{z,j+1/2,k+1/2} - B^{n+1/2}_{z,j-1/2,k+1/2}}{\Delta z} - J^{n+1/2}_{x,j+1/2,k}. \tag{2.71}$$

The code alternates, advancing $\mathbf{E}$ and $\mathbf{B}$, as shown in Fig. 2.3. The new quantities will replace the old one on the grids each step. It is no need to store the values in the memory more than one time.

2.3.3 Boundary Conditions

The fields at the boundary of y direction with the periodical condition can be written as

$$B_x(j+1/2,0) = B_x(j+1/2,M_y-1), \tag{2.72}$$

$$B_x(j+1/2,1) = B_x(j+1/2,M_y), \tag{2.73}$$

$$B_y(j,1/2) = B_y(j,M_y-1/2),$$

$$B_y(j,3/2) = B_y(j,M_y+1/2), \tag{2.74}$$

$$E_z(j+1/2,1/2) = E_z(j+1/2,M_y-1/2),$$

$$E_z(j+1/2,3/2) = E_z(j+1/2,M_y+1/2), \tag{2.75}$$

where $k=0$ ($k=M_y$) is the terminal of left (right) boundary shown in Fig. 2.3.

The velocity and position of a particle which pass through the y- boundary obey, if $j<0$,

$$v_y(j,k) = v_y(j,k+M_y), \;\; v_z(j,k) = v_z(j,k+M_y), \tag{2.76}$$

$$y(j,k) = y(j,k+M_y), \;\; z(j,k) = z(j,k+M_y), \tag{2.77}$$

if $j>0$,

$$v_y(j,k) = v_y(j,k+M_y), \;\; v_z(j,k) = v_z(j,k+M_y), \tag{2.78}$$

$$y(j,k) = y(j,k+M_y), \;\; z(j,k) = z(j,k+M_y). \tag{2.79}$$

In the z-direction, the fields obey the conducting wall boundary condition, in the field advance, only the tangential component of $\mathbf{E}$ is needed

$$E_x(1/2,k) = E_x(M_z+1/2,k) = 0, \tag{2.80}$$

$$E_y(0,k+1/2) = E_y(M_z,k+1/2) = 0, \tag{2.81}$$

where $j = 1/2$ ($j = M_z + 1/2$) is the terminal of bottom (top) boundary shown in Fig. 2.3. The normal component of $\mathbf{B}$ is

$$B_z(1/2,k+1/2) = B_z(M_z+1/2,k+1/2). \tag{2.82}$$

The particles will be reflected by the conducting wall boundaries, if $k < 0$,

$$z(j,k) = -z(j,k), \tag{2.83}$$

if $k > 0$,

$$z(j,k) = -z(j,k) + 2M_z. \tag{2.84}$$

2.3.4 Correction for Charge Conservation

In addition to two curl equations, there are still two divergence equations in the Maxwell sets

$$\nabla \cdot \mathbf{E} = \rho, \nabla \cdot \mathbf{B} = 0. \tag{2.85}$$

It is proven that the divergence of $\mathbf{E}$ and $\mathbf{B}$ are always correct, if the continuity of charge,

$$\nabla \cdot \mathbf{J} - \frac{\partial \rho}{\partial t} = 0, \tag{2.86}$$

is satisfied at all times.

However, neither the current nor the charge density, which is obtained by the weighting method on the grids, satisfies the continuity equation. Moreover, people found that calculating a charge-conservative **J** according to ρ by a weight method is hard due to the rapid rising noise level in the electromagnetic fields[96, 97]. Here, the method ensuring the continuity by using a nonconservative **J** is introduced as follows.

E is advanced using **J** in Ampere's law. An **E** depending on a nonconservative **J** does not satisfy the equation of continuity in generally. In order to ensuring the continuity, the correction form of **E** is invented

$$\mathbf{E}' = \mathbf{E} - \nabla\delta\phi, \tag{2.87}$$

where $\mathbf{E}'$ satisfies $\nabla \cdot \mathbf{E}' = \rho$. Taking divergence on the both side of eq. (2.72), we have

$$\nabla \cdot (\mathbf{E} - \nabla\delta\phi) = \rho. \tag{2.88}$$

Thus the corrected potential $\delta\phi$ is obtained though the Poisson's equation,

$$\nabla^2\delta\phi = \nabla \cdot \mathbf{E} - \rho. \tag{2.89}$$

In the simulations, the above correction procedure is executed between several decades of steps to satisfy the continuity.

2.3.5 Boris Scheme

In the FK code, we use the Boris scheme[98] to push electrons and ions. The electric and magnetic fields applying on the particles are obtained from the nearby grids through cloud-in-cell weighting method[99]. We can calculate the velocity of the particles by the

time-center difference form of Eq. (2.49)

$$\frac{\mathbf{v^{n+1/2}} - \mathbf{v^{n-1/2}}}{\Delta t} = \frac{q}{m}[\mathbf{E} + \frac{\mathbf{v^{n+1/2}} + \mathbf{v^{n-1/2}}}{2} \times \mathbf{B}] \tag{2.90}$$

where the superscripts indicate the time step. In the above difference from, the unknown variable $\mathbf{v}^{n+1/2}$ is on both the left and the right hand side, thus Eq. (2.75) is in the implicit form. Calculating $\mathbf{v}^{n+1/2}$ needs to solve linear equation sets, a splitting scheme is invented to transfer eq. (2.75) to explicit form. First, move a particle by the electric field in the half time step,

$$\mathbf{v}^{-} = \mathbf{v}^{n+1/2} + \frac{q\mathbf{E}}{m}\frac{\Delta t}{2}. \tag{2.91}$$

Noting that, $\mathbf{t} \equiv (q\mathbf{B})\Delta t/2$, the vector $\mathbf{v}'$ is then

$$\mathbf{v}' = \mathbf{v}^{-} + \mathbf{v}^{-} \times \mathbf{t} \tag{2.92}$$

Next, the complementary vector $\mathbf{v}^{+}$ can be calculated as

$$\mathbf{v}^{+} = \mathbf{v}^{-} + \mathbf{v}' \times \mathbf{s}, \tag{2.93}$$

where $\mathbf{s} = 2\mathbf{t}/1 + t^2$. The eq. (2.73) - (2.75) show the the rotation of the particle under $\mathbf{B}$. Then push the particle in the rest half time step and obtain $\mathbf{v}^{n+1/2}$,

$$\mathbf{v}^{n+1/2} = \mathbf{v}^{+} + \frac{q\mathbf{E}}{m}\frac{\Delta t}{2}. \tag{2.94}$$

The Boris scheme has the second order accuracy and shows good energy conservative. Fig. 2.4 shows the trajectory of a charge particle in an uniform background magnetic field, the red dished lines are obtained from the numerical calculation of Boris scheme, the blue solid line shows the orbit of the analytic results, the trajectory from numerical calculation exactly agree with the theory orbit.

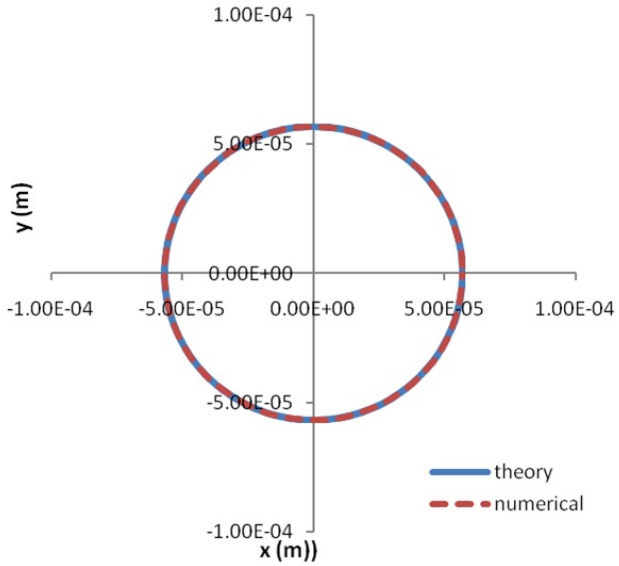

Figure 2.4: Trajectory of a charge particle in an uniform field, the red dashed lines are obtained from numerical calculation, blue solid line show the orbits from the analytic calculation.

Chapter 3

Electrostatic Results

In this chapter, the current sheet instability is simulated with the GeFi code in the ES limit. In the ES limit, it is found that only LHDI is present. Therefore, our introduction below will focus on the LHDI only.

3.1 Introduction

The LHDI has long attracted attention as a possible source of the anomalous resistivity.

LHDI in a Harris current sheet has been investigated for decades[58, 59, 60, 108, 63, 64]. A nonlocal kinetic theory for a Harris sheet without a guide field found that the LHDI is well localized at the edge of the current sheet[60]. Here, the guide field denotes the external magnetic field component applied along the current direction. On the other hand, a finite guide field was found to have a significant effect on the instability. The two-fluid theory of Yoon and Lui [108] showed that the most unstable LHDI is an oblique mode and the maximal growth rate occurs at $\vec{k} \cdot \vec{B} = 0$, where $\vec{k}$ is the wave vector normal to the nonuniformity direction. Daughton[63, 64] used a linear Vlasov code to investigate the linear LHDI and drift kink instability in a Harris sheet and showed that the eigenmode structure is modified by the presence of the finite guide field, but the calculation only considered the spatial planes with $\vec{k} \cdot \vec{B} = 0$. A two-dimensional (2-D) fully kinetic (FK) particle simulation was also carried out in the rotated plane with the parallel wave number $k_{\|} = 0$, and the results were compared with those from the linear Vlasov calculation[64]. Based on a gyrokinetic (GK) electron and fully kinetic unmagnetized ion assumption, Tummel et al.[62] developed an electrostatic eigenmode theory to examine the LHDI. It was found that under a certain k_y, where k_y is the component of wave number along the current direction, the most unstable LHDI can peak

at locations where $\vec{k} \cdot \vec{B} \neq 0$, or $k_{\parallel} \neq 0$. The unstable modes peaked at $\vec{k} \cdot \vec{B} \neq 0$ could have a significant consequence on the anomalous resistivity because with the finite $k_{\parallel}$, electrons can resonate with waves and be scattered; leading to the anomalous resistivity. Therefore, it is necessary to scan through the entire three-dimensional (3-D) $\vec{k} \cdot \vec{B} \neq 0$ spectral space for the LHDI in the current sheet. It is the purpose of this chapter to calculate the complete eigenmode structure of LHDI in a Harris sheet with a 3-D particle simulation.

Since the physics of LHDI is directly related to m_i/m_e, it is necessary to use a realistic mass ratio to assure a proper scale separation between electrons and ions, which is very important for understanding the linear and nonlinear physics related to reconnection. Due to the limitation in the computing resources, most of the previous FK particle simulations of magnetic reconnection and LHDI are based on 2-D models[113, 115, 65, 114], and the 3-D properties of LHDI has not been systematically simulated.

In this chapter, the electrostatic LHDI is investigated using the 3-D GeFi particle simulation code[83, 82]. This study focuses on the linear LHDI, and thus a linearized δf scheme is used in the simulation. The GeFi simulation results are compared with the results from the linearized FK simulation. Both simulations adopt the particle-in-cell (PIC) approach. The eigenmode structure and growth rate of the LHDI in the full 3-D space are calculated. Effects of finite guide field B_G and mass ratio m_i/m_e are investigated. The simulation results are compared with the theoretical finding of Tummel et al.[62] based on the GeFi eigenmode theory.

3.2 Simulation Model

3.2.1 GeFi Linearized δf Scheme

In the GeFi particle simulation scheme, electrons are treated as GK particles[86, 87, 88, 89], and ions are treated as FK particles. The GeFi model is suitable for the process in which the characteristic frequency ω range from the Alfvenic frequency to the lower-hybrid frequency, smaller than the electron cyclotron frequency Ω_e. Wave modes relevant

to the current sheet instabilities associated with magnetic reconnection fall inside this range of dynamic scales. The GeFi simulation model has been benchmarked against the fully kinetic analytical theory[129, 83, 82] for uniform plasmas and against the GK eigenmode theory[54] for the tearing mode. This model has also been used to study instabilities in a two-dimensional (2-D) plane of the Harris current sheet that contains a guide field [130, 84].

For the linearized scheme, the FK ion equations of motion in unperturbed orbits are

$$\begin{aligned} \frac{d\mathbf{p}_i}{dt} &= -q_i\nabla(\bar{\phi}_0 - \mathbf{v}_i\cdot\bar{\mathbf{A}}_0/c), \\ \frac{d\mathbf{x}_i}{dt} &= \mathbf{v}_i, \end{aligned} \tag{3.1}$$

where q_i is the ion charge, $\mathbf{p}_i$ is the ion canonical momentum, $\mathbf{x}_i$ is the ion position, $\mathbf{v}_i$ is the ion velocity, ϕ_0 and $\mathbf{A}_0$ are the equilibrium scalar and vector potentials, respectively, and the 'bar' indicates the background quantities. The perturbed ion particle weighting function $W_i = \delta f_i/\bar{f}_i$ is governed by the linearized Vlasov equation in the six-dimensional phase space $(\mathbf{x}, \mathbf{v}_i)$,

$$\frac{dW_i}{dt} = q_i\nabla\delta\phi\cdot\frac{\partial ln\bar{f}_i}{\partial\mathbf{v_i}}. \tag{3.2}$$

Here, $\bar{f}_i$ is the equilibrium ion distribution function, and $\delta\phi$ is the perturbed scalar potential.

In the GK ordering for electrons, $\omega/\Omega_e \sim \rho_e/L \sim k_\parallel\rho_e \sim \delta B/B \sim \epsilon$ and $k_\perp\rho_e \sim 1$, where ρ_e is the electron Larmor radius, L is the macroscopic background plasma scale length, δB is the perturbed magnetic field on the microscopic wave scale lengths, and ϵ is a smallness parameter. Following the above GK ordering for electrons, the rapid electron gyromotion is removed in the calculation, which significantly enhances the computation power and allows for the calculation of physical problems with a realistic ion-to-electron mass ratio. The GK particle approximation can be used for reconnection under a finite guide field. The gyrocenter equations of motion in unperturbed orbits for the parallel electron canonical momentum, $p_\parallel = m_e v_{e\parallel} + q_e A_\parallel/c$, and for the electron gyrocenter position, $\mathbf{R}$, are given by

[86, 87, 88, 89]

$$\begin{aligned}\frac{dp_\parallel}{dt} &= -\mathbf{b}^*\cdot[q_e < \nabla\phi_0^* > +\mu\nabla\bar{B}_0], \\ \frac{d\mathbf{R}}{dt} &= v_{e\parallel}\mathbf{b}^* + \frac{c}{q_e\bar{B}}\bar{\mathbf{b}}\times[q_e < \nabla\phi_0^* > +\mu\nabla\bar{B}_0],\end{aligned} \tag{3.3}$$

where m_e and $v_{e\parallel}$ are the electron mass and electron parallel velocity, respectively, q_e is the electron charge, μ is the magnetic moment, $\bar{\mathbf{B}}_0$ is the background magnetic field, $\bar{\mathbf{b}} = \bar{\mathbf{B}}_0/\bar{B}_0$, and $\mathbf{b}^* = \bar{\mathbf{b}} + (v_{e\parallel}/\bar{\Omega}_e)\bar{\mathbf{b}}\times(\bar{\mathbf{b}}\cdot\nabla)\bar{\mathbf{b}}$. $\phi_0^* = \bar{\phi}_0 - \mathbf{v}\cdot\bar{\mathbf{A}}_0/c$ is the unperturbed scalar potential, $< \ldots >$ represents gyro-averaging, and $\perp$ and $\parallel$ denote components perpendicular and parallel to the background magnetic field, respectively. The weighting function of the GK electrons obeys

$$\begin{aligned}\frac{dW_e}{dt} = &-\frac{c\bar{\mathbf{b}}}{q_e\bar{B}_0}\times(q_e < \nabla\delta\phi >)\cdot\frac{\partial ln\bar{F}_e}{\partial\mathbf{R}} \\ &+\mathbf{b}^*\cdot(q_e < \nabla\delta\phi >)\cdot\frac{\partial ln\bar{F}_e}{\partial p_\parallel}.\end{aligned} \tag{3.4}$$

The linearized electrostatic GK Poisson's equation in a nonuniform plasma can be expressed as

$$\nabla_\perp\cdot[(1+\frac{\bar{\omega}_{pe}^2}{\bar{\Omega}_e^2})]\nabla_\perp\delta\phi = -4\pi(q_i\delta n_i + q_e < \delta N_e >), \tag{3.5}$$

where $\bar{\omega}_{pe}$ is the electron plasma frequency, δn_i is the perturbed ion number density, and $< \delta N_e >$ is the perturbed electron density in the guiding-center coordinates[83, 82].

3.2.2 Initial and Boundary Conditions

The simulation is performed in the 3-D space, with the coordinate z along the current sheet normal, the antiparallel field component B_x, and the guide field B_G in the y direction. The initial magnetic field is given by

$$\mathbf{B}_0(z) = \hat{x}B_{x0}\tanh(z/L) + \hat{y}B_G, \tag{3.6}$$

where L is the half-width of the current sheet, and B_G is a constant. We assume that the ion and electron temperatures, T_i and T_e, are constant everywhere in the domain. For a given ion beta value β_{i0}, the initial density in the Harris sheet is expressed as

$$n_{i0} = n_H \mathrm{sech}^2(z/L) + n_{b0}, \tag{3.7}$$

where n_{b0} is the background density. The peak ion density n_H in the current is obtained from the total pressure balance

$$n_H(T_i + T_e) = \frac{1}{8\pi} B_{x0}^2, \tag{3.8}$$

where T_i and T_e are in units of energy. The equilibrium drift Maxwellian velocity distribution of ion population in the Harris sheet is given by

$$f_{Hi} = \frac{n_H \mathrm{sech}^2(z/L)}{(2\pi T_i/m_i)^{3/2}} \exp(-\frac{m_i}{2T_i}[v_x^2 + (v_y - v_{di})^2 + v_z^2]), \tag{3.9}$$

where $v_{di} = 2cT_i/q_i B_0 L$ is the ion drift speed. The GK equilibrium distribution function for the Harris sheet electrons takes the form[84]

$$\begin{aligned} f_{He,g} = \frac{n_H \mathrm{sech}^2(z/L)}{(2\pi T_i/m_i)^{1/2}} \frac{B_0}{T_e} \exp(-\frac{2\mu B_0 + m_e(v_\parallel - v_{de\parallel})^2}{2T_e}) \\ \times (1 + \frac{v_{de}}{2T_e\Omega_e}\frac{dB_x}{dz}) \exp(\frac{B_x^2}{B_0^2}\frac{m_e v_{de}^2}{2T_e}) \end{aligned} \tag{3.10}$$

where v_{de} is the electron drift speed. For the Harris current sheet, $v_{de}/T_e = -v_{di}/T_i$. Note that the initial distribution functions given above are taken as the equilibrium distribution functions in the δf calculation.

The periodic boundary conditions are applied at $x = 0$, l_x and $y = 0$, l_y. The conducting boundary conditions are applied at $z = \pm l_z/2$, with $\delta\phi = 0$ and $\delta\mathbf{A} = 0$.

3.2.3 Parameters and Normalization

The parameters used in the simulation are described as follows. The half-width of the current sheet is $L = 0.25\text{-}0.5\rho_{i0}$, where ρ_{i0} is the ion Larmor radius in the asymptotic magnetic field B_0. The system lengths are chosen as $l_x = 0.75\text{-}15\rho_{i0}$ in the x direction, $l_y = 0.1\text{-}1.5\rho_{i0}$ in the y direction, and $l_z = 5\rho_{i0}$ in the z direction. The grid number is $N_x \times N_y \times N_z = 16 \times 16 \times 128\text{-}32 \times 32 \times 512$. The number of particles in each cell is 100-400. The guide field $B_G/B_{x0} = 0.1\text{-}1$. The electron beta is $\beta_{e0} = 0.0033\text{-}0.016$, the ion-to-electron temperature ratio is $T_i/T_e = 10$, the mass ratio $m_i/m_e = 459\text{-}1836$, and $\omega_{pe}/\Omega_{ce} = 1\text{-}10$, where $\omega_{pe} = (4\pi n_0 e^2/m_e)^{1/2}$ is the electron plasma frequency and $\Omega_{ce} = eB_0/m_e c$ is the electron cyclotron frequency.

In this paper, the magnetic field is normalized to $B_0 = (B_{x0} + B_G)^{1/2}$. The electric potential is normalized to T/e. The normalized background density $n_{b0} = 0\text{-}1$, while $n_H = 5.6\text{-}27.5$ in the cases shown. The real frequency and growth rate are normalized to the asymptotic ion cyclotron frequency, Ω_{i0}. The wave number is normalized to ρ_{i0}^{-1}.

3.2.4 Fully Kinetic δf Scheme

In the fully kinetic δf model, for both electrons and ions, the perturbed particle weighting function $W_\alpha = \delta f/\bar{f}_\alpha$, is governed by the linearized Vlasov equation,

$$\frac{dW_\alpha}{dt} = q_\alpha \nabla \delta\phi \cdot \frac{\partial ln \bar{f}_\alpha}{\partial \mathbf{v}_\alpha}, \tag{3.11}$$

where subscript $\alpha = i, e$. The unperturbed orbits of particles follow,

$$\begin{aligned} \frac{d\mathbf{v}_\alpha}{dt} &= \frac{q_\alpha}{m_\alpha}\mathbf{v}_\alpha \times \mathbf{B}_0, \\ \frac{d\mathbf{x}_\alpha}{dt} &= \mathbf{v}_\alpha. \end{aligned} \tag{3.12}$$

The perturbed electrostatic potential is given by Poisson's equation,

$$\nabla^2 \delta\phi = -4\pi(\int d\mathbf{v}_i q_i \delta f_i + \int d\mathbf{v}_e q_e \delta f_e). \tag{3.13}$$

3.3 Results of Investigation

In the following, we show the simulation results of current sheet instability. Cases of 2-D LHDI with $k_x = 0$ and $k_y \neq 0$ are presented first. Note that there exists no (2-D) electrostatic unstable mode for $k_y = 0$. The full 3-D results with $k_x \neq 0$ and $k_y \neq 0$ are then presented.

3.3.1 Results with $k_x = 0$ and $k_y \neq 0$: 2-D cases

In the cases with $k_x = 0$ and $k_y \neq 0$, the wave vectors of LHDI are in the 2-D (yz) plane that contains the guide field and the current sheet normal. The current and drift direction are in this plane, and so are the LHDI modes. For typical 2-D cases, the dispersion relation of LHDI modes obtained from the GeFi particle simulation are compared with the GeFi eigenmode theory and the FK particle simulation.

2-D Eigenmode

Fig. 1 shows the results of case 1, in which $L = 0.25\rho_{i0}$, $\beta_{e0} = 0.016$, $B_G/B_{x0} = 0.1$, $\omega_{pe}/\Omega_{ce} = 1.0$, and the back ground plasma density is set to be zero, i.e., $n_{b0} = 0$. Only modes with $k_y\rho_{i0} = \pm 35.23$ are kept, The left column of Fig. 1 presents the GeFi simulation results, while the right column shows the corresponding FK simulation results. Fig. 1(a) shows contours of the perturbed electrostatic potential $\delta\phi$ in the y-z plane, while Fig. 1(b) shows the eigenmode structure $\delta\tilde{\phi}$, which is the absolute value of the eigenfunction. The dashed lines in Figs. 1(a) and 1(b) mark the position $z = \pm L$, $\pm 2L$, and $\pm 3L$. Instability in the electrostatic potential is present, which is located at the edge of the current sheet, within $L < |z| < 2L$. Fig. 1(c) shows $|\delta\tilde{\phi}|$ of the instability as a function of time. An exponential

growth is seen, with a linear growth rate of $\gamma/\Omega_{i0} = 22.3$ obtained in the GeFi simulation and $\gamma/\Omega_{i0} = 21.1$ obtained from the FK simulation. The electrostatic instability obtained from the simulations is the LHDI[63]. The results from the GeFi simulation are in excellent agreement with those from the FK simulation in terms of the linear growth rate and mode structure. As expected, higher frequency fluctuations are also present in the growth curve of the FK results, while the growth curve obtained from the GeFi model is much smoother due to the removal of fluctuations with $\omega \sim \Omega_e$. The LHDI propagates in the $+y$ direction, i.e., direction of the ion drift, at both edges of the current sheet. Moreover, as shown in Figs. 1(a) and 1(b), there is little $\delta\phi$ near the center of the current sheet. The two eigenmodes on the two sides of the current sheet are independent.

To show this property, we show two GeFi simulation runs with even and odd initial perturbations. The initial perturbation in one run follows a cosine function across the current sheet, whereas in the other run the initial perturbation follows a sine function. By choosing identical initial perturbation on the $z < 0$ side in the two runs, the perturbations on the $z > 0$ side are of opposite signs. The left and right columns of Fig. 2 show the eigenmodes obtained from the two runs with a cosine and sine initial perturbations in $\delta\phi$, respectively. Shown in Figs. 2(a), 2(b), and 2(c) are the real space contours, eigenfunction structure, and the time growth of $|\delta\tilde{\phi}|$, respectively. The real (imaginary) part of the eigenfunction is shown by the solid (dotted) lines in Fig. 2(b). The eigenvalues on both sides of the sheet and in both runs are identical, with the growth rate of $\gamma/\Omega_{i0} = 22.3$ and real frequency of $\omega/\Omega_{i0} = 242.1$, as seen in Fig. 2(c). The structures of the eigenfunction in $z < 0$ for the two runs are identical. whereas in $z > 0$ they are of opposite signs in the two runs. In general, the sign and strength of eigenfunctions of these two independent eigenmodes are determined by their initial perturbations.

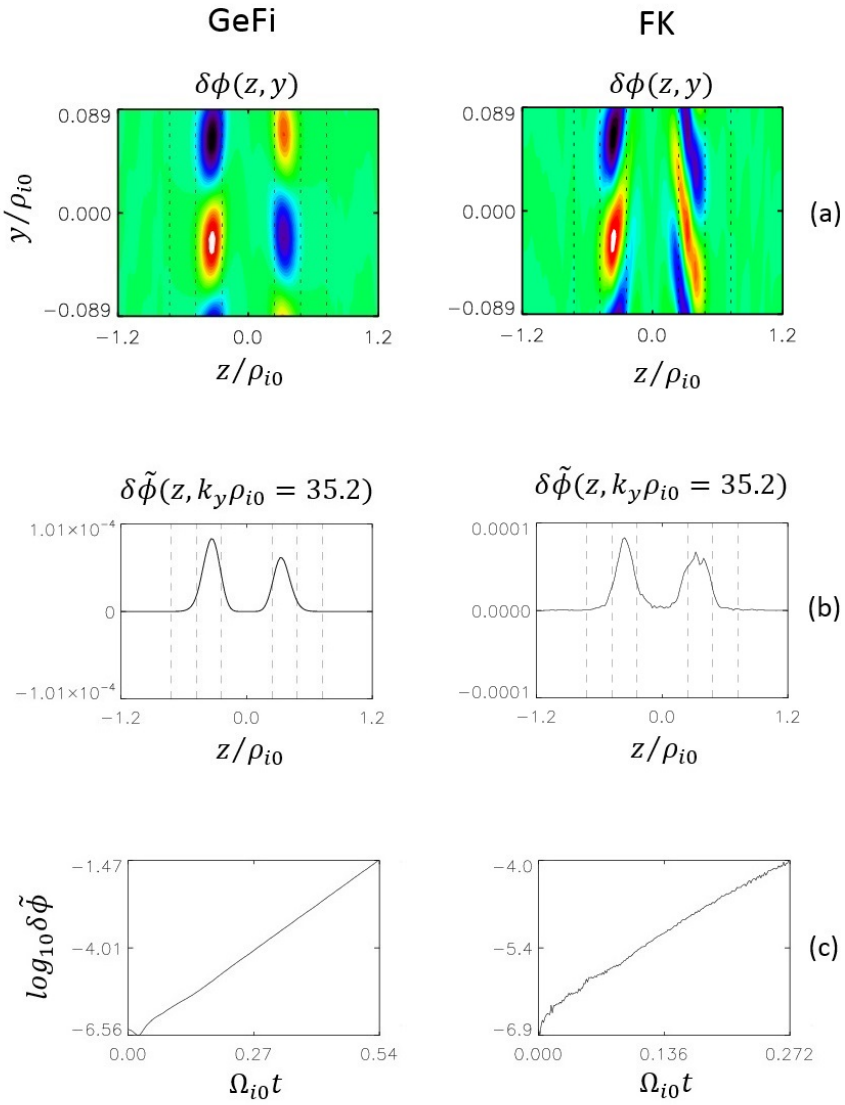

Figure 3.1: FK and GeFi simulation results for case 1, with $L/\rho_{i0} = 0.25$, $T_e/T_i = 0.1$, $\beta_{e0} = 0.016$, $n_{b0} = 0.0$, $B_G/B_{x0} = 0.1$, $\omega_{pe}/\Omega_{ce} = 1.0$ and $k_y\rho_{i0} = 35.23$. (a) Contours of the perturbed electrostatic potential $\delta\phi$ from the GeFi (left) and FK (right) models. The dashed lines mark $z = \pm L$, $\pm 2L$, and $\pm 3L$. (b) The solid line presents the absolute value of the eigenfunction obtained from the GeFi (left) and FK (right) simulations. The dashed lines mark $z = \pm L$, $\pm 2L$, an $\pm 3L$. (c) The growth of the eigenmode obtained from the GeFi (left) and FK (right) simulations.

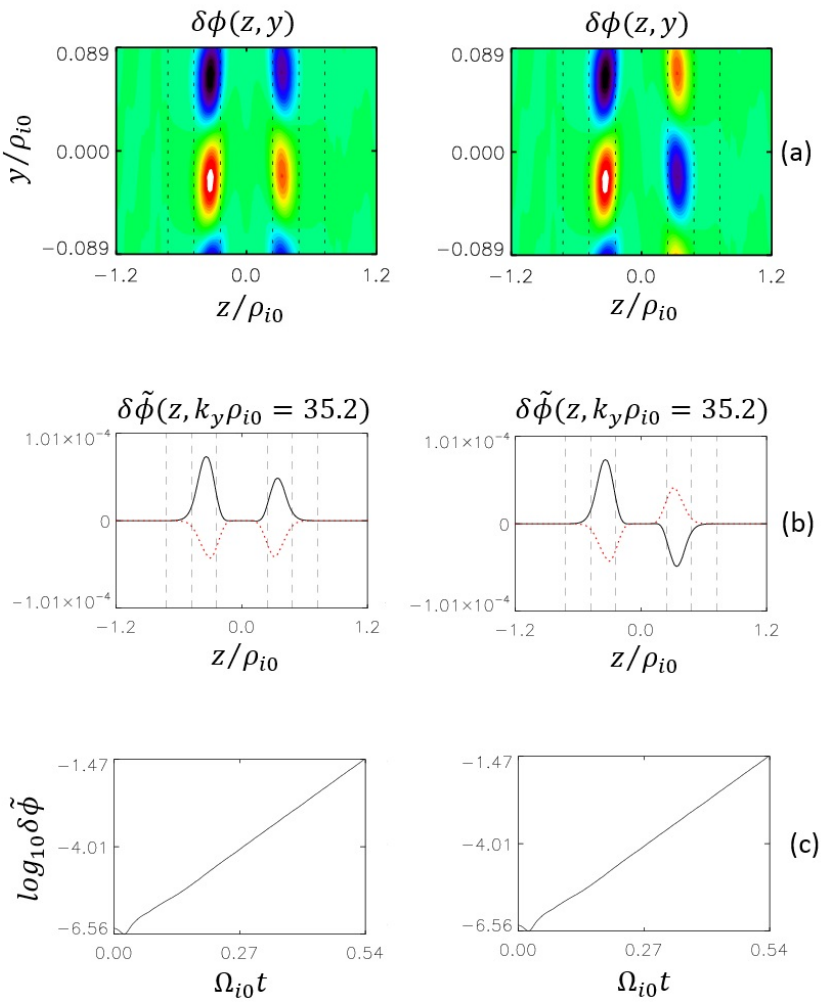

Figure 3.2: LHDIs with even (left column) and odd (right column) initial perturbations. The parameters are the same as those in Fig. 1. (a) Contours of $\delta\phi$. The dashed lines mark $z = \pm L$, $\pm 2L$, and $\pm 3L$. (b) The real (solid lines) and imaginary (dashed lines) part of eigenfunction. The thin vertical dashed line marks $z = \pm L$, $\pm 2L$,$\pm 3L$. (c) The growth rate of eigenmode.

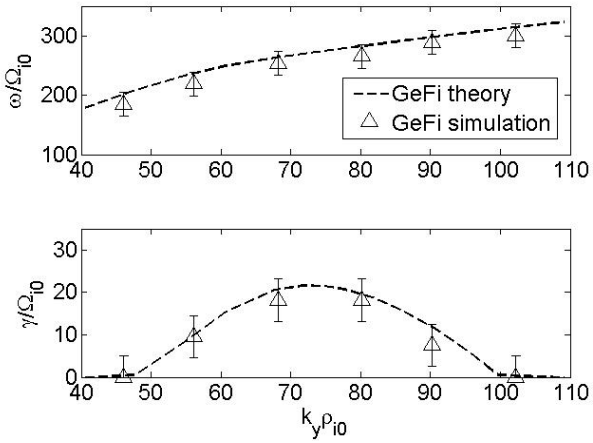

Figure 3.3: Comparison of the frequency (top plot) and growth rate (bottom plot) between the GeFi simulation (triangles) and the GeFi eigenmode theory (dashed lines) for $L = 0.23\rho_{i0}$, $\beta_{e0} = 0.0033$, $B_G/B_{x0} = 0.1$, $\omega_{pe}/\Omega_{ce} = 10$, and $n_b = 0.5$.

Dispersion Relation of 2-D LHDI

The open circles with error bars in Fig. 3 show the real frequency ω (top plot) and the growth rate γ (bottom plot) of LHDI as a function of k_y obtained from the GeFi simulation, in which $L = 0.23\rho_{i0}$, $\beta_{e0} = 0.0033$, $B_G/B_{x0} = 0.1$, $\omega_{pe}/\omega_e = 10$, and $n_b = 0.5$. The growth rate of the instability is seen to peak at $k_y\rho_{i0} \simeq 35$. As a comparison, the dashed lines in Fig. 3 show the analytical dispersion relation obtained from the GeFi eigenmode theory[62]. It is seen that both the real frequencies and the growth rate obtained from the GeFi simulation are nearly identical to those from the GeFi theory. The peak growth rates from the two models are also nearly identical.

The GeFi simulation results are also compared with the FK simulation results. Comparison of the LHDI dispersion relations between the two simulation schemes are shown in Fig. 4 for parameters similar to those in case 1. In this figure, the triangles depict ω and γ obtained from the GeFi scheme, and the circles show the corresponding values from the FK simulation. The dashed lines in Fig. 4 link through the values of the GeFi results. Results from the two particle simulation schemes are seen to agree very well.

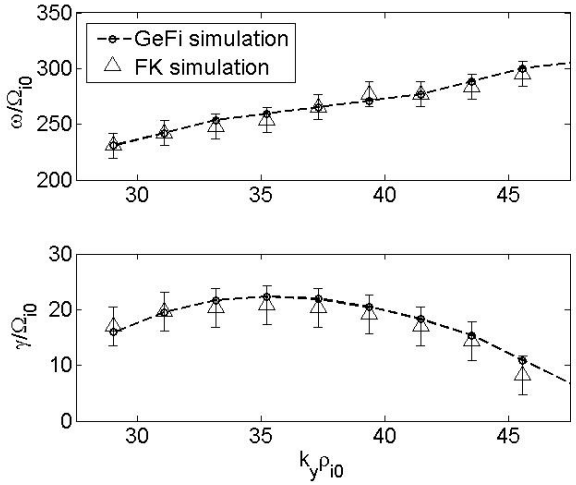

Figure 3.4: Comparison of the frequency and growth rate between the GeFi (circle-dashed line) and FK (open triangle) simulations for parameters similar to case 1. The top and bottom plots show the real frequency and the growth rate, respectively.

To understand the influence of the guide field B_G on the LHDI, Fig. 5 presents the frequency (top plot) and growth rate (bottom plot) vs. the intensity of guide field B_G/B_{x0} while the asymptotic field B_0 is fixed. The open circles present the GeFi simulation results, and the dashed lines show the results from the GeFi eigenmode theory. The simulation and the theory are seen to agree well. It is shown that as the guide field B_G increases, the frequency increases and the growth rate decreases. Such result can be understood as the following. As B_G increases under the fixed $B_0 = \sqrt{B_{x0}^2 + B_G^2}$, the B_{x0} component decreases. A smaller B_{x0} leads to a reduced diamagnetic current, which drives the unstable modes, and a smaller growth rate of LHDI.

3.3.2 Results with Finite k_x and k_y: Instabilities in 3-D

In this section, the GeFi simulation results are shown for the full 3-D space, with $k_x \neq 0$ and $k_y \neq 0$. The eigenmode structure, frequency, and growth rate are discussed as a function of (k_x, k_y). In the 3-D study, we focus on the cases with $k_y > k_x$ because the $k_y < k_x$ regime possesses no electrostatic instability.

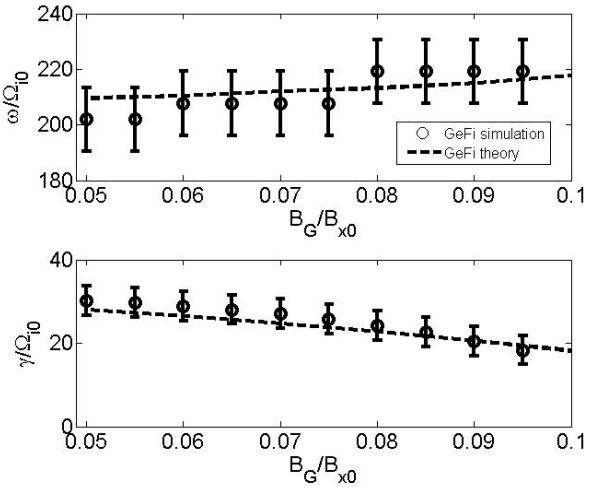

Figure 3.5: Frequency and growth rate vs. B_G/B_{x0}, for $L = 0.25\rho_{i0}$, $\beta_{e0} = 0.016$, $\omega_{pe}/\Omega_{ce} = 1.0$, $k_y\rho_{i0} = 35.23$.

3-D Eigenmodes

Fig. 6 shows the real space contours of $\delta\phi$ obtained from the GeFi simulation of case 2, in which $|k_y\rho_{i0}| = 29.02$, $|k_x\rho_{i0}| = 2.9$, and all other parameters are the same as case 1. The contours are shown for planes $y = -0.17\rho_{i0}$, and $x = -3\rho_{i0}$, 0, and $3\rho_{i0}$. It is found that the 3-D LHDI is excited and still localized at the edges of the current sheet. The phase of the instability changes with positions x and y, according to $\delta\phi = \delta\phi(z)\exp(k_x x + k_y y)$. The phase is related to the mode propagation in the x and y directions, which is discussed below.

In the 3-D space, for each sign of k_x, the LHDI occurs on only one side of current sheet. The absolute value of eigenfunction, $|\delta\tilde{\phi}|$, of case 2 is presented in Fig. 7. The red line in Fig. 7 shows the eigenfunction with $(k_x, k_y)\rho_{i0} = (-2.9, 29.02)$. The blue line shows the eigenfunction with $(k_x, k_y)\rho_{i0} = (2.9, 29.02)$. The dashed lines mark, again, $z = \pm L$, $\pm 2L$, and $\pm 3L$. For $k_x k_y > 0$ ($k_x k_y < 0$), the eigenmode is present on the $z = -L$ ($z = L$) side. This result is due to that in the presence of a finite k_x, the values of $\vec{k} \cdot \vec{B}$ are different on different sides of the current sheet, where $\vec{k} \cdot \vec{B} = k_x B_{x0}\tanh(z/L) + k_y B_y$. In case 2, the unstable mode is peaked at $\vec{k} \cdot \vec{B} \sim 0$. For $k_x k_y > 0$, the unstable mode appears on the $z < 0$ side since $\vec{k} \cdot \vec{B} = 0$ is present on this side. Finite $\vec{k} \cdot \vec{B}$ is found to stabilize the

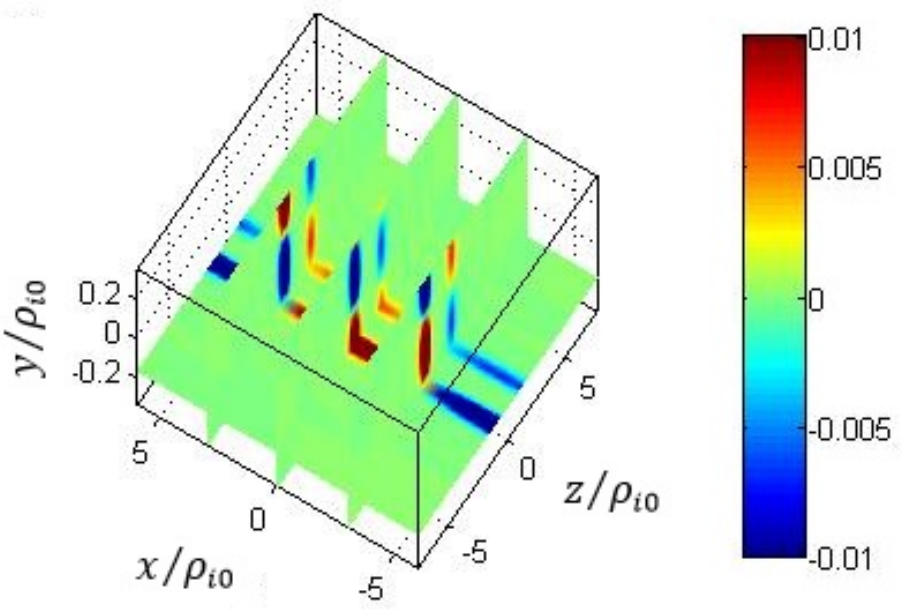

Figure 3.6: $\delta\phi$ contours in the x-z and y-z cross-sections in the 3-D simulation of case 2.

local stability. In the nonuniform magnetic field $\vec{B}(z)$, properties of the local instability at various z varies with $\vec{k} \cdot \vec{B}(z)$. For example, at the peak of the eigenfunction ($z = -1.4L$), $(k_x, k_y)\rho_{i0} = (2.9, 29.02)$ gives $\vec{k} \cdot \vec{B} \simeq 0$. On the opposite side of the current sheet at $z = 1.4L$, the same (k_x, k_y) gives $\vec{k} \cdot \vec{B} = 5.8$ and no unstable growth. Instead, the LHDI mode with $(k_x, k_y)\rho_{i0} = (-2.9, 29.02)$ peaks at $z = 1.4L$.

The phase speed of unstable modes depends on z, k_x, and k_y. It is shown that the LHDI propagates along the same $+y$-direction on both sides of current sheet, but in opposite

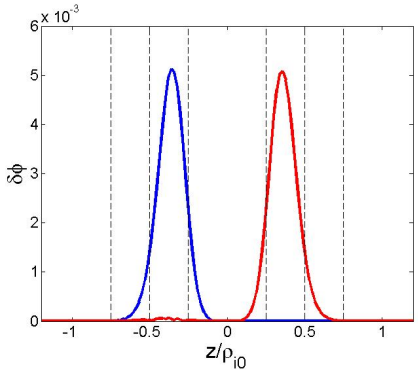

Figure 3.7: Eigenmode structure of the 3-D LHDI: the red and blue lines show eigenfunctions for ($k_x\rho_{i0} = -2.9$, $k_y\rho_{i0} = 29.02$) and ($k_x\rho_{i0} = 2.9$, $k_y\rho_{i0} = 29.02$), respectively.

directions along x. Consider the real frequency $\omega > 0$. For $(k_x, k_y)\rho_{i0} = (-2.9, -29.02)$,the phase velocity is $\mathbf{v}_{xph} = -67.6 v_{thi}\hat{\mathbf{x}}$ in the x-direction and $\mathbf{v}_{yph} = 6.8 v_{thi}\hat{\mathbf{y}}$ in the y-direction on the $z < 0$ side, where v_{thi} is the ion thermal velocity. On the $z > 0$ side, the sign of the unstable k_x is reversed to positive, with $\mathbf{v}_{xph} = 67.6 v_{thi}\hat{\mathbf{x}}$ and $\mathbf{v}_{yph} = 6.8 v_{thi}\hat{\mathbf{y}}$. The corresponding frequency is found to be $\omega/\Omega_{i0} = 196.1$ on both sides of current sheet.

Growth Rate in the k_x-k_y Space

In this subsection, we examine the growth rate of LHDI as a function of both k_x and k_y. Dependence of the results on the mass ratio m_i/m_e, half-width of current sheet L and guide field B_G are investigated.

Fig. 8 shows contours of the growth rate γ obtained from the GeFi simulation in the k_x-k_y space for $L/\rho_{i0} = 0.25$, $T_e/T_i = 0.1$, $B_G/B_{x0} = 0.1$, $n_{b0} = 0$ and $\omega_{pe}/\Omega_{ce} = 1.0$. As in the previous cases, a realistic proton-to-electron mass ratio $m_i/m_e = 1836$ is assumed. The black dashed line in Fig. 8 marks $\mathbf{k}\cdot\mathbf{B} = 0$ at the edge of the current sheet where the LHDI is present. As the contours showing, the maximal growth rate in the k_x-k_y plane is found to be $\gamma_{max}/\Omega_{i0} = 30.1$, present at $\mathbf{k}\cdot\mathbf{B} = 0$, with $(k_x, k_y)\rho_{i0} = (-2.9, 29.0)$. This peak LHDI growth rate corresponds to $0.7\omega_{LH}$, where $\omega_{LH} \equiv \sqrt{\Omega_{i0}\Omega_{e0}}$. The total wave number perpendicular to the nonuniformity direction, $k \equiv (k_x^2 + k_y^2)^{1/2}$, of this peak growth rate corresponds to $k\sqrt{\rho_i\rho_e} \simeq 2.5$. No instability is present for $k_y\rho_i < 8.4$. At the threshold $k_y\rho_i = 8.4$, the unstable $k_x\rho_i = -1.2$. As the wave number k_y increases, the unstable region becomes wider in k_x and is almost symmetric about $mathbfk \cdot \mathbf{B} = 0$. When the wave number k_y increases to a point around $k_y\rho_{i0} > 35$, however, there appears no instability at $\mathbf{k}\cdot\mathbf{B} = 0$. Rather, the unstable region splits into two separate ones in k_x for a certain k_y, located on the two sides and away from the $\mathbf{k}\cdot\mathbf{B} = 0$ line. Overall, the simulation reveals that the unstable mode is peaked at $\mathbf{k}\cdot\mathbf{B} = 0$ when the wave number is relatively small, whereas if the wave number is large enough the instability is peaked at $\mathbf{k}\cdot\mathbf{B} \neq 0$. The most unstable mode with the maximal growth rate in the k_x-k_y space, however, still satisfies $\mathbf{k}\cdot\mathbf{B} = 0$.

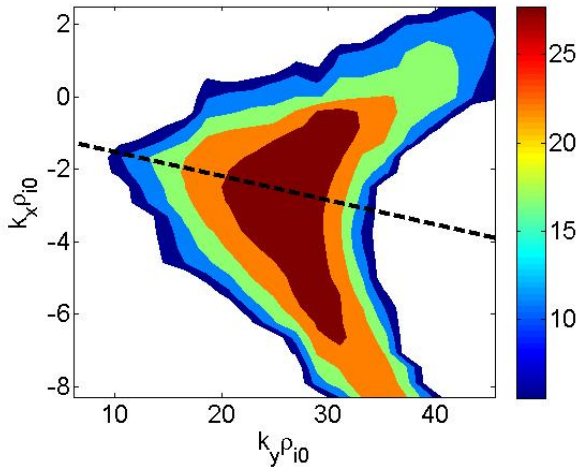

Figure 3.8: Contours of growth rate γ in the k_x-k_y space for $L/\rho_{i0} = 0.25$, $T_e/T_i = 0.1$, $B_G/B_{x0} = 0.1$, $n_{b0} = 0.0$, $m_i/m_e = 1836$, and $\omega_{pe}/\Omega_{ce} = 1.0$. The dark dashed line marks $\mathbf{k} \cdot \mathbf{B} = 0$. Colorbar shows growth rates.

The real space structure for the cases around the peaks at $\mathbf{k} \cdot \mathbf{B} \neq 0$ is qualitatively similar to those around $\mathbf{k} \cdot \mathbf{B} = 0$ (case 2). The contour plot obtained from the GeFi simulation is consistent with the prediction from the GeFi eigenmode theory[62].

Most FK simulations have been carried out with an artificial mass ratio in order to save the computing time. Therefore it is interesting to examine the mass ratio effect on the instability. To show the influence of the mass ratio on LHDI, Fig. 9 presents the GeFi simulation results with the realistic mass ratio, shown in column (a), and a reduced mass ratio $m_i/m_e = 1836/4 = 459$, shown in columns (b)and (c). All other parameters except the current sheet half-width L are the same as those for Fig. 8. When the mass ratio is varied, we also examine the results with a fixed L/ρ_e or L/ρ_i. In column (b) of Fig. 9, L/ρ_{i0} is fixed ($L = 0.25\rho_{i0} = 16.88\rho_{e0}$) as compared with column (a), whereas in column (c), L/ρ_{e0} is fixed ($L = 0.5\rho_{i0} = 33.75\rho_{e0}$) as the mass ratio is reduced. In addition, to understand the scaling of the LHDI physics, we present the results with two different normalizations, normalization to the ion cyclotron scales and the lower-hybrid scales. The top row of Fig. 9 shows the results with the wave number scaled to ρ_{i0}^{-1} and growth rate scaled to Ω_{i0}, whereas the bottom row plots the results scaled to $1/\sqrt{\rho_{i0}\rho_{e0}}$ and ω_{LH}, where $\omega_{LH} \equiv \sqrt{\Omega_{i0}\Omega_{e0}}$.

Compared to the contours shown in Fig. 9 (a) for the realistic $m_i/m_e = 1836$, the unstable range in k_y around the peak at $\mathbf{k} \cdot \mathbf{B} = 0$ becomes smaller for the smaller $m_i/m_e = 459$ and fixed L/ρ_{i0} when the results are normalized to the ion cyclotron scales, as seen in the top row of Fig. 9(b): the LHDI occurs in $6 < k_y\rho_{i0} < 14$ and $-9 < k_x\rho_{i0} < 4$ for $m_i/m_e = 459$, whereas it is present in $10 < k_y\rho_{i0} < 33$ and $-9 < k_x\rho_{i0} < 1$ for $m_i/m_e = 1836$. The unstable k_y range of the 'wing' regions, in which the modes satisfy $\mathbf{k} \cdot \mathbf{B} \neq 0$, is slightly smaller for the smaller mass ratio. The maximum growth rate in the k_x-k_y space for $m_i/m_e = 459$ ($\gamma/\Omega_{i0} \simeq 12$) is much smaller than that for the realistic mass ratio ($\gamma/\Omega_{i0} \simeq 30$).

When For the reduced mass ratio, when L/ρ_{e0} is fixed as $L = 33.75\rho_{e0}$, which corresponds to an L/ρ_{i0} two times that of Fig. 9(b), the peak growth rate is nearly the same as that in the run of Fig. 9(b) (top row) when the results are expressed with the ion cyclotron scales, i.e., much smaller than the growth rate under the realistic m_i/m_e. The k_x range of the instability is narrower by a significant 40% ($-10 < k_x\rho_{i0} < 5$ for $L = 0.25\rho_{i0}$ and $-7 < k_x\rho_{i0} < 2$ for $L = 0.5\rho_{i0}$) for the larger sheet width L/ρ_{i0}, while the k_y range of the instability is slightly larger ($6 < k_y\rho_{i0} < 21$ for $L = 0.25\rho_{i0}$ and $7 < k_y\rho_{i0} < 29$ for $L = 0.5\rho_{i0}$). Comparing the top rows of Figs. 9(b) and 9(c), which are for the same mass ratio, the simulation suggests that the wider current sheet stabilizes the LHDI, as the corresponding current and thus driving force become smaller.

Therefore, with respect to the ion ρ_i^{-1} and Ω_i, a smaller mass ratio leads to a smaller range of LHDI in the k_x-k_y space and/or a reduced growth rate. Furthermore, with the smaller mass ratio, the LHDI shifts to the smaller $k_y\rho_{i0}$ region. A wider current sheet also results in a smaller range of LHDI in the k_x-k_y space, stabilizing the LHDI.

On the other hand, if the results are scaled to the lower hybrid frequency ω_{LH}, the maximal growth rate of LHDI remains nearly the same for different values of mass ratio, as seen from the bottom rows of Fig. 9. Moreover, the maximal growth rate is the same for either a fixed L/ρ_{i0} or a fixed L/ρ_{e0} when m_i/m_e decreases. Meanwhile, when scaled to

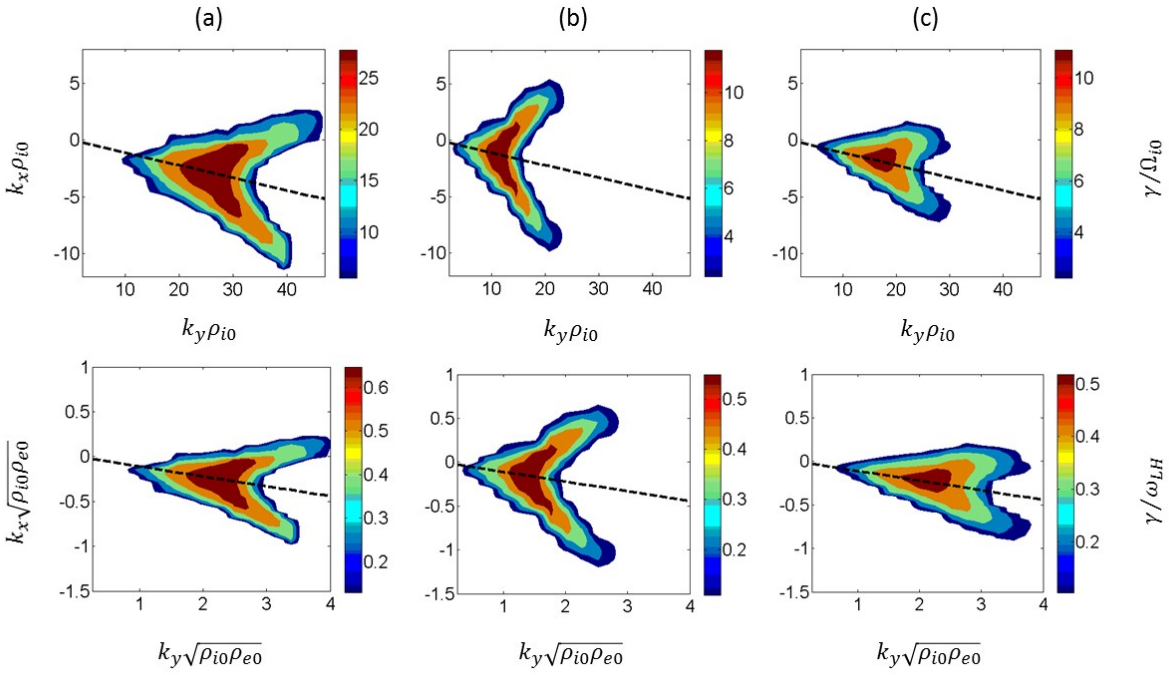

Figure 3.9: Contour plots of growth rate γ in the k_x-k_y space with (a) realistic mass ratio $m_i/m_e = 1836$ and $L = 0.25\rho_{i0} = 33.75\rho_{e0}$, (b) $m_i/m_e = 1836/4 = 459$ and $L = 0.25\rho_{i0} = 16.88\rho_{e0}$, and (c) $m_i/m_e = 1836/4 = 459$ and $L = 0.5\rho_{i0} = 33.75\rho_{e0}$. Top row shows the results with the wave number scaled to ρ_{i0}^{-1} and growth rate scaled to Ω_{i0}, and the bottom row shows the results scaled to $1/\sqrt{\rho_{i0}\rho_{e0}}$ and ω_{LH}. The black dashed line marks $\mathbf{k}\cdot\mathbf{B} = 0$.

$1/\sqrt{\rho_{i0}\rho_{e0}}$, the sizes of the unstable region in k_y are also similar for different values of mass ratio and under the two different widths L. The maximal growth rate $\gamma_{max}/\omega_{LH} \simeq 0.5$-$0.6$, and it occurs at $k\sqrt{\rho_i\rho_e} \simeq 2.0$-$3.0$. This result indicates that indeed the instability is scaled with the lower hybrid characteristics. Comparing the top and bottom rows of Figs. 9(a) and 9(c), it is also seen that for a certain mass ratio, the shape of the unstable region in the k_x-k_y space remains similar regardless of the scaling to $1/\sqrt{\rho_{i0}\rho_{e0}}$ or ρ_{i0}.

The guide field B_G plays an important role in the LHDI. To illustrate the influence of the guide field, Fig. 10 depicts the growth rate as a function of k_x and k_y for cases with a larger guide field, $B_G/B_{x0} = 0.3$. All other parameters are the same as those for Fig. 8 with the smaller $B_G/B_{x0} = 0.1$. The mass ratio is chosen as $m_i/m_e = 1836$ for both B_G. As described above, in the calculation we change B_G while fixing the total B_0 as a constant.

Comparing Figs. 8 and 10, it is seen that the k_y range of the 'wing' regions of LHDI is significantly reduced under the larger guide field. The range of k_y for the LHDI peaked at $\vec{k} \cdot \vec{B} = 0$ is also narrower under the larger B_G ($17 < k_y\rho_{i0} < 32$ for $B_G/B_{x0} = 0.3$ and $10 < k_y\rho_{i0} < 35$ for $B_G/B_{x0} = 0.1$). In addition, as B_G is increased to 0.3, the minimum k_y of the unstable region moves to a larger $k_y\rho_{i0}$. Correspondingly, the minimum k_x also shifts to a larger absolute value because of $\mathbf{k} \cdot \mathbf{B} = 0$ at the point. The growth rate of the most unstable mode also decreases under a larger B_G ($\gamma/\Omega_{i0} = 22.5$ for $B_G/B_{x0} = 0.3$ and $\gamma/\Omega_{i0} = 30.1$ for $B_G/B_{x0} = 0.1$). The 3-D simulations reveal that the guide field has a stabilizing effect on the LHDI, similar to the 2-D cases.

Simulations of the increased $B_G = 0.3$ are also performed with a fixed anti-parallel field $B_{x0} = 1.0$, and the results show a similar tendency that the LHDI is stabilized by the larger B_G. The LHDI is driven by the diamagnetic current associated with ∇P, or the drift velocity

$$v_{\nabla P} = -\nabla P \times \mathbf{B}_0/qB_0^2. \tag{3.14}$$

Here, P is the plasma thermal pressure, whose gradient is related to B_{x0} according to the pressure balance eq. (8). When the total B_0 is fixed, B_{x0} decreases as B_G increases, and thus ∇P decreases. When B_{x0} is fixed, the total B_0 increases as B_G increases. As a consequence, in both situations $v_{\nabla P}$ decreases. Hence, with either B_0 or B_{x0} fixed, increasing B_G reduces the driving force of LHDI and thus stabilizes the instability.

3.4 Summary

In this chapter, the electrostatic LHDI in a Harris current sheet is studied systematically by using the 3-D GeFi δf particle simulation model in the electrostatic limit for cases with a finite guide field B_G, with sheet normal in the z direction and guide field in the y direction. The LHDI is investigated for various (k_x, k_y). Effects of mass ratio m_i/m_e, guide field B_G, and half-width L of the current sheet are studied. The GeFi particle simulation results

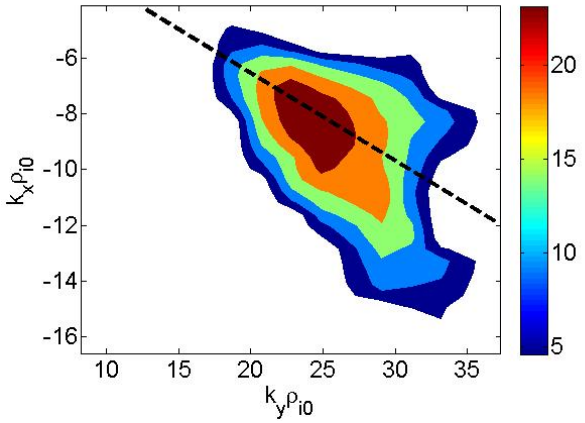

Figure 3.10: Contours of growth rate in the k_x-k_y space with guide field $B_G/B_{x0} = 0.3$, for $m_i/m_e = 1836$, $L/\rho_{i0} = 0.25$, $T_e/T_i = 0.1$, $n_{b0} = 0$ and ω_{pe}/Ω_{ce}=1.0.

are compared with the GeFi eigenmode theory and the FK particle simulations. The main results are summarized below.

1. Modes of the lower hybrid drift instability, localized at the edges of current sheet ($1 < |z/L| < 2$), propagate oppositely along the anti-parallel magnetic field direction (x) on the two sides of current sheet. Their propagation velocity in y is the same, along the ion drift direction.

2. The eigenmode structure is calculated as a function of k_x and k_y. In the limiting 2-D cases with k_x=0, two independent eigenmodes are present, with one on each side of the current sheet.

3. Introduction of a finite k_x significantly affects the eigenmode of LHDI. Unlike the 2-D results, the 3-D unstable mode only appears on one side of current sheet for a certain (k_x, k_y), the side where $\mathbf{k} \cdot \mathbf{B}$ is closer to zero.

4. The growth rates are calculated in the k_x-k_y space. The simulation results show that under a certain k_y, the dominant unstable mode satisfies $\mathbf{k} \cdot \mathbf{B} = 0$ when the wave number k_y is relatively small. As the wave number becomes larger, the dominant unstable mode can peak at $\mathbf{k} \cdot \mathbf{B} \neq 0$, although the most unstable mode in the entire k_x-k_y plane still satisfies $\mathbf{k} \cdot \mathbf{B} = 0$.

5. The simulation also demonstrates the dependence of LHDI on the mass ratio m_i/m_e and corresponding current sheet half-width L. Specifically, reducing mass ratio and increasing current sheet width have stabilizing effects on the LHDI. The growth rate γ and unstable regions in the k_x-k_y space depend on the normalization in the description of γ and k. The instability is found to be scaled with the lower hybrid characteristic length $1/\sqrt{\rho_{i0}\rho_{e0}}$ and frequency ω_{LH} when m_i/m_e and L vary. Meanwhile, increasing guide field stabilizes the LHDI.

6. The real space and eigenmode structures of LHDI obtained from the GeFi simulation agree very well with those from the FK δf simulations. The dispersion relation obtained from the GeFi simulation agrees very well with those obtained from the analytic theory and the FK simulation.

Chapter 4

Electromagnetic Results

In this chapter, the eigenmode stability properties of 3-D EM instabilities in a Harris current sheet with a finite guide magnetic field are systematically studied by employing the EM GeFi model with a realistic m_i/m_e. Our studies indicate that, at the small guide magnetic field B_G. the LHDI exists at $k\sqrt{\rho_i\rho_e} \sim 1$. The properties of LHDI are similar to those obtained in the ES simulations. The results from the GeFi code are compared with those from the electromagnetic FK particle code. On the other hand, DKI and drift sausage instability (DSI) are found to be present under a moderate B_G. The most unstable DKI is away from $\mathbf{k}\cdot\mathbf{B} = 0$ and the DSI peaks at $\mathbf{k}\cdot\mathbf{B} = 0$. Finally, Buneman instability (BI) with a compressional magnetic field perturbation is present at the center of current sheet under a relatively large B_G, with $k\rho_i \sim 10$. The most unstable BI is found at $\mathbf{k}\times\mathbf{B} = 0$.

4.1 Introduction

In the fully electromagnetic description, more typed of instabilities can be present in the current sheet, in addition to the LHDI. These EM-dominant instabilities include the tearing mode and drift-kink instability, as discussed in the introduction chapter. In the EM regime, previous studies found that the instabilities can exist in both short wavelength regime ($k\sqrt{\rho_i\rho_e} \sim 1$) and long wavelength regime ($k\rho_i \sim 1$). The LHDI is the dominant unstable mode for $k\sqrt{\rho_i\rho_e} \sim 1$. As found in the electrostatic simulationsin Chapter III, the most unstable LHDI is peaked at $\mathbf{k}\cdot\mathbf{B} \neq 0$ at certain k_y and the instability is scaled with the lower hybrid characteristic length $1/\sqrt{\rho_{i0}\rho_{e0}}$ and frequency ω_{LH} when m_i/m_e and L vary. Previous electromagnetic FK PIC simulations of LHDI was carried out in a rotated plane

that contains $\mathbf{k} \cdot \mathbf{B} = 0$[64]. In this chapter, the linear properties of LHDI are calculated with the fully EM GeFi code systematically in the full 3-D space.

While LHDI was extensively studied by previous authors, the instabilities at $k\sqrt{\rho_i} \sim 1$ are still poorly understood. Previous FK simulations and theoretical results showed the existence of drift-kink instability ([74, 70]. Meanwhile, Wang et al.[84] found an unstable EM mode peaked at $k\rho_i \sim 1$, which was named as 'mode B'. This mode has a compressional magnetic fluctuation at the center of current sheet. The DKI was found under a zero guide magnetic field, whereas the mode B was found under a small but finite guide field. The guide field, therefore, was found to influence the current sheet instabilities at $k\rho_i \sim 1$ as well. In this chapter, we investigate the EM instabilities in a broad range of $k\rho_i$, under intermediate broad range of the guide fields.

4.2 Lower-Hybrid Drift Instability under Small Guide Field

In the following, we show the simulation results of current sheet instability under a small guide field $B_G/B_{x0} = 0.1$ ==. It is found that under this small B_G, only LHDI is present. Cases of 2-D LHDI with $k_x = 0$ and $k_y \neq 0$ are presented first. The full 3-D results with $k_x \neq 0$ and $k_y \neq 0$ are then presented. Because the EM GeFi code has not been benchmarked in the lower-hybrid frequency range for an inhomogeneous plasma, the results of the GeFi code are also compared with those of the FK code.

2-D Properties of Stability

Fig. 4.1 shows the results of case 1, with the same parameters as those in case 1 of Chapter 3 for the ES limit, in which $L = 0.25\rho_{i0}$, $\beta_{e0} = 0.016$, $B_G/B_{x0} = 0.1$, $\omega_{pe}/\Omega_{ce} = 1.0$, and the background plasma density is set to be zero, i.e., $n_{b0} = 0$. Similar to Fig. 3.1, nly modes with $k_y\rho_{i0} = \pm 26.1$ are kept. The top column of Fig. 4.1 presents the GeFi simulation results, while the bottom column shows the corresponding FK simulation results. The left, middle and right columns show the contours of the perturbed magnetic field δB_z, δB_x and

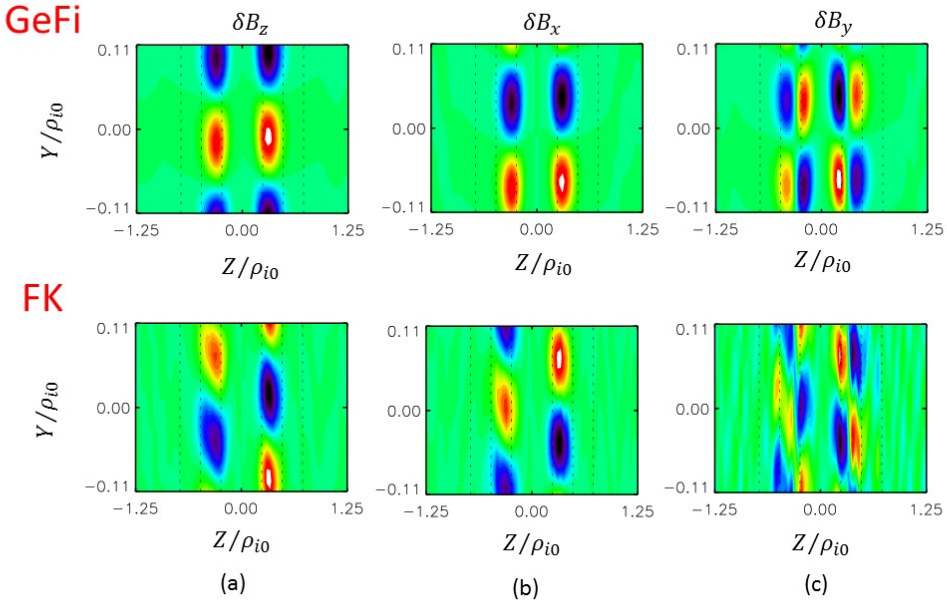

Figure 4.1: FK and GeFi simulation results for case 1, with $L/\rho_{i0} = 0.25$, $T_e/T_i = 0.1$, $\beta_{e0} = 0.016$, $n_{b0} = 0.0$, $B_G/B_{x0} = 0.1$, $\omega_{pe}/\Omega_{ce} = 1.0$ and $k_y\rho_{i0} = 26.1$. (a) Contours of δB_z from the GeFi (top) and FK (bottom) models. (b) Contours of δB_x from the GeFi (top) and FK (bottom) models. (c) Contours of δB_y from the GeFi (top) and FK (bottom) models. The dashed lines mark $z = \pm L$, $\pm 2L$, and $\pm 3L$.

δB_y in the y-z plane, respectively. The dashed lines in Fig. 4.1 mark the positions $z = \pm L$, $\pm 2L$, and $\pm 3L$. Instability in the magnetic field perturbation is excited, which is found to be located at the edge of the current sheet, within $L < |z| < 2L$, similar to the ES results in Fig. 3.1. The compressional component δB_y shows two anti-symmetric peaks, whereas B_x and B_z show one peak.

Figs. 4.2 (a), (b) and (c) show the absolute values of the eigenfunctions of δB_z, δB_x, and δB_y respectively. Again, the compressional field δB_y shows two peaks. Fig. 4.2(d) shows $|\delta B_z|$ of the instability as a function of time. An exponential growth is seen, with a linear growth rate of $\gamma/\Omega_{i0} = 20.5$ obtained in the GeFi simulation and $\gamma/\Omega_{i0} = 18.7$ from the FK simulation. The results from the GeFi simulation are in excellent agreement with those from the FK simulation in terms of the linear growth rate and mode structure. As expected,

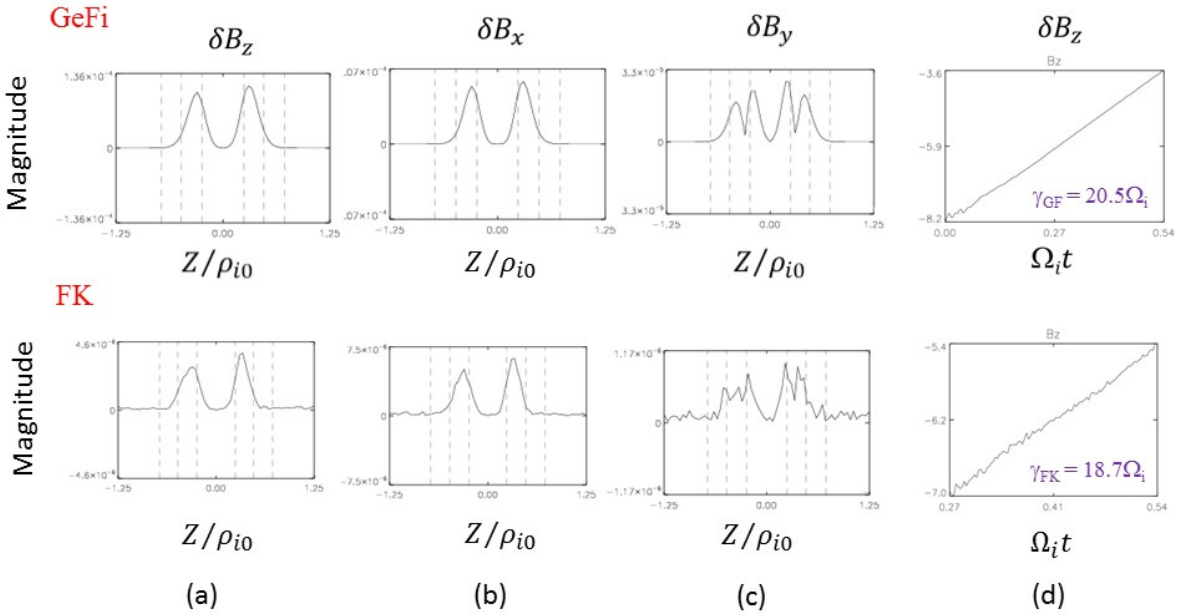

Figure 4.2: Eigenmodes of the FK and GeFi simulations for case 1, with $L/\rho_{i0} = 0.25$, $T_e/T_i = 0.1$, $\beta_{e0} = 0.016$, $n_{b0} = 0.0$, $B_G/B_{x0} = 0.1$, $\omega_{pe}/\Omega_{ce} = 1.0$ and $k_y\rho_{i0} = 26.1$. In (a),(b),and (c), the solid lines present the absolute value of eigenfunctions obtained from the GeFi (top) and FK (bottom) simulations. The dashed lines mark $z = \pm L$, $\pm 2L$, and $\pm 3L$. (d) The growth rates of eigenmodes obtained from the GeFi (left) and FK (right) simulations.

higher frequency fluctuations are also present in the growth curve of the FK results, while the growth curve obtained from the GeFi model is much smoother due to the removal of fluctuations with $\omega \sim \Omega_e$. The LHDI propagates in the $+y$ direction, i.e., direction of the ion drift, at both edges of the current sheet. Moreover, as shown in Figs. 4.2(a), 4.2(b) and 4.2(c), there is little $\delta\mathbf{B}$ near the center of the current sheet. The two eigenmodes on the two sides of the current sheet are independent.

Fig. 4.3 shows the vector potential $\delta\mathbf{A}$ and the scalar potential $\delta\phi$. For the scalar potential $\delta\phi$ and each component of $\mathbf{A}$, the instability is localized at $z = L$, . A_y shows two

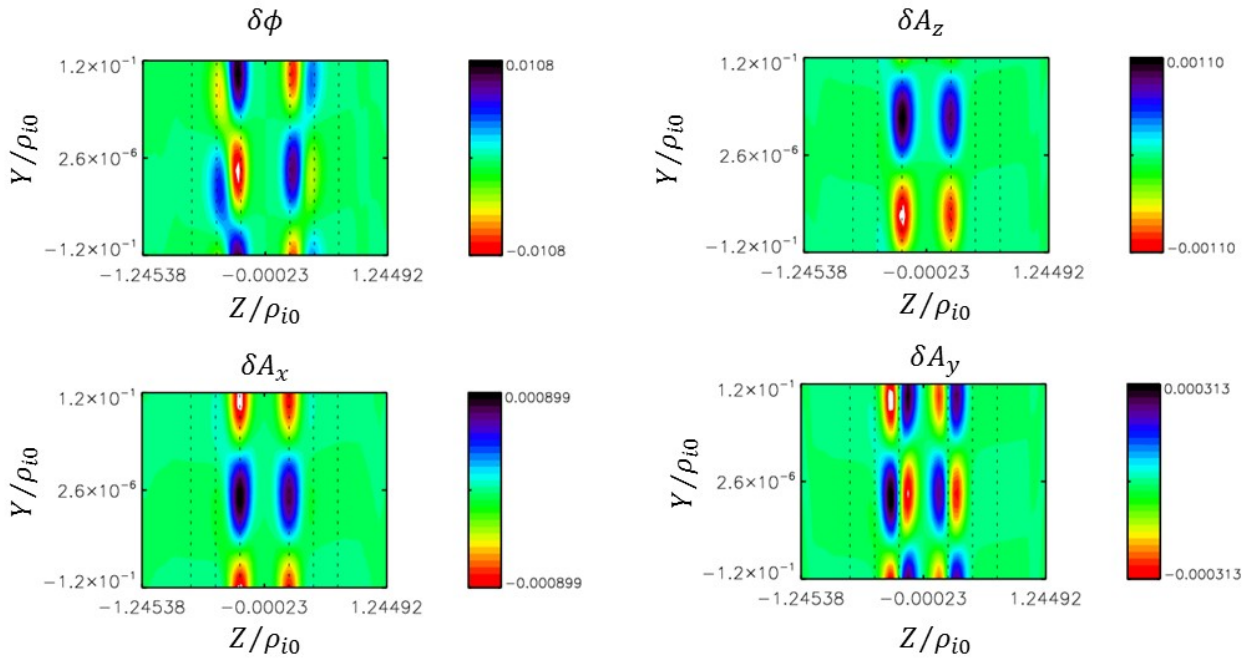

Figure 4.3: **A**-ϕ eigenmodes for case 1. The dashed lines mark $z = \pm L$, $\pm 2L$, an $\pm 3L$.

anti-symmetric peaks at $z = L$, similar to δB_y. The magnitude of $\delta\phi$ ($\sim 10^{-2}$) is an order of magnitude higher than δA_z and δA_x ($\sim 10^{-3}$) and is two orders higher than $\delta\phi$ ($\sim 10^{-4}$). Therefore, as expected, the LHDI is a quasi-electrostatic mode even in the EM calculation.

To further illustrate the ES nature of the LHDI, the absolute values of $\nabla \times \mathbf{E}$ and $\nabla \cdot \mathbf{E}$ are plotted in Fig. 4.4. Overall, the ratio $\nabla \times \mathbf{E}/\nabla \cdot \mathbf{E}$ is found to be $\sim 10^{-1}$. The longitudinal mode $\nabla \cdot \mathbf{E}$, in which the electromagnetic component is eliminated under the Coulomb gauge, is much larger than the transverse mode $\nabla \times \mathbf{E}$, in which the electrostatic component is eliminated. Therefore, the comparison between $\nabla \times \mathbf{E}$ and $\nabla \cdot \mathbf{E}$ confirms that the LHDI is a quasi-electrostatic mode.

The triangles with error bars in Fig. 4.5 show the real frequency ω (top plot) and the open circles show the growth rate γ (bottom plot) of LHDI as a function of k_y obtained from

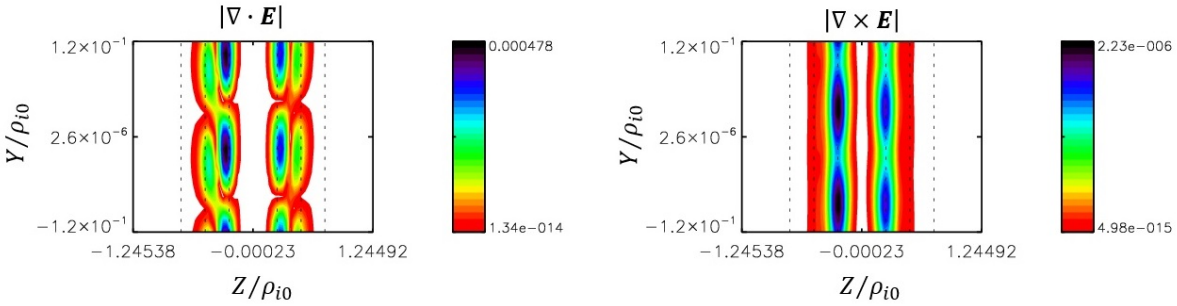

Figure 4.4: $\nabla \cdot \mathbf{E}$ and $\nabla \times \mathbf{E}$. The dashed lines mark $z = \pm L$, $\pm 2L$, an $\pm 3L$.

the GeFi simulation, in which $L = 0.23\rho_{i0}$, $\beta_{e0} = 0.0033$, $B_G/B_{x0} = 0.1$, $\omega_{pe}/\omega_e = 10$, and $n_b = 0.5$. The growth rate of the instability is seen to peak at $k_y\rho_{i0} \simeq 70$. As a comparison, the dashed lines in Fig. 3 show the analytical dispersion relation obtained from the GeFi theory[135]. It is seen that both the real frequencies and the growth rate obtained from the GeFi simulation are nearly identical to those from the GeFi theory. The peak growth rates from the two models are also nearly identical.

4.2.1 3-D Properties of Stability

We now show 3-D simulations of the LHDI for a case with a finite $|k_x\rho_{i0}| = 1.2$, for $|k_y\rho_{i0}| = 20.7$ and all other parameters the same as case 1. Figs. 4.6, 4.7, and 4.8 show the real space contours of δB_x, δB_y, and δB_z, respectively, obtained from the GeFi simulation of case 2 for planes $y = 0.137\rho_{i0}$, and $x = -2\rho_{i0}$, $x = 2\rho_{i0}$, and $6\rho_{i0}$. It is found that the 3-D LHDI is excited and still localized at the edges of the current sheet. The phase of the instability changes with positions x and y, according to $\delta B_z = \delta B_z(z)\exp(k_x x + k_y y)$. The phase speed of unstable modes depends on k_x and k_y, and the direction of phase velocity depends on z. It is shown, again, that the LHDI propagates along the same $+y$-direction on both sides of current sheet, but in opposite directions along x. Consider the real frequency $\omega > 0$. For $(k_x, k_y)\rho_{i0} = (-1.2, -20.7)$,the phase velocity is $\mathbf{v}_{xph} = -134.6v_{thi}\hat{\mathbf{x}}$ in the x-direction and $\mathbf{v}_{yph} = 7.8v_{thi}\hat{\mathbf{y}}$ in the y-direction on the $z < 0$ side, where v_{thi} is the ion thermal velocity. On the $z > 0$ side, the sign of the unstable k_x is reversed to positive,

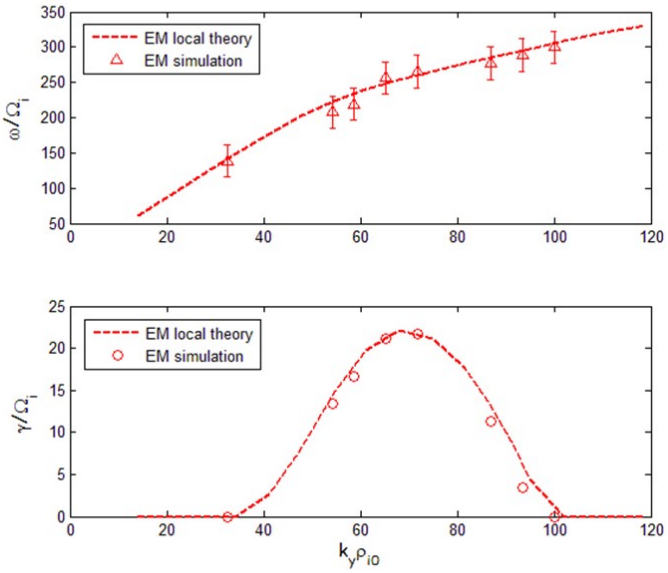

Figure 4.5: Comparison of the frequency (top plot) and growth rate (bottom plot) between the GeFi simulation (triangles) and the GeFi theory (dashed lines) for $L = 0.23\rho_{i0}$, $\beta_{e0} = 0.0033$, $B_G/B_{x0} = 0.1$, $\omega_{pe}/\Omega_{ce} = 10$, and $n_b = 0.5$.

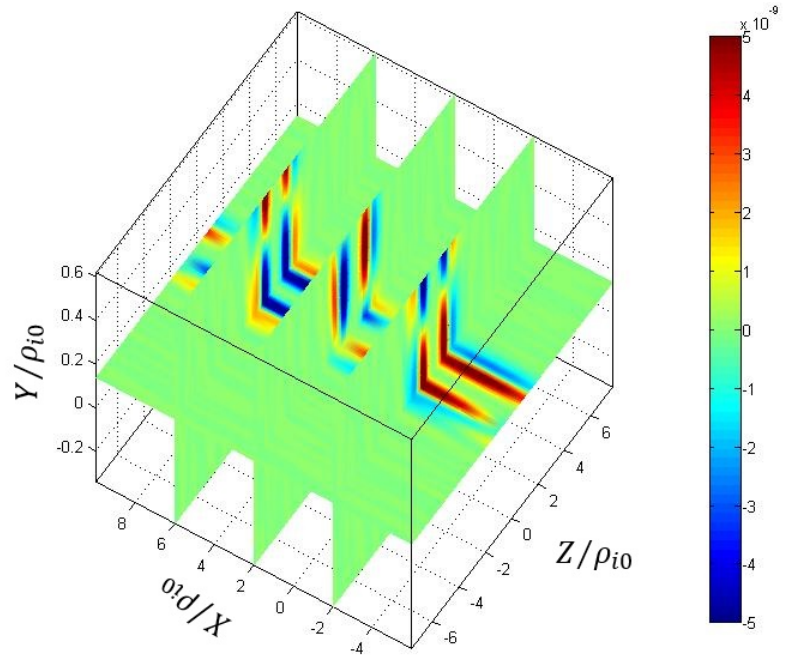

Figure 4.6: δB_z contours in the 3-D simulation of case 2 for planes $y = 0.137\rho_{i0}$ in the y-z cross-sections, and $x = -2\rho_{i0}$, $x = 2\rho_{i0}$, and $6\rho_{i0}$. Colorbar shows magnitudes of fields.

with $\mathbf{v}_{xph} = 134.6v_{thi}\hat{\mathbf{x}}$ and $\mathbf{v}_{yph} = 7.8v_{thi}\hat{\mathbf{y}}$. The corresponding frequency is found to be $\omega/\Omega_{i0} = 161.5$ on both sides of current sheet.

The eigenfunctions of $\delta\mathbf{A}$ and $\delta\phi$ of case 2 are presented in Fig. 4.9. The black solid and the red pointed lines are the real and imaginary parts of the eigenfunctions, respectively. The dashed black lines mark the positions $z = \pm L$, $\pm 2L$, and $\pm 3L$. Like the ES results of LHDI, the EM fluctuations in $\delta\mathbf{A}$ and $\delta\phi$ are localized at the edge of the current sheet ($L < |z| < 3L$), andthe magnitude is nearly zero at the center of current sheet. It is seen that the real and imaginary parts of the eigenfunctions on the both side of the current sheet are not identical, but the absolute value of the eigenfunctions are identical. The two unstable mode on the both sides are independent. Moreover, the magnitude of $\delta\phi$ ($\sim 10^{-5}$) is two order of magnitude higher than $\delta\mathbf{A}$ ($\sim 10^{-7}$).

Next, we examine the growth rate of LHDI as a function of both k_x and k_y and compare the results with the calculation in the ES limit. Fig. 4.10 shows contours of the growth

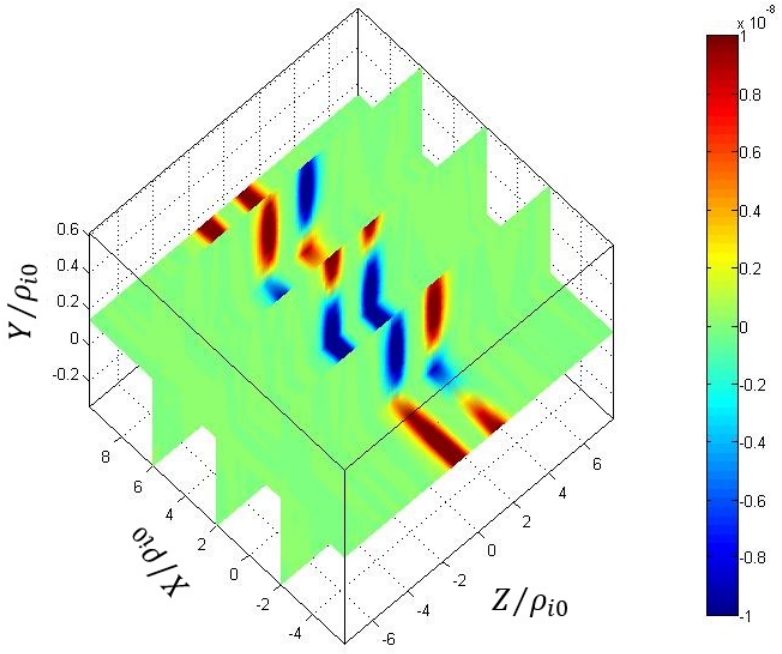

Figure 4.7: δB_x contours in the 3-D simulation of case 2 for planes $y = 0.137\rho_{i0}$ in the y-z cross-sections, and $x = -2\rho_{i0}$, $x = 2\rho_{i0}$, and $6\rho_{i0}$.

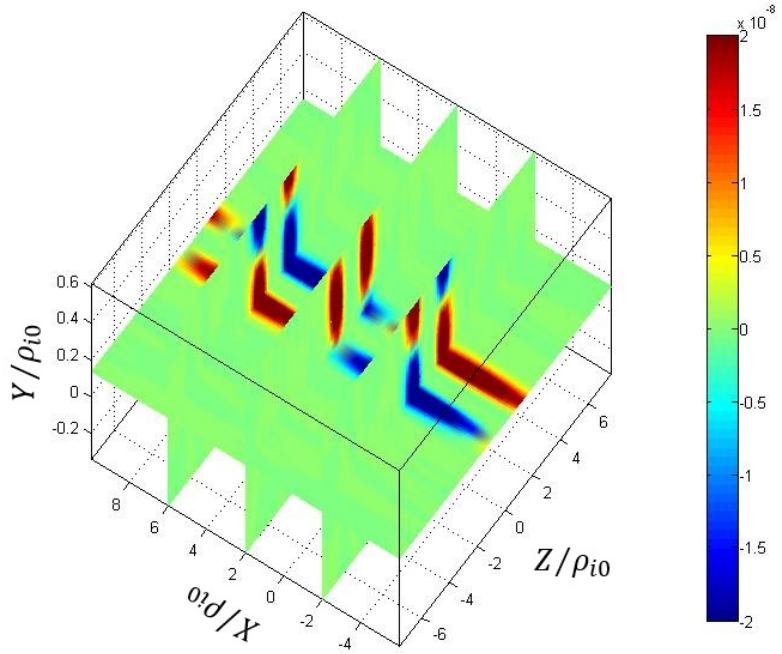

Figure 4.8: δB_y contours in the 3-D simulation of case 2 for planes $y = 0.137\rho_{i0}$ in the y-z cross-sections, and $x = -2\rho_{i0}$, $x = 2\rho_{i0}$, and $6\rho_{i0}$.

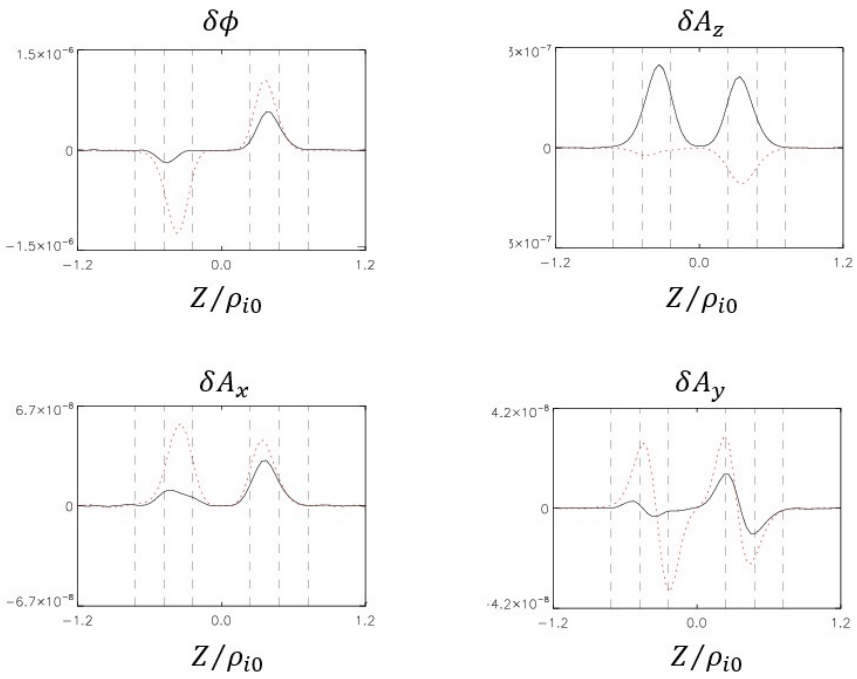

Figure 4.9: Eigenfunctions of case 2, with $L/\rho_{i0} = 0.25$, $T_e/T_i = 0.1$, $\beta_{e0} = 0.016$, $n_{b0} = 0.0$, $B_G/B_{x0} = 0.1$, $\omega_{pe}/\Omega_{ce} = 1.0$, $k_x\rho_{i0} = 1.2$ and $k_y\rho_{i0} = 20.7$. The black solid and the red pointed lines are the real and imaginary parts of the eigenfunctions respectively. The dashed black lines mark the position $z = \pm L$, $\pm 2L$, and $\pm 3L$.

rate γ obtained from the GeFi simulation in the k_x-k_y space for $L/\rho_{i0} = 0.25$, $T_e/T_i = 0.1$, $B_G/B_{x0} = 0.1$, $n_{b0} = 0$ and $\omega_{pe}/\Omega_{ce} = 1.0$, with a realistic proton-to-electron mass ratio $m_i/m_e = 1836$. The black dashed line in Fig. 4.22 marks $\mathbf{k}\cdot\mathbf{B} = 0$ at the edge of the current sheet where the LHDI is present. As the contours showing, the maximal growth rate in the k_x-k_y plane is found to be $\gamma_{max}/\Omega_{i0} = 17.1$, present at $\mathbf{k}\cdot\mathbf{B} = 0$, with $(k_x, k_y)\rho_{i0} = (-1.5, 15.0)$. This peak LHDI growth rate corresponds to $0.4\omega_{LH}$. The total wave number perpendicular to the nonuniformity directionof this peak growth rate corresponds to $k\sqrt{\rho_i\rho_e} \simeq 1.5$. At the threshold $k_y\rho_i = 2.6$, the unstable $k_x\rho_i = -0.15$. When the wave number k_y increases to a point around $k_y\rho_{i0} > 35$, the unstable region splits into two separate ones in k_x for a certain k_y, located on the two sides and away from the $\mathbf{k}\cdot\mathbf{B} = 0$ line. Similar to the ES results, the unstable mode is peaked at $\mathbf{k}\cdot\mathbf{B} = 0$ when the wave number is relatively small, whereas if the wave number is large enough the instability is peaked at $\mathbf{k}\cdot\mathbf{B} \neq 0$. The most unstable mode with the maximal growth rate in the k_x-k_y space, however, still satisfies $\mathbf{k}\cdot\mathbf{B} = 0$. Compared with the ES results shown in Fig. 3. 8, the maximum growth rate becomes smaller, and the unstable region in the k_x-k_y plane shifts to smaller k_y,

In addition, it is found that the stabilizing effects of B_G is more efficient in the fully EM calculation of LHDI. No LHDI is found when B_G/B_{x0} increases to 0.2 in the EM calculation, whereas in the ES calculation the LHDI is found even when $B_G/B_{x0} = 0.3$.

4.3 Drift Kink and Sausage Instability under Moderate Guide Field

Previously, Wang et al.[84] found that EM-dominant instabilities in the lower-hybrid frequency range and with $k\rho_i \sim 1$ exist in the 2-D plane which contains the current sheet normal and the current under a moderate guide field $B_G/B_{x0} = 0.2$. In this section, the 3-D instabilities under $B_G/B_{x0} = 0.2$ are studied with the 3-D GeFi code.

Fig. 4.11 shows the real space structure of $\delta\mathbf{A}$ and $\delta\phi$ in the y-z plane at $x = 0$ of case 3, in which $L = 0.25\rho_{i0}$, $\beta_{e0} = 0.016$, $B_G/B_{x0} = 0.2$, $\omega_{pe}/\Omega_{ce} = 1.0$, $n_{b0} = 0$. Only modes with $k_x\rho_{i0} = \pm 0.2$ and $k_y\rho_{i0} = \pm 1.2$ are kept. The dashed lines mark the positions

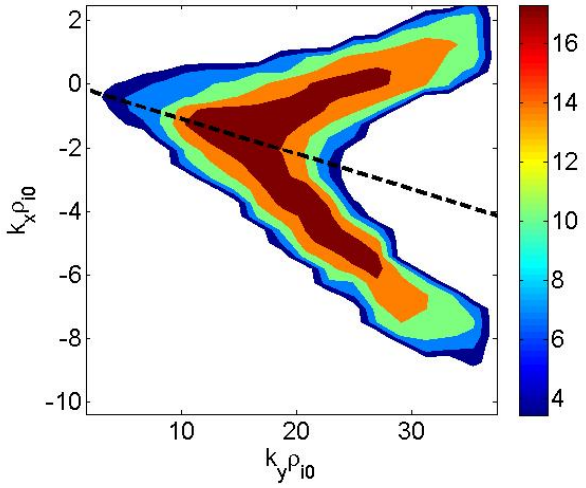

Figure 4.10: Contours of growth rate γ of LHDI in the k_x-k_y space for $L/\rho_{i0} = 0.25$, $T_e/T_i = 0.1$, $B_G/B_{x0} = 0.1$, $n_{b0} = 0.0$, $m_i/m_e = 1836$, and $\omega_{pe}/\Omega_{ce} = 1.0$. The dark dashed line marks $\mathbf{k} \cdot \mathbf{B} = 0$. Colorbar shows growth rates.

$z = \pm L$, $\pm 2L$, and $\pm 3L$, and the color-bar indicates the magnitude of fields. An instability with fluctuation of $\delta\phi$, δA_x, and δA_y is found to localize at the edge of the current sheet ($L < |z| < 3L$), while δA_z occupies the current sheet ($0 < |z| < 3L$). $\delta\phi$ and δA_y have an odd mode structure, while δA_x and δA_z have an even mode structure. Unlike the LHDI, whose wave vector is parallel to the current sheet normal, the wave vector of the unstable mode is oblique to the current direction. The quantity $\delta\mathbf{B}$ in the y-z plane is shown in Fig 4.12, in which δB_x, δB_y and δB_z are seen to localize at the edge of the current sheet. All components of $\delta\mathbf{B}$ propagate in the direction oblique to $\hat{\mathbf{y}}$. The amplitude of δB_y is one order of magnitude larger than that of δB_x, and two orders of magnitude larger than that of δB_z. Fig. 4.13 shows the real space contours of δB_y in the x-z plane at $y = 4.7\rho_{i0}$, and in y-z planes at $x = 19.8\rho_{i0}$, $x = 44\rho_{i0}$, and $68\rho_{i0}$. The multiple planes in the figure show the instability is localized at the edge of current sheet.

The eigenfunctions of scalar potential $\delta\phi$ and vector potential $\delta\mathbf{A}$ of case 3 are shown in Fig. 4.13, where the black solid and red pointed lines are the real and imaginary parts, respectively, and the black dashed lines mark the positions $z = \pm L$, $\pm 2L$ and $\pm 3L$. $\delta\phi$ and δA_y are of an odd symmetry, whereas δA_x and δA_z are of an even symmetry. The magnitude

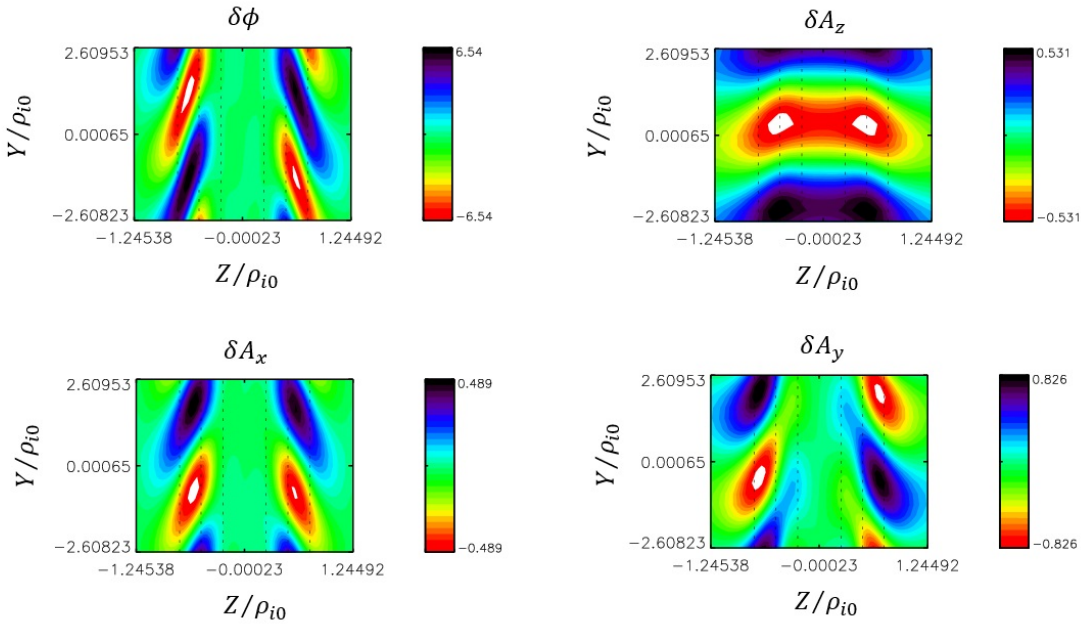

Figure 4.11: $\delta\phi$ and $\delta\mathbf{A}$ on the y-z plane of case 3 at $z = 0$, with $L/\rho_{i0} = 0.25$, $T_e/T_i = 0.1$, $\beta_{e0} = 0.016$, $n_{b0} = 0.0$, $B_G/B_{x0} = 0.1$, $\omega_{pe}/\Omega_{ce} = 1.0$, $k_x\rho_{i0} = 0.2$ and $k_y\rho_{i0} = 1.2$. The dashed black lines mark the position $z = \pm L$, $\pm 2L$, and $\pm 3L$. Colorbar shows magnitudes of fields.

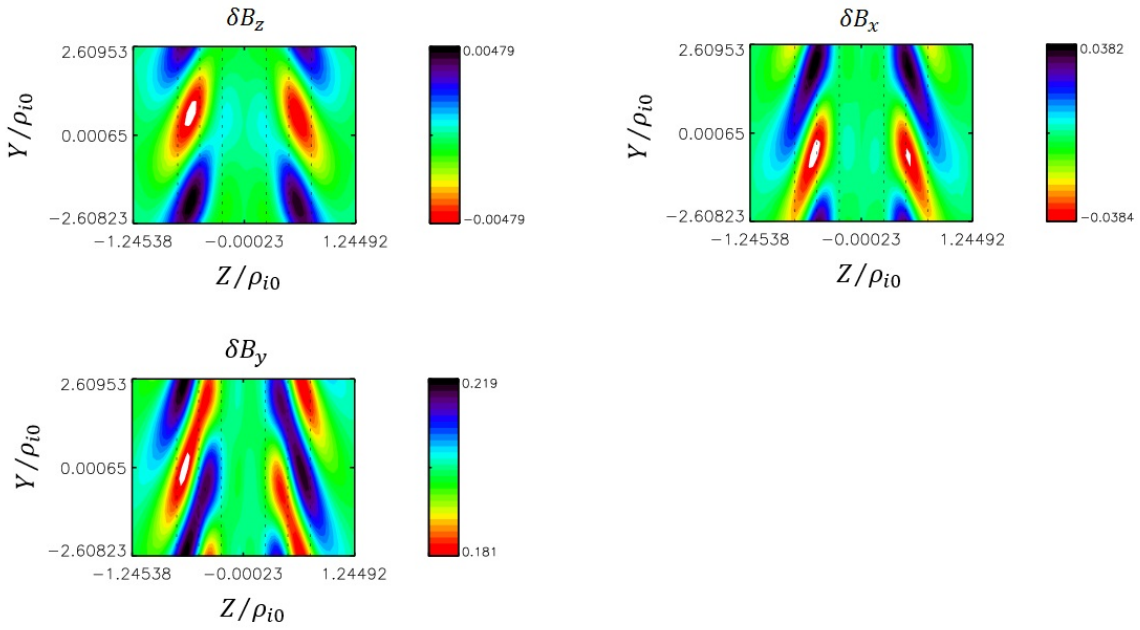

Figure 4.12: $\delta\mathbf{B}$ on the y-z plane of case 3 at $z = 0$. The dashed black lines mark the position $z = \pm L$, $\pm 2L$, and $\pm 3L$.

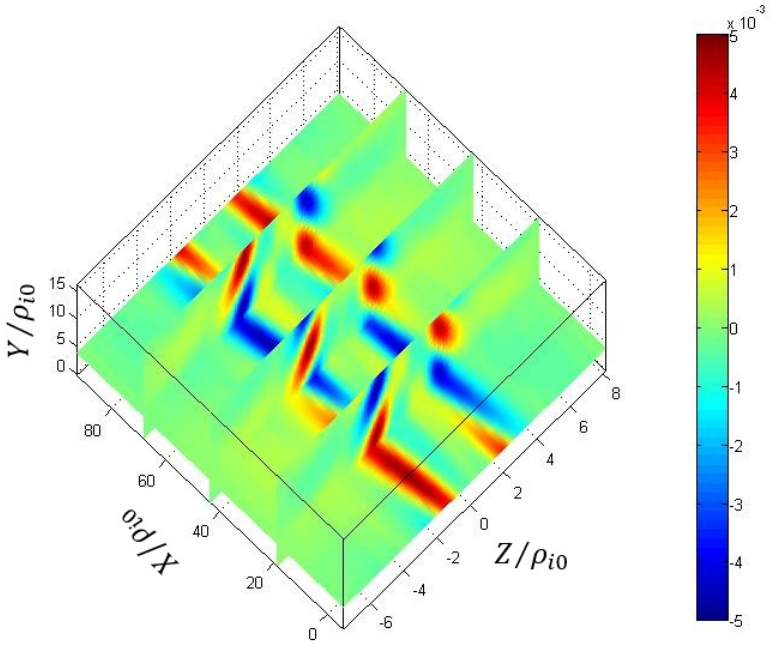

Figure 4.13: δB_y contours in the 3-D simulation of case 3 for planes $y = 4.7\rho_{i0}$ in the y-z cross-sections, and $x = 19.8\rho_{i0}$, $x = 44\rho_{i0}$, and $68\rho_{i0}$. Colorbar shows magnitudes of fields.

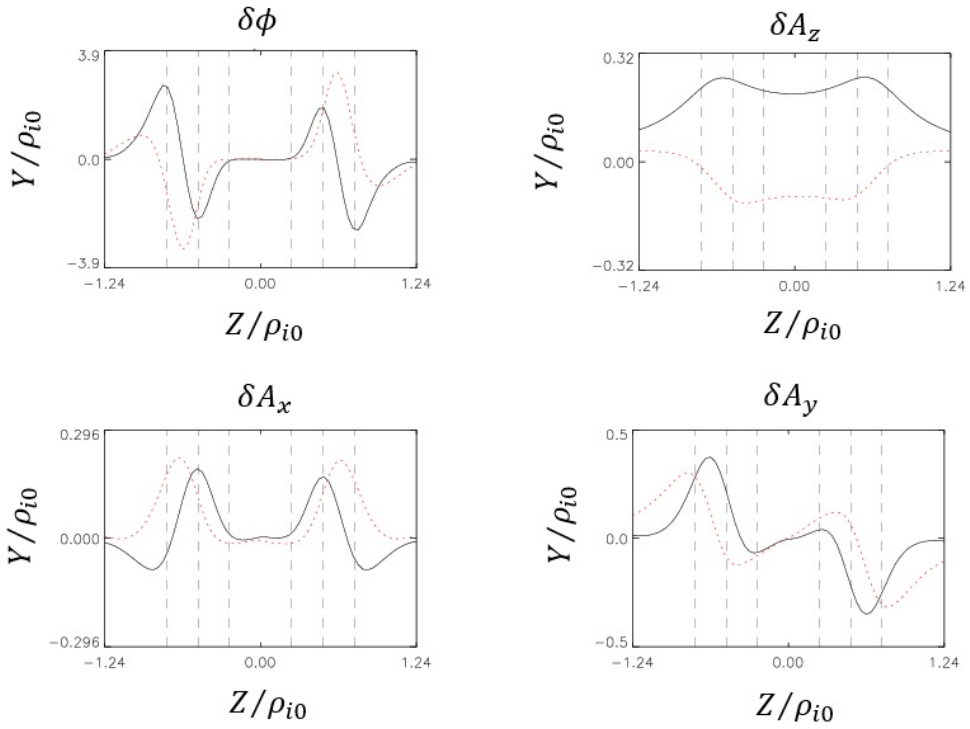

Figure 4.14: Eigenfunctions of $\delta\phi$ and $\delta\mathbf{A}$ of case 3, with $L/\rho_{i0} = 0.25$, $T_e/T_i = 0.1$, $\beta_{e0} = 0.016$, $n_{b0} = 0.0$, $B_G/B_{x0} = 0.1$, $\omega_{pe}/\Omega_{ce} = 1.0$, $k_x\rho_{i0} = 0.2$ and $k_y\rho_{i0} = 1.2$. The black solid and the red pointed lines are the real and imaginary parts of the eigenfunctions respectively. The dashed black lines mark the position $z = \pm L$, $\pm 2L$, and $\pm 3L$.

of $\delta\mathbf{A}$ and $\delta\phi$ are identical on both sides of the current sheet. At the center of the current sheet, the value of $\delta\phi$, δA_x, and δA_y are zero, while A_z has a finite magnitude. Therefore, unlike LHDI, the unstable mode on both sides of the current sheet are coupled.

The eigenfunctions of components of $\delta\mathbf{B}$ of case 3 are shown in Fig. 4.15. It is seen that δB_x and δB_z are an even mode, and δB_y is an odd mode. The magnitude of δB_x and δB_y are an order of magnitude larger than that of δB_z. The δB_y component shows the kink-like structure, in which the value of field at $z = 0$ is zero, similar to the drift kink mode in Daughton[63]. The frequency of the mode is in the lower-hybrid frequency range ($\omega/\Omega_{i0} = 60.6$ in case 3), and the imaginary part is several Ω_{i0} ($\gamma/\Omega_{i0} = 3.8$). Thus, the unstable mode is identified as the drift kink instability (DKI).

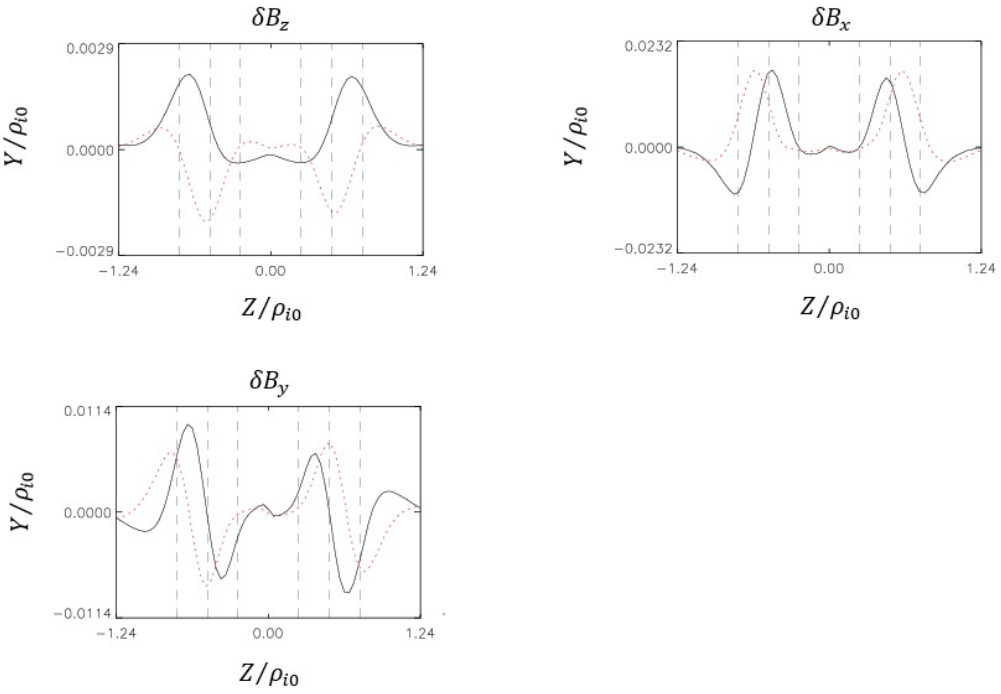

Figure 4.15: Eigenfunctions of $\delta\mathbf{B}$ of case 3, The black solid and the red pointed lines are the real and imaginary parts of the eigenfunctions respectively. The dashed black lines mark the position $z = \pm L$, $\pm 2L$, and $\pm 3L$.

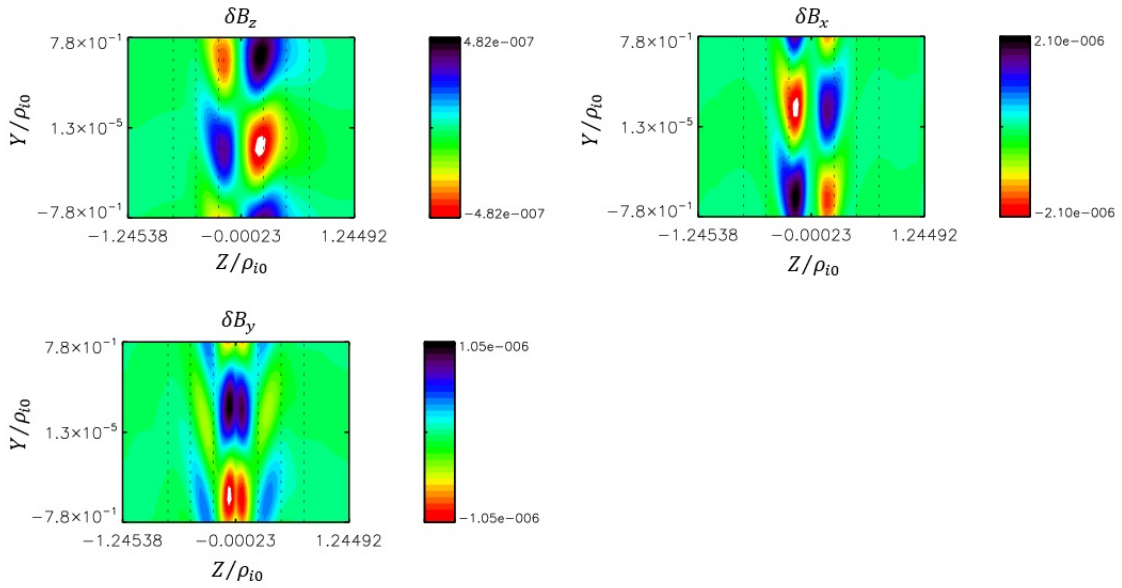

Figure 4.16: $\delta\mathbf{B}$ on the y-z plane of case 4 at $z = 0$, with $L/\rho_{i0} = 0.25$, $T_e/T_i = 0.1$, $\beta_{e0} = 0.016$, $n_{b0} = 0.0$, $B_G/B_{x0} = 0.1$, $\omega_{pe}/\Omega_{ce} = 1.0$, $k_x\rho_{i0} = 0.6$ and $k_y\rho_{i0} = 4.0$. The dashed black lines mark the position $z = \pm L$, $\pm 2L$, and $\pm 3L$, colorbar shows magnitudes of fields.

When the wave number k is increased, another instability is found to be excited. Fig. 4.16 shows the real space contours at $x = l_x/2 = 44\rho_{i0}$ of all components of $\delta\mathbf{B}$ of case 4, which has the same parameters as case 3 except for $k_x\rho_{i0} = \pm 0.6$ and $k_y\rho_{i0} = \pm 4.0$. The dashed lines mark the positions $z = \pm L$, $\pm 2L$, and $\pm 3L$. An instability is localized at the edge of the current sheet, with an odd mode structure in δB_x and δB_z. The instability propagates parallel to $\hat{\mathbf{y}}$. The component δB_y, also propagating along the $\hat{\mathbf{y}}$, has two peaks with an even symmetry and is located around the center of the current sheet. The amplitude of B_x and B_y are comparable and an order of magnitude higher than that of B_z. Fig. 4.17 shows the real space contours of δB_y in the x-z plane at $y = 4.7\rho_{i0}$, and in the y-z planes at $x = 19.8\rho_{i0}$, $x = 44\rho_{i0}$, and $68\rho_{i0}$, in the 3-D box.

The eigenfunctions of components of $\delta\mathbf{B}$ of case 4 are shown in Fig. 4.18, where the black solid and red dotted lines indicate the real and imaginary parts, respectively. The

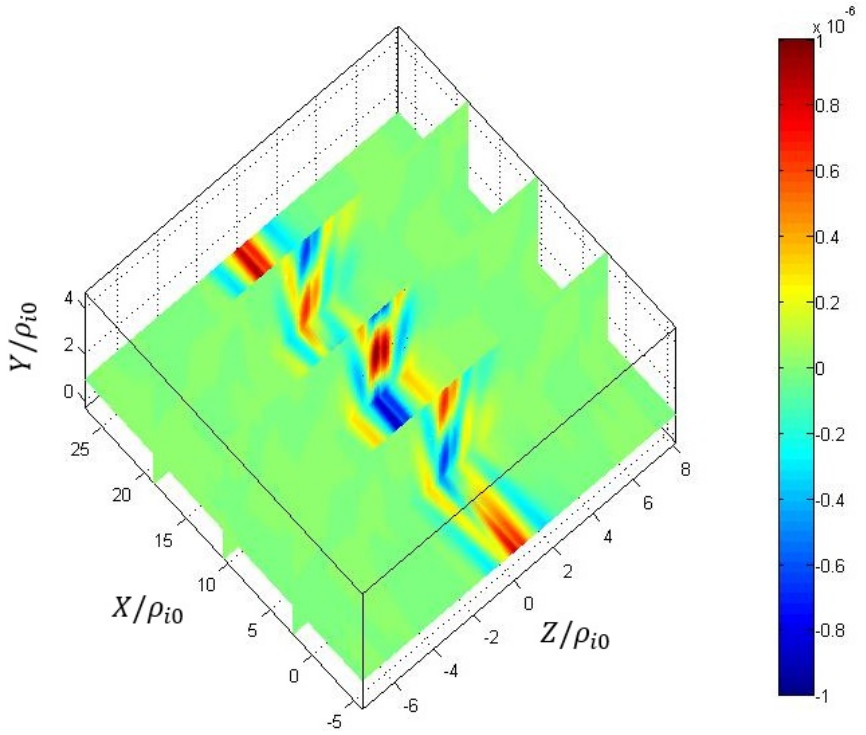

Figure 4.17: δB_y contours in the 3-D simulation of case 4 for planes $y = 4.7\rho_{i0}$ in the y-z cross-sections, and $x = 19.8\rho_{i0}$, $x = 44\rho_{i0}$, and $68\rho_{i0}$. Colorbar shows magnitudes of fields

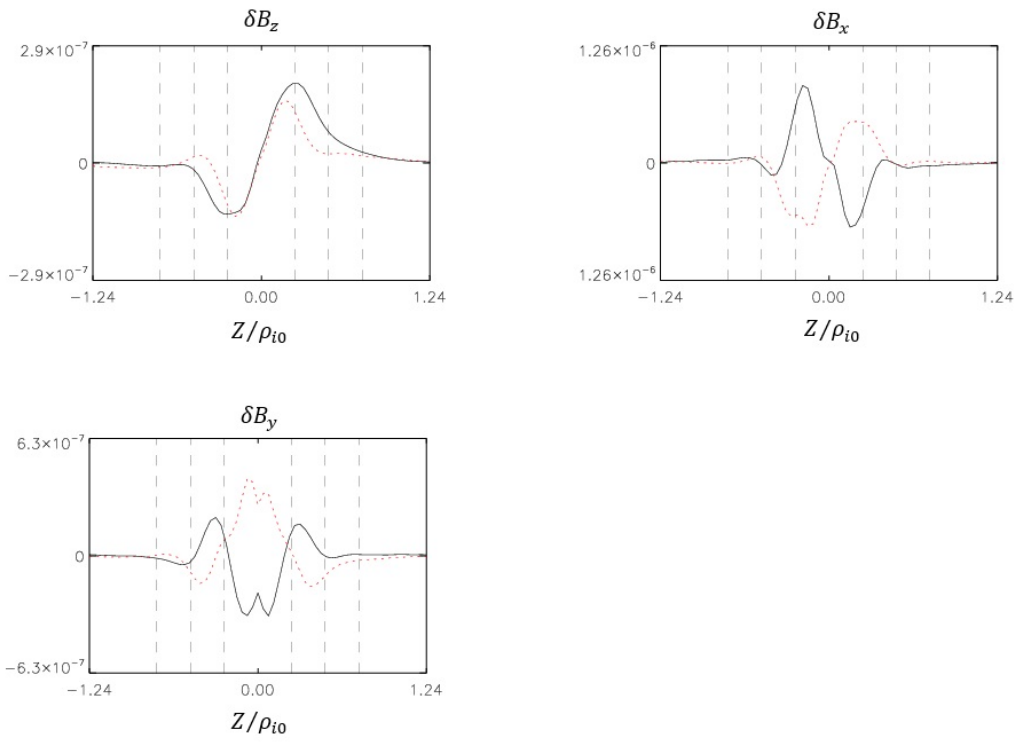

Figure 4.18: Eigenfunctions of $\delta\mathbf{B}$ of case 4, The black solid and the red pointed lines are the real and imaginary parts of the eigenfunctions respectively. The dashed black lines mark the position $z = \pm L$, $\pm 2L$, and $\pm 3L$.

black dashed lines mark the positions $z = \pm L$, $\pm 2L$, and $\pm 3L$. The quantities δB_x and δB_z have a kink-like structure (odd mode). The quantityδB_y, whose two peaks are located close to the center of the current sheet, has a sausage-like structure (even mode). The growth rate of the instability is $\gamma/\Omega_{i0} = 2.5$, larger than that of the tearing mode. Due to the sausage structure of δB_y and the lower-hybrid range frequency ($\omega/\Omega_{i0} = 28.8$), the instability is called the drift sausage instability (DSI).

The growth rates of the drift kink and sausage instabilities are calculated as a function of k_x and k_y, shown in Fig. 4.19. The unstable region is separated as two zones, A and B, as pointed by the two arrows. The black dashed line marks $\mathbf{k} \cdot \mathbf{B} = 0$. In zone A ($-2 < k_x\rho_{i0} < 1$, $0 < k_y\rho_{i0} < 4$), the DKI is dominant. The most unstable DKI is away from $\mathbf{k} \cdot \mathbf{B} = 0$. The DSI exists in zone B ($-3 < k_x\rho_{i0} < -1$, $4 < k_y\rho_{i0} < 8$) and is peaked

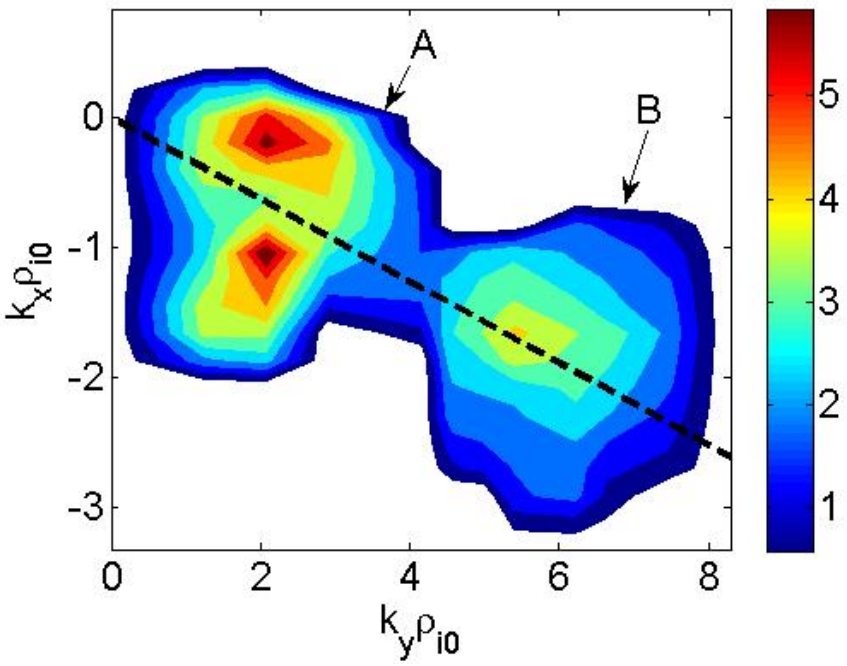

Figure 4.19: Contours of growth rate γ of DKI and DSI in the k_x-k_y space for $L/\rho_{i0} = 0.25$, $T_e/T_i = 0.1$, $B_G/B_{x0} = 0.2$, $n_{b0} = 0.0$, $m_i/m_e = 1836$, and $\omega_{pe}/\Omega_{ce} = 1.0$. The dark dashed line marks $\mathbf{k} \cdot \mathbf{B} = 0$. Colorbar shows the growth rates of DKI and DSI

at $\mathbf{k} \cdot \mathbf{B} = 0$. The growth rates of the DKI and DSI are comparable, with the growth rates of DKI being a little larger.

4.4 Instability under Large Guide Field

In this section, instabilities under a larger guide field, $B_G/B_{x0} = 0.6$, are searched in the 3-D current sheet system.

Fig. 4.20 shows all components of the perturbed magnetic field $\delta\mathbf{B}$ of case 5, in which $L = 0.25\rho_{i0}$, $\beta_{e0} = 0.016$, $B_G/B_{x0} = 0.6$, $\omega_{pe}/\Omega_{ce} = 1.0$, and $n_{b0} = 0$. Only modes with $k_x\rho_{i0} = \pm 0.6$ and $k_y\rho_{i0} = \pm 14.5$ are kept. The dashed lines in Fig. 4.13 mark the positions $z = \pm L$, $\pm 2L$, and $\pm 3L$. The primary peaks of δB_x and δB_z are of an odd mode and located at the central region of the current sheet, within $0.2L < |z| < L$. There also exist secondary peaks with a smaller magnitude, within $L < |z| < 2L$. The wave vectors of δB_x and δB_y are oblique to $\hat{\mathbf{y}}$ and pointing toward the current sheet center. The quantity δB_y, which is

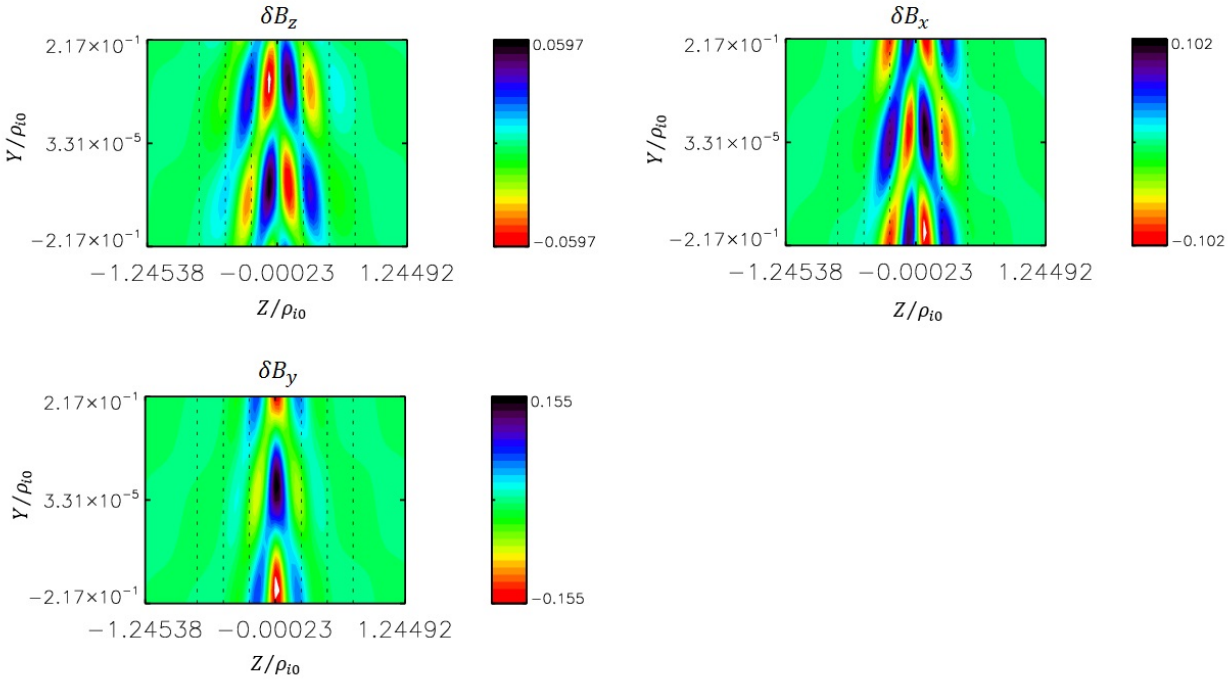

Figure 4.20: Mode structures of $\delta\mathbf{B}$ for case 4, with $L/\rho_{i0} = 0.25$, $T_e/T_i = 0.1$, $\beta_{e0} = 0.016$, $n_{b0} = 0.0$, $B_G/B_{x0} = 0.6$, $\omega_{pe}/\Omega_{ce} = 1.0$, $k_x\rho_{i0} = 0.6$ and $k_y\rho_{i0} = 14.5$. The dashed lines mark $z = \pm L$, $\pm 2L$, and $\pm 3L$. Colorbar shows magnitudes of fields

the compressional component of magnetic field, is an even mode and peaked at the center of current sheet.

The real space structure of $\delta\mathbf{A}$ and $\delta\phi$ are shown in Fig. 4.21. The scalar potential $\delta\phi$ is localized at the edge of the current sheet with the wave vector oblique to the y direction. The vector potentials δA_x and δA_z are an odd mode and have a kink-like structure. The primary peaks of these two components are located inside the current sheet ($|z| < L$), The secondary peaks are present at the edge of the current sheet ($L < |z| < 2L$). The component δA_y is an even mode and have a sausage-like structure, for which the primary peak is located exactly at the center of the current sheet while the secondary peak is at $0.2L < |z| < L$. The magnitude of $\delta\phi$ is an order of magnitude larger than that of $\delta\mathbf{A}$.

The eigenfunctions of $\delta\mathbf{B}$ of case 4 are shown in Fig 4.22, in which the black solid and red dotted lines indicate the real and imaginary parts of the eigenfunction. The black

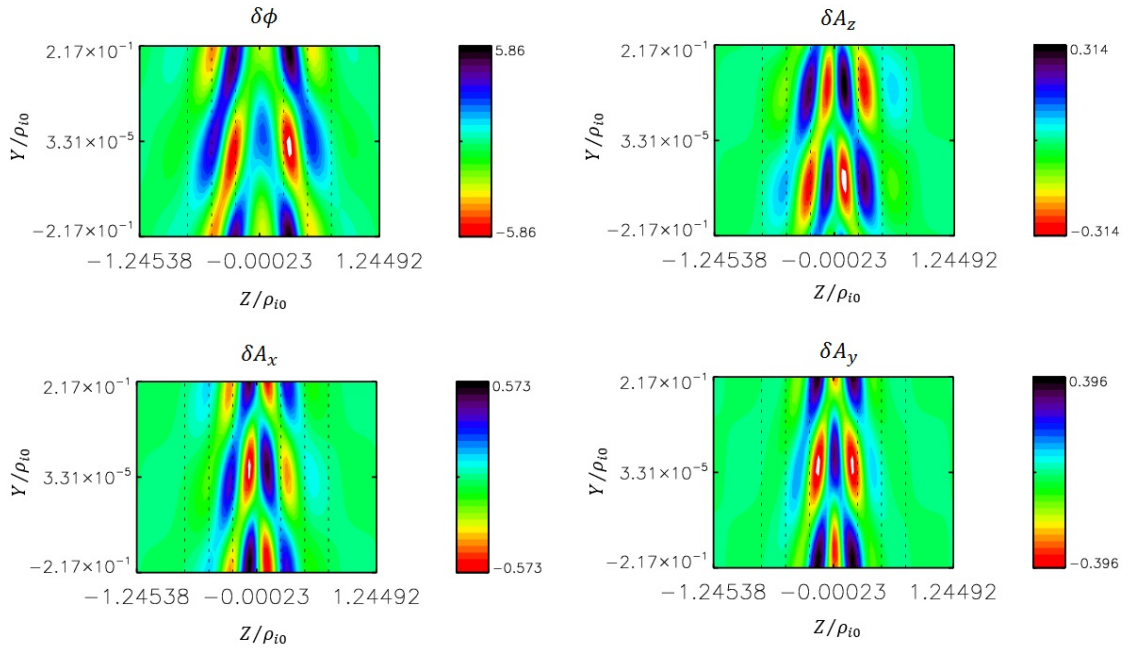

Figure 4.21: Mode structures of $\delta\mathbf{A}$ and $\delta\phi$ for case 4, with $L/\rho_{i0} = 0.25$, $T_e/T_i = 0.1$, $\beta_{e0} = 0.016$, $n_{b0} = 0.0$, $B_G/B_{x0} = 0.6$, $\omega_{pe}/\Omega_{ce} = 1.0$, $k_x\rho_{i0} = 0.6$ and $k_y\rho_{i0} = 14.5$. The dashed lines mark $z = \pm L$, $\pm 2L$, and $\pm 3L$.

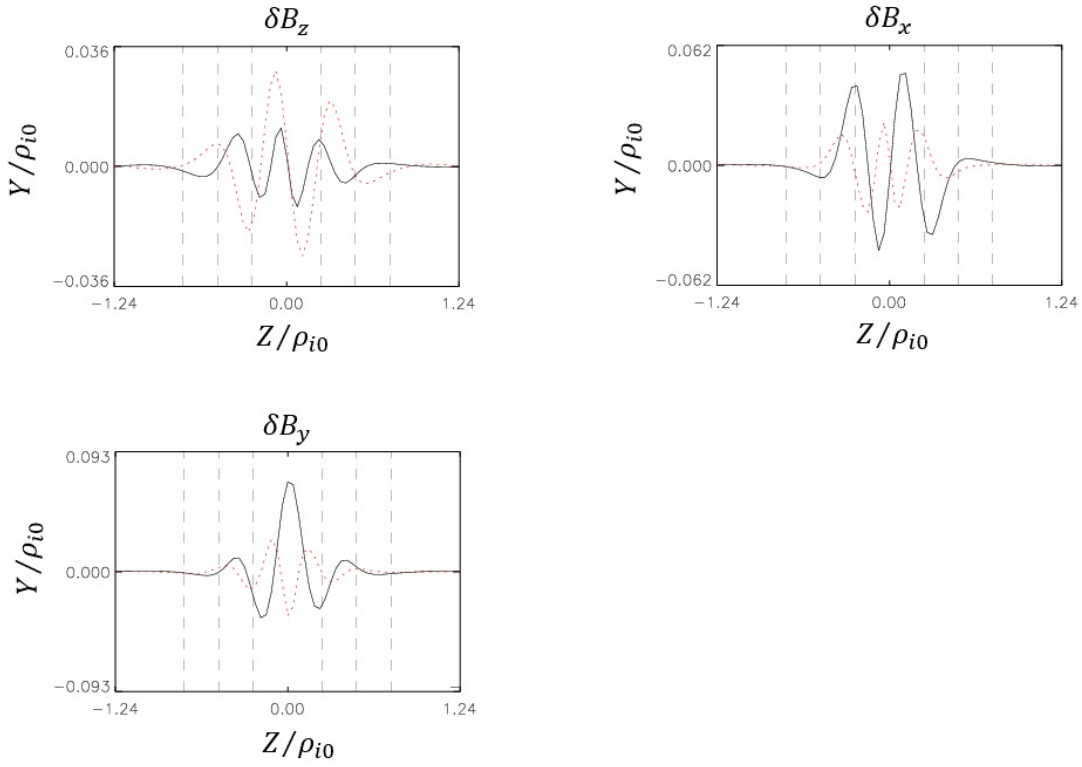

Figure 4.22: Eigenfunctions of $\delta\mathbf{B}$ case 4, with $L/\rho_{i0} = 0.25$, $T_e/T_i = 0.1$, $\beta_{e0} = 0.016$, $n_{b0} = 0.0$, $B_G/B_{x0} = 0.1$, $\omega_{pe}/\Omega_{ce} = 1.0$, $k_x\rho_{i0} = 0.6$ and $k_y\rho_{i0} = 14.5$. The black solid and the red pointed lines are the real and imaginary parts of the eigenfunctions respectively. The dashed black lines mark the position $z = \pm L$, $\pm 2L$, and $\pm 3L$.

dashed lines mark the positions $z = \pm L$, $\pm 2L$, and $\pm 3L$. It is seen that δB_z and δB_x are an odd mode and has a kink-like structure, while δB_y is an even mode and has a sausage-like structure. The magnitude of δB_x, δB_y, and δB_z are comparable.

Fig. 4.23 shows the real space contours of the compressional component, δB_y, for planes $y = 0$, and $x = 2.25\rho_{i0}$, $x = 10.5\rho_{i0}$, and $18.8\rho_{i0}$. The compressional magnetic fluctuation is seen to be located at the center of the current sheet.

Although the spatial structure of this unstable mode is similar to that of the DSI in case 4, the wave number ($k\sqrt{\rho_i\rho_e} \sim 1$) of the instability is much larger than that of the DSI ($k\rho_{i0} \sim 1$). The real frequency ($\omega/\Omega_{i0} = 226.9$) and the growth rate ($\gamma/\Omega_{i0} = 10.97$) of this

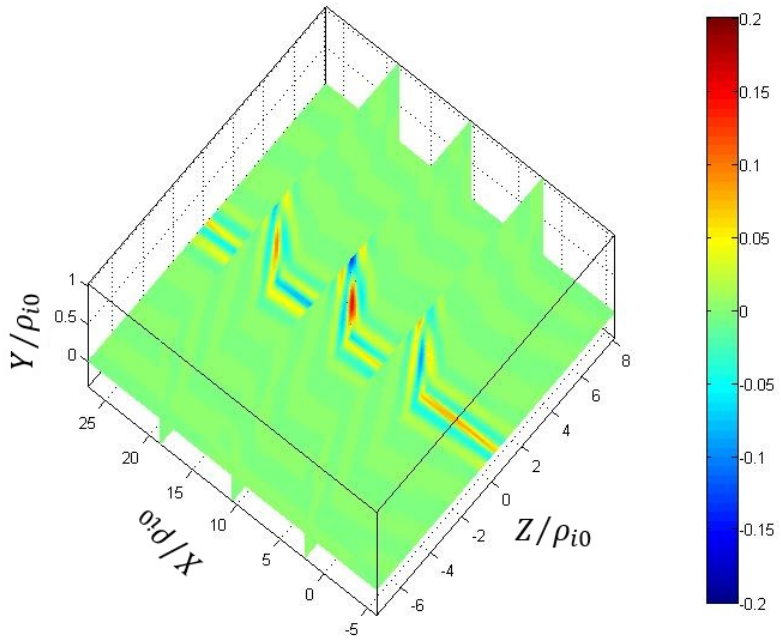

Figure 4.23: δB_z contours in the planes $y = 0$, and $x = 2.25\rho_{i0}$, $x = 10.5\rho_{i0}$, and $18.8\rho_{i0}$ of case 5. Colorbar shows magnitudes of fields

mode are an order of magnitude larger than those of the DSI. Moreover, the compressional magnetic fluctuation peaks exactly at the sheet center, which is also different from the structure of the DSI.

Finally, we examine the growth rate of this new mode as a function of both k_x and k_y. Fig. 4.24 shows contours of the growth rate γ obtained from the GeFi simulation in the k_x-k_y space for $L/\rho_{i0} = 0.25$, $T_e/T_i = 0.1$, $B_G/B_{x0} = 0.6$, $n_{b0} = 0$ and $\omega_{pe}/\Omega_{ce} = 1.0$, and a realistic $m_i/m_e = 1836$ is assumed. The black dashed line in the figure marks $(\mathbf{k}\times\mathbf{B}) = 0$ at$z = 0.6L$, where the peak of δA_x is present. As the contours showing, the maximal growth rate is found to be $\gamma_{max}/\Omega_{i0} = 13.1$, located at $\mathbf{k}\times\mathbf{B} = 0$, with $(k_x, k_y)\rho_{i0} = (-10.0, 10.0)$. The instability appears to be the ion-electron streaming instability, also known as the Buneman instability, as predicted by Yoon and Lui[131], which peaks at $\mathbf{k} \times \mathbf{B} = 0$.

It is believed that collisonless magnetic reconnection requires an excitation of anomalous resistivity at the current sheet center, or the neutral point of magnetic field. Since the

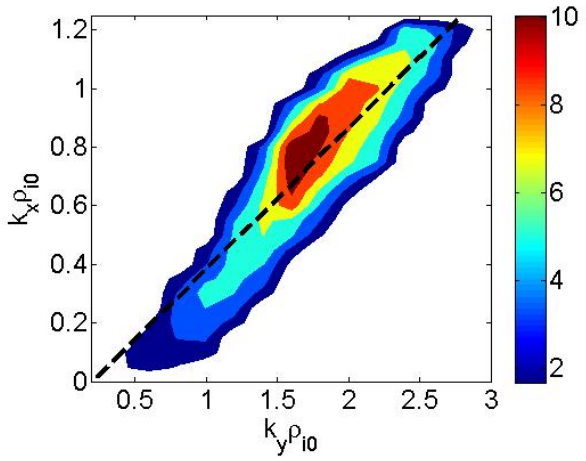

Figure 4.24: Contours of growth rate γ in the k_x-k_y space for $L/\rho_{i0} = 0.25$, $T_e/T_i = 0.1$, $B_G/B_{x0} = 0.1$, $n_{b0} = 0.0$, $m_i/m_e = 1836$, and $\omega_{pe}/\Omega_{ce} = 1.0$. The dark dashed line marks $\hat{\mathbf{z}} \cdot (\mathbf{k} \times \mathbf{B}) = 0$. Colorbar shows growth rates.

location where $\mathbf{k} \cdot \mathbf{B} = 0$ can only be on the edge of the current sheet or outside the sheet center, it was argued that the LHDI, whose maximum growth rate occurs at $\mathbf{k} \cdot \mathbf{B} = 0$, may not be the direct cause for the anomalous resistivity. In the presence of a finite guide field B_G, we have found the existence of a Buneman instability mode with $\mathbf{k} \cdot \mathbf{B} \neq 0$ at the center of the current sheet. In this mode, the wave perturbation in magnetic field is dominated by a compressional fluctuation δB_y in the direction of the electron drift velocity. It is speculated that this mode may contribute directly to the electron anomalous resistivity in magnetic reconnection.

4.5 Summary

In this chapter, the electromagnetic instabilities in a Harris current sheet are studied systematically by using the 3-D GeFi δf particle simulation model for cases with a finite guide field B_G, with sheet normal in the z direction and guide field in the y direction. The instabilities are investigated for various (k_x, k_y). Effects of the guide field B_G are studied. The GeFi particle simulation results are compared with the GeFi theory and the FK particle simulations. The main results are summarized below.

1. The real space and eigenmode structures of LHDI obtained from the GeFi simulation agree very well with those from the FK δf simulations. The dispersion relation obtained from the GeFi simulation agrees very well with those obtained from the analytic theory and the FK simulation.

2. The lower-hybrid drift instability which exists under a small guide filed, localized at the edges of current sheet ($1 < |z/L| < 2$). The LHDI is essentially a quasi-electrostatic mode with the magnitude of $\delta\phi$ two orders of magnitude larger than $\delta\mathbf{A}$. The growth rates are calculated in the k_x-k_y space. The simulation results show that under a certain k_y, the dominant unstable mode of LHDI satisfies $\mathbf{k} \cdot \mathbf{B} = 0$ when the wave number k_y is relatively small. As the wave number becomes larger, the dominant unstable mode can peak at $\mathbf{k}\cdot\mathbf{B} \neq 0$, although the most unstable mode in the entire k_x-k_y plane still satisfies $\mathbf{k}\cdot\mathbf{B} = 0$.

3. The drift kink and the drift sausage instabilities are found under a moderate $B_G/B_{x0} = 0.2$ at $k\rho_{i0} \sim 1$ region. The magnetic fluctuations of DKI are localized at the edge of the current sheet, which propagates obliquely to the current. The compressional field of DSI is located around the center of the current sheet. The growth rates of the DKI and DSI as the function of k_x-k_y, show that the DSI is peaked at $\mathbf{k} \cdot \mathbf{B} = 0$ and the most unstable DKI is away from that.

4. Under a larger guide field, the Buneman instability with the compressional magnetic field δB_y localized at the center of the current sheet is found. The electrostatic fluctuation $\delta\phi$ is located at the edges ($L < |z| < 3L$), while the electromagnetic fluctuation $\delta\mathbf{A}$ is located at the center of the current. The growth rates are calculated in the k_x-k_y space, and it is found that the most unstable mode peaks at $\mathbf{k} \times \mathbf{B} = 0$.

Chapter 5

Summary

In this thesis, the instabilities in the Harris current sheet are investigated by the 3-D GeFi δf particle simulation code. The instabilities are calculated for a broad range of finite guide fields. The stability properties of unstable modes are systematically screened the (k_x,k_y) space. The GeFi particle simulation results are compared with the GeFi eigenmode theory and the FK particle simulations.

LHDI can be excited at a small but finite guide field $B_G/B_{x0} = 0.1$ and $k\sqrt{\rho_i\rho_e} \sim 1$. The electromagnetic perturbations of LHDI are localized at the edge of current sheet. The propagation direction of LHDI is parallel to the drift current. The LHDI is a quasi-electrostatic instability. The linear stability calculations show that compared to the cases in the purely ES limit, the LHDI in the fully EM calculation has a smaller growth rate and can be more efficiently stabilized by an increasing B_G. LHDI is found to be scaled with the lower hybrid characteristic length $1/\sqrt{\rho_{i0}\rho_{e0}}$ and frequency ω_{LH} when m_i/m_e and L vary. Since the LHDI is located at the current sheet edge, the instability in the linear stage may not directly contribute to the anomalous resistivity.

DSI and DKI are found to coexist at $k\rho_i \sim 1$ and $B_G/B_{x0} = 0.2$. DSI possesses a compressional magnetic perturbation around the sheet center, thus it is a potential source of anomalous resistivity. The fluctuations of DKI are located at the sheet edge, similar to the LHDI, and thus the instability may not directly produce anomalous resistivity. The growth rate contours show that the DKI is present at $k_y\rho_{i0} < 4$, while the DSI is at $k_y\rho_{i0} > 4$. The most unstable DKI is away from $\mathbf{k}\cdot\mathbf{B} = 0$, while, the DSI is peaked at $\mathbf{k}\cdot\mathbf{B} = 0$.

An electromagnetic unstable mode is found to be present at a larger $B_G/B_{x0} = 0.6$ and $k\sqrt{\rho_i\rho_e} \sim 1$. The mode has a compressional magnetic perturbation at the center of current

sheet. Therefore, the unstable mode may have the contribution to anomalous resistivity. The calculation of growth rate in k_x-k_y shows that the most unstable mode is at $\mathbf{k} \times \mathbf{B} = 0$. It is consistent with the calculations of Buneman instability calculated with the two-fluid theory. Hence, the instability is recognized as the Buneman instability. Since the magnetic perturbation of this mode is dominated by a compressional fluctuation δB_y in the direction of the electron drift velocity, it is suggested that this mode may contribute directly to the elctron anomalous resistivity in magnetic reconnection.

Bibliography

[1] Dungey J W, Phys. Rev. Lett., **6**, 47 (1961).

[2] Birn J, Drake J F, Shay M A, et al., J Geophys Res, **106** A3 3715 (2001).

[3] Yamada M, Kulsrud R, Ji H T, Reviews of Modern Physics, **82** 603 (2010).

[4] Tsuneta S, Hara H, Shimizu T, et al., Publications of the Astronomical Society of Japan, **44** L63 (1992).

[5] Golub L, Bookbinder J, Deluca E, et al., Phys Plasmas, **6** 2205 (1999).

[6] Masuda S, Kosugi T, Hara H, et al., Nature, **371** 495 (1994).

[7] Qiu J, Wang HM, Cheng CZ, et al., Astrophys J, **604** 900 (2004).

[8] Russell C T, Elphic R C, Space Sci Rev, **22** 681 (1978).

[9] Lee L C, Fu Z F, Geophys Res Lett, **12** 105 (1985).

[10] Hasegawa H, Wang J, Dunlop M W, et al., Geophys Res Lett, **37** L16101 (2010).

[11] Baker D N, Pulkkinen T I, Angelopoulos V, et al., J Geophys Res, **101** A6 12975 (1996).

[12] Lui A T Y, J Geophys Res, **101** A6 13067 (1996).

[13] Yamada M, Ji H T, Hsu S, et al., Phys Plasmas, **4** 1936 (1997).

[14] Yamada M., J Geophys Res, **104** A7 14529 (1999).

[15] Brin J, Priest E R, Reconnection of Magnetic Fields: Magnetohydrodynamics and Collisionless Theory and Observations, Cambridge University Press, 144 (2007).

[16] Kusano K, Sakurai T, Solar flares, Reconnection of Magnetic Fields: Magnetohydrodynamics and Collisionless Theory and Observations, Cambridge University Press, 275 (2007).

[17] Trattner K J, Fuselier S A, Petrinec S M, Observations of magnetopause reconnection, Reconnection of Magnetic Fields: Magnetohydrodynamics and Collisionless Theory and Observations, Cambridge University Press, 180 (2007).

[18] Baumjohann W, Nakamura R, Observations of tail reconnection, Reconnection of Magnetic Fields: Magnetohydrodynamics and Collisionless Theory and Observations, Cambridge University Press, 209 (2007).

[19] Drake J F, Shay M A, Fundamentals of collisionless reconnection, Reconnection of Magnetic Fields: Magnetohydrodynamics and Collisionless Theory and Observations, Cambridge University Press, 87 (2007).

[20] Hesse M, Diffusion region physics, Reconnection of Magnetic Fields: Magnetohydrodynamics and Collisionless Theory and Observations, Cambridge University Press, 108 (2007).

[21] Pritchett P L, Onset of magnetic reconnection, Reconnection of Magnetic Fields: Magnetohydrodynamics and Collisionless Theory and Observations, Cambridge University Press, 121 (2007).

[22] Bhattacharjee A, Dorelli J C, Hall MHD reconnection, Reconnection of Magnetic Fields: Magnetohydrodynamics and Collisionless Theory and Observations, Cambridge University Press, 132 (2007).

[23] Buchner J, Daughton W S, Role of current-aligned instabilities, Reconnection of Magnetic Fields: Magnetohydrodynamics and Collisionless Theory and Observations, Cambridge University Press, 144 (2007).

[24] Yokoyama T, Shibata K, Astrophysical J, **436** L197 (1994).

[25] Zweibel E G, Yamada M, Annual Review of Astronomy and Astrophysics, **47** 291 (2009).

[26] Sweet P A, The neutral point theory of solar flares, Cambridge: Cambridge University Press, 123 (1958).

[27] Parker E N, Journal of Geophysical Research, **62**, 509-520 (1957).

[28] Petschek H E, Magnetic field annihilation, Symposium on the Physics of Solar Flares NASA, 425 (1964).

[29] Vasyliunas V M, Reviews of Geophysics, **13** 303 (1975).

[30] Biskamp D, Phys Fluids, **29** 1520 (1986).

[31] Uzdensky D A, Kulsrud R M, Phys Plasmas, **7** 4018 (2000).

[32] Mozer FS, Bale SD, Phan TD, et al, Phys. Rev. Lett., **91** 245002 (2003).

[33] Nagai T, Fujimoto M, Saito Y, et al, J Geophys Res-Space, **A103** 4419 (1998).

[34] Eastwood J P, Phan T D, Oieroset M, et al, J Geophys Res-Space, **115** A08215 (2010).

[35] Ren Y, Yamada M, Ji H, et al, Phys Rev Lett, **101** 085003 (2008).

[36] Ren Y, Yamada M, Ji H, et al, Phys Plasmas, **15** 082113 (2008).

[37] Kuznetsova MM, Hesse M, Winske D., J Geophys Res-Space, **A103** 199 (1998).

[38] Pritchett P L, J Geophys Res-Space, **A106** 25961 (2001).

[39] Pritchett P L, J Geophys Res-Space, **A106** 3783 (2001).

[40] Hesse M, Schindler K, Birn J, Phys Plasmas, **6** 1781 (1999).

[41] Daughton W, Scudder J, Karimabadi H. Phys Plasmas, **13** 072101 (2006).

[42] Eastwood J P, Phan T D, Mozer F S, et al, J Geophys Res-Space, **A112** 06235 (2007).

[43] Wang R S, Lu Q M, Du A M, et al, Phys Rev Lett, **104** 175003 (2010).

[44] Wang R S, Lu Q M, Huang C, et al, J Geophys Res-Space, **A115** 01209 (2010).

[45] Shay M A, Drake J F, Swisdak M, Phys Rev Lett, **99** 155002 (2007).

[46] Phan T D, Drake J F, Shay M A, Phys Rev Lett, **99** 255002 (2007).

[47] Bessho N, Bhattacharjee A, Phys Rev Lett, **95** 245001 (2005).

[48] Coppi B, Laval G, Pellat R, Phys Rev Lett, **16**, 1207 (1966).

[49] Laval G, Pellat R, Vuillemin M, Plasma Physics and Controlled Nuclear Fusion, **2** 259 (1966).

[50] Biskamp D, Schindler K, Plasma Phys, **13** 1013 (1971).

[51] Sonnerup B, J Geophys Res, **79**, 1546 (1974).

[52] Quest K B, Coroniti F, J Geophys Res, **86**, 3289 (1981).

[53] Drake J F, Lee Y C, Phys Fluids, **20** 1341 (1977).

[54] Wang X, Lin Y, Chen L, Lu X, and Kong W, Phys. Plasmas **5**, 122102 (2011).

[55] Daughton W, Karimabadi H, J Geophys Res-Space, **A110**, 03217 (2005).

[56] Davidson R C, Gladd N T, Wu C S, Huba J D, Phys. Fluids **20**, 301 (1977).

[57] Carte T A, Yamada M, Ji H, Kulsurd R M, Trintchouk F, Phys. Plasmas **9**, 3272 (2002).

[58] Sanuki H, Watanabe T, Watanabe M, Phys. Fluids **23**, 158 (1980).

[59] Ross D W and Mahajan S M, Phys. Rev. Lett. **40**, 324 (1978).

[60] Huba J D, Drake J F, Gladd N T, Phys. Fluids **23** 552 (1980).

[61] Yoon P H, Lui A T Y, Phys. Plasmas **15** 072101 (2008).

[62] Tummel K, Chen L, Wang Z, Lin Y, Wang X Y, Phys. Plasmas **21** 052104 (2014).

[63] Daughton W, Phys. Plasmas **6**, 1329 (1999).

[64] Daughton W, Phys. Plasmas **10**, 3103 (2003).

[65] Lapenta G, Brackbill J U, Daughton W, **10** 1577 (2003).

[66] Daughton W, Lapenta G, Ricci P, Phys. Rev. Lett. **93** 105004 (2004).

[67] P. Ricci, J. U. Brackbill, W.Daughton, and G. Lapenta, Phys. Plasmas. **12**, 055901 (2005).

[68] L. Yin, W. Daughton, H. Karimabadi, B.J. Albright, K.J. Bowers and J. Marguline, Phys. Rev. Lett, **101** 125001 (2008).

[69] W. Daughton, V. Roytershteyn, H. Karimabadi, L. Yin, B.J. Albright, B. Bergen and K.J. Bowers, Nature Physics, **7** 539 (2011).

[70] W. Daughton, J. Geophys. Res. **103** A12 29429 (1998).

[71] Ozaki M, Sato T, Horiuchi R, et al, Phys. Plasmas, **3** 2265 (1996).

[72] Pritchett P L, Coroniti F V, J Geomagn. Geoelectr., **99** 5953 (1996).

[73] Pritchett P L, Coroniti F V, Decyk V K, J Geophys Res-Space, **101** 27413 (1996).

[74] Lapenta G, Brackbill J U, J Geophys Res-Space, **102** 27099 (1997).

[75] Zhu Z, Winglee R M, J Geophys Res-Space, **101** 4885 (1996).

[76] Zhu Z, Winglee R M, Parks G K, Eos Trans AGU **73** 43 Fall Meet Suppl 461 (1992).

[77] Yoon P H, Lui A T Y, Wong H K, J Geophys Res-Space, **103** 11875 (1998).

[78] Shay M A and Drake J F, Geophys. Res. Lett. **25** 3759 (1998).

[79] Pritchett P L, J. Geophys. Res. **106** 3783 (2001).

[80] Mandt M E, Denton E R and Drake J F, Geophys. Res. Lett. **21** 73 (1994).

[81] Hesse M and Winske D, J. Geophys. Res. **103** 26479 (1998).

[82] Lin Y, Wang X, Chen L, Lu X, and Kong W, Plasma Phys. Control. Fusion **53** 054013 (2011).

[83] Lin Y, Wang X, Lin Z, and Chen L, Plasma Phys. Control. Fusion **47** 657 (2005).

[84] Wang X, Lin Y, Chen L, and Lin Z, Phys. Plasmas **15** 072103 (2008).

[85] Qi L, Wang X, and Lin Y, Phys. Plasmas **20**, 062107 (2013).

[86] Freiman E A and Chen L, Phys. Fluids **25**, 502 (1982).

[87] Hahm T S, Lee W W, Brizard A, Phys. Fluids **31** 1940 (1988).

[88] Brizard A, J. Plasma Phys. **41** 541 (1989).

[89] Brizard A, Phys. Fluids B **4** 1213 (1992).

[90] Lee W W, Phys. Fluids **26** 556 (1983).

[91] Birdsall C K and Langdon A B, Plasma Physics via Computer Simulation (Bristol: Institute of Physics) 1991.

[92] Harris E G, Nuovo Cimento, **23**, 115 (1962).

[93] Lee W W, J. Comp. Phys., **72**, 243 (1987).

[94] Zhang W S, Finite Difference Methods for Partial Differential Equations in Science Computation (Beijing: Higher Education Press) 2006.

[95] Press W H, Teukolsky S A, Vetterling W T, Flannery B P, Numerical recipes in Fortran 77: the Art of Scientific Computing - Second Edition (Cambridge: Cambridge University Press) 1992.

[96] Buneman O and Pardo W, Relativistic Plasmas The Coral Gables Conference University of Miami, Benjamin, New York, 205-219, 1968.

[97] Morse R L, Nielson C W, Phys. Fluids **14**, 830 (1971).

[98] Boris J P, Proc. Fourth Conf. Num. Sim. Plasmas, pp. 3-67, Naval Res. Lab., Washington D.C., 1970.

[99] Birdsall C K, Fuss D, Proc. Second Conf. Num. Sim. Plasmas, Los Alamos Sci. Labs., **LA-3990**, 18-20, 1968.

[100] Kleva, R. G., Drake, J. F., Waelbroeck, F. L., Phys. Plasmas, **2**, 23 (1995).

[101] Y. S. Wang, R. Kulsrud and H. T. Ji, Phys. Plasmas **15**, 122105 (2008).

[102] P. H. Yoon and A. T. Y. Lui, J. Geophys. Res. **109**, A02210 (2004).

[103] A. T. Y. Lui, P. H. Yoon and C. L. Chang, J. Geophys. Res. **98**, A1 153 (1993).

[104] I. Shinohara, T. Nagai, M. Fujimoto, T. Terasawa, T. Mukai, K. Tsuruda, and T. Yamamoto, J. Geophys. Res. **103**, A9 20365 (1996).

[105] N. Singh, I. Khazanov and B. E. Wells, Phys. Plasmas **22**, 052117 (2015).

[106] P. Petkaki, M. P. Freeman, T. Kirk, C. E. J. Watt and R. B. Horne, J. Geophys. Res. **111**, A01205(2006).

[107] I. Silin, J. Buchner and A. Vaivads, Phys. Plasmas **12**, 062902 (2005).

[108] P. H. Yoon and A. T. Y. Lui, Phys. Plasmas **15** 072101 (2008).

[109] Zeiler, A., D. Biskamp, J. F. Drake, B. N. Rogers, M. A. Shay, and M. Scholer, J. Geophys. Res., **107** A9, 1230 (2002).

[110] M. Scholer, I. Sidorenko, C. H. Jaroschek, R. A. Treumann and A. Zeiler, Phys. Plasmas **10**, 3521 (2003).

[111] V. Roytershteyn, W. Daughton, H. Karimabadi, and F. S. Mozer, Phys. Rev. Lett. **108**, 185001 (2012).

[112] M. Tanaka, and T. Sato, J. Geophys. Res., **86** A7, 5541 (1981).

[113] M. Hoshino, J. Geophys. Res., 96(A7), 11555 (1991).

[114] G. Lapenta and J. U. Brackbill, Phys. Plasmas **9**, 1544 (2002).

[115] P. Ricci, J. U. Brackbill, W. Daughton and G. Lapenta, Phys. Plasmas **11**, 4489 (2004).

[116] B. N. Rogers, J. F. Drake, M. A. Shay, Geophys. Res. Lett. **27** 3157 (2000).

[117] Y. Chen, S. Parker, Phys. Plasmas **8** 2095 (2001).

[118] J. M. TenBarge, W. Daughton, H. Karimabadi, G. G. Howes and W. Dorland, Phys. Plasmas **21**, 020708(2014).

[119] D. Liu, J. Bao, T. Han, J. Wang and Z. Lin, Phys. Plasmas **23**, 022502(2016).

[120] W. Wan, Y. Chen and S. E. Parker, Phys. Plasmas **12** 012311(2005).

[121] J. Bao, Z. Lin, A Kuley and Z X Lu, Plasma Physics and Controlled Fusion, **56** 095020 (2014).

[122] Z Lin, L Chen, Phys. Plasmas **8** 1447 (2001).

[123] Y. Chen, S. E. Parker, Journal of Computational Physics **189** 463 (2003).

[124] A. J. Brizard and T. S. Hahm, Rev. Mod. Phys. **79** 421 (2007).

[125] G. G. Howes, S. C. Cowley, W. Dorland, G. W. Hammett, E. Quataert and A. A. Schekochihin, Astrophys. J. **651**, 590 (2006).

[126] Z Lin, W M Tang, W W Lee, Phys. Plasmas **2** 2975 (1995).

[127] P. Porazik and J. J. Johnson, J. Geophys. Res. **A118** 2169 (2013).

[128] K. J. Bowers, B. J. Albright, L. Yin, B. Bergen and T. J. T Kwan, Phys. Plasmas **15** 055703 (2008).

[129] L. Qi, X. Y. Wang and Y. Lin, Phys. Plasmas **20** 062107 (2014).

[130] P. H. Yoon, Y. Lin, X. Y. Wang, and A. T. Y. Lui, Phys. Plasmas **15** 112103 (2008).

[131] Yoon P H, Lui A T Y, Phys. Plasmas., **15** 112105 (2008).

[132] Zhou M, Deng X H, Li S Y, et. al., J. Geophysics Res. **114** A02216 (2009).

[133] Z. Wang, Y. Lin, X. Wang, K. Tummel, L. Chen, Phys. Plasmas, to be published 2016.

[134] Yamada M, Ji H, Kulsrud R M, American Geophysics Union, Spring Meeting 2002.

[135] Tummel K, APS Division of Plasma Physics Annual Meeting, New Orleans, 2014.